Study of impact ejecta from small bodies in the solar system

Yamamoto, Satoru

(Degree)
博士（理学）
(Date of Degree)
1999-03-31
(Date of Publication)
2015-06-11
(Resource Type)
doctoral thesis
(Report Number)
甲1907
(JaLCDOI)
https://doi.org/10.11501/3156308
(URL)
https://hdl.handle.net/20.500.14094/D1001907

博士論文

Study of impact ejecta from small bodies in the Solar System

平成１１年１月

神戸大学大学院自然科学研究科

山本　聡
Satoru Yamamoto

博士論文

Study of impact ejecta from small bodies in the Solar System

(太陽系小天体における衝突現象および衝突放出物の研究)

Satoru Yamamoto

The graduate School of Science and Technology,
Kobe University, Nada, Kobe, 657-8501, Japan

Contents

1 General Introduction

Continuous bombardments of meteoroids onto airless bodies, such as the Moon or planetary satellites, result in enhancement of dust in the vicinity of the planetary bodies and can result in formation of dust rings. The mutual collisions between small bodies, such as asteroids or Edgeworth-Kuiper Belt objects (EKOs), provide a significant amount of dust grains in the interplanetary space. These impact ejecta are one of major sources of dust grains of the zodiacal cloud. This thesis is dedicated to the understanding of dynamical properties of the impact ejecta produced by the mutual collisions of planetary bodies and by the bombardment of meteoroids. This thesis consists of two parts. The first part (Chapters 2 and 3) is devoted to impact ejecta escaping from the Moon (the so-called 'lunar ejecta'). The second part (Chapters 4, 5, 6, and 7) is devoted to the dust grains from Edgeworth-Kuiper Belt (EKB).

Hypervelocity impacts of interplanetary meteoroids on the surface of the Moon provide lunar ejecta with velocities higher than the lunar escape velocity (~ 2.4 km s^{-1}). Ten meteorites identified as lunar rock have been discovered in the Antarctic on the Earth (e.g. Warren, 1994). These large meteorites, with masses larger than several grams, were produced by sporadic impact of much larger meteoroids. It is natural to assume that lighter lunar micro-sized particles are more frequently ejected from the lunar surface to the space.

In previous studies of lunar ejecta, the surface of the Moon was treated as hard rock and the velocity distribution of ejecta from hard surface was incorporated (e.g. Alexander et al. 1984; Yamamoto & Mukai 1996). However, the real surface of the Moon is covered by regolith layer. Large meteoroids excavate deeper, hard rock regions of the Moon. On the contrary, the impacts of small particles, which provide a continuous flux of ejecta, produce the craters in the regolith layers. Consequently, in order to examine the continuous flux of ejecta produced by impacts of small meteoroids rather than sporadic collisions of large meteoroids, the data of velocity distribution of ejecta from regolith target is highly needed. In previous works, the measurements of the velocity distribution of powdery ejecta were derived only for low velocity ejecta ($<$ tens of m s^{-1})(e.g. Housen et al. 1983; Hartmann 1985). In order to estimate the continuous flux of the lunar ejecta, it is necessary to know the amount of ejecta with velocity higher than the lunar escape velocity (~ 2.4 km s^{-1}).

In Chapter 2, I performed new impact experiments onto the regolith-like layers to obtain the velocity distribution of ejecta with velocity higher than several hundred m s^{-1}. Spherical nylon projectile of 7.0 mm in diameter was accelerated to about 4 km s^{-1} by using a two-stage light-gas gun. The ejecta were detected by thin Al foil targets of different thickness, and the resulting holes on the foil were counted to derive the velocity distribution using an empirical formula of threshold penetration (McDonnell & Sullivan, 1992). From the resulting velocity distribution, the total mass of ejecta with velocity higher than several hundreds of m s^{-1} were derived. The results were compared to a scaling formula (Housen et al., 1983) deduced from the low velocity data of the ejecta from sand targets. It is found that, although our results of the volume of ejecta with higher velocity lie below the extrapolation of the lower velocity data, the differences were within about one order of magnitude.

In Chapter 3, I estimated a production rate of lunar ejecta escaping from the Moon, by using the results obtained in Chapter 2. I found that the mass production of lunar ejecta from the particulate surface is more effective compared with that from hard surface.

The lunar ejecta evolve their orbits under the effects of the gravitational forces by the Moon, Earth and the Sun, mutual collisions, solar radiation pressure, Poynting-Robertson effects, and electromagnetic forces in the Earth-Moon system. These dynamical processes depend strongly on the grain size as well as its shape and material component. In order to study the contribution of lunar ejecta to zodiacal cloud and interplanetary dust particles (IDPs) collected in the stratosphere of the Earth, it is important to investigate the production process of lunar ejecta as a function of size. Therefore, in Chapter 3, I also estimated the cumulative flux of lunar ejecta as a function of size. The size distribution of the lunar ejecta is assumed to be related to that of the lunar soil sample (McKay et al. 1991) from the Moon. In the previous studies based on the hard surface model (e.g. Alexander et al. 1984; Yamamoto & Mukai 1996), the maximum sizes of lunar ejecta were estimated to be a few μm. On the other hand, for the case of regolith layers, the lunar ejecta with radii larger than tens of μm could escape from the Moon.

The second part of this thesis (Chapters 4, 5, 6, and 7) is devoted to the dust grains from EKOs. Recently, it has been suggested that significant dust production occurs in EKB (e.g. Backman et al. 1995; Stern 1996). Jewitt et al. (1996) estimated that about 7.0×10^4 objects with diameters larger than 100km exist in EKB. Duncan et al. (1995) estimated that, within 50 AU, the total number of comets in EKB is roughly 5×10^9. It has been proposed that the collisions between these objects provide a significant amount of dust grains in EKB. Stern (1996) estimated the production rate of collisional debris, and predicted a time-averaged mass supply rate of $3 \times 10^{16} \sim 10^{19}$g yr^{-1}, for collisional debris ranging from multi-kilometer blocks to fine dust.

In Chapter 4, I proposed that the impacts by such interstellar dust on EKOs produce a considerable amount of dust grains. EKOs are continuously bombarded by interstellar dust grains with high relative velocities ($\sim$ 26 km s^{-1}). Although the amount of target material excavated by the individual impacts of interstellar dust is smaller than the amount produced by catastrophic collisions between large EKOs, impacts by interstellar dust grains occur more frequently and continuously. Moreover, all EKOs are bombarded by interstellar dust simultaneously, whereas the mutual collisions of EKOs occur locally. As a consequence, the continuous impacts by interstellar dust should provide a considerable amount of dust grains all over the EKB. By using the flux of interstellar dust measured by the Ulysses space craft, I estimated the production rate of dust grains by the impacts of interstellar dust grains on EKOs. I concluded that dust production due to the impacts by interstellar dust on EKOs is a significant source of interplanetary dust grains with radii smaller than about 10 μm, at least for those far from the Sun.

In spite of the significant dust production in EKB, the existence of these dust grains coming from EKOs has not yet been directly confirmed by observations of zodiacal light/emission or *in situ* measurements. Just releasing from EKOs, the orbital elements of dust grains are immediately changed due to their ejection velocity and solar radiation pressure on them. The dust grains taking bound orbits form the dust cloud in EKB, and then reduce gradually their perihelion distances and eccentricities under the Poynting-Robertson effect. Therefore, a fraction of the dust grains produced in EKB may contribute to the population of the interplanetary dust inside the orbit of Jupiter.

In Chapter 5, the dynamical evolution and the detectabilities of EKB dust grains by *in situ* measurement were investigated. Taking into account the gravitational force of the Sun, the solar radiation pressure, the Poynting-Robertson effect, as well as the ejection velocity of dust grain, I investigated the orbital evolution of dust grains, consisting of water-ice, released from EKOs. It is found that all dust grains with radii greater than 1μm ejected from EKOs can stay in the Solar System against the solar radiation pressure, when the parent EKOs have eccentricities less than 0.3. At the Jupiter crossing orbit, the major part of survival dust grains have already circular orbits because of the Poynting-Robertson effect. Consequently, I concluded that when the grains with sizes larger than 1μm on the nearly circular orbits would be detected beyond Jupiter, their origin is the EKOs.

In Chapter 6, I investigated the detectability of thermal radiation from the dust cloud in EKB. The temperatures of EKB dust grains were calculated based on the model of heterogeneous icy material consisting of small refractory inclusions embedded in icy matrix such as cometary dust. Applying the results of temperature for EKB dust grains, we examined the thermal emission from dust cloud existing between 30 AU and 50 AU. Since the predicted thermal emission from EKB dust cloud is fainter than that of IRAS data, it seems to be difficult to find a sign of thermal emission from EKB dust cloud in the past observations from the Earth. On the other hand, I found that the maximum case of thermal emission from EKB dust cloud becomes to be comparable to that of foreground zodiacal emission in far-infrared and submillimeter wavelength domains.

In addition to EKOs between the solar distances of 30 AU and 50 AU, it is suggested that the aggregates of planetesimals, which are too faint to detect from the Earth, must exist beyond 50 AU (Yamamoto & Kozasa 1988). In Chapter 7, the contribution of thermal emission from the objects in EKB beyond 50

AU were considered. Furthermore, the mass distributions of dust grains beyond 50 AU were investigated based on numerical model which takes into account grain-grain collisions and the Poynting-Robertson effect (Ishimoto & Mann 1998). The resulting brightness of the thermal emission from EKB dust disk beyond 50 AU is fainter than the foreground zodiacal emission in infrared wavelength domain. Therefore, it seems to be difficult to find a sign of thermal emission from EKB dust disk beyond 50 AU in the past observation.

Acknowledgement Many people have contributed to this thesis. I am extremely grateful to Prof. T.Mukai and assistant Prof. A.M.Nakamura of Kobe University, Japan, for providing constructive comments, helpful suggestions, and continuous encouragement. Gratitude is also expressed to Prof. J.A.M.McDonnell and the colleagues of Kent university, U.K., for providing the opportunity to study impact experiments in their laboratory. I am also grateful to Prof. T.Yamamoto of Hokkaido University, Japan, for valuable discussion and suggestions. In addition, appreciation is expressed to Dr.H. Ishimoto and Dr. R.Nakamura of Kobe University, who gave me valuable suggestions and shared passions in scientific studies with me. Finally, I wish to express to all colleagues in the Solar System Physics Group of Graduate School of Sci. & Tech. in Kobe University.

References

Alexander, M., Anz, P., Lyons, D., et al., 1984, Adv.Space Res., 4, 23.

Backman, D.E., Dasgupta, A., Stencel, R.E., 1995, ApJ, 450, L35.

Duncan, M.J., Levison, H.F., Budd, S.M., 1995, AJ, 110, 3073.

Hartmann, W.K., 1985, Icarus, 63, 69.

Housen, K.R., Schmidt, R.M., Holsapple, K.A., 1983, J. Geophys. Res., 88, 2485.

Ishimoto, H., Mann, I., 1998, Planet. Space Sci., in press.

Jewitt, D., Luu, J., Chen, J., 1996, Astron.J, 112, 1225.

McDonnell, J.A.M., Sullivan, K., 1992, Hypervelocity Impacts in Space (edited by McDonnell, J.A.M.), pp. 39, Unit for Space Sciences, University of Kent (Canterbury).

McKay, D.S., Heiken, G., Basu, A., et al., 1991, Lunar sourcebook, a user's guide to the Moon (edited by Heiken, G., Vaniman, D., French, B.M.), pp. 285, Cambridge Univ. press.

Stern, S.A., 1996, A&A, 310, 999.

Warren, P.H., 1994, Icarus, 111, 338.

Yamamoto,T., Kozasa, T., 1988, Icarus, 75, 540.

Yamamoto, S., Mukai, T., 1996, Physics, Chemistry, and Dynamics of Interplanetary Dust (edited by Gustafson, B.A.S., Hanner, M.S.), pp. 47, PASP Conference Series, Provo, Utah.

2 Velocity Measurement of Impact Ejecta from Regolith Target

S.Yamamoto & A.M.Nakamura
Icarus, **128**, 160-170 (1997)

Abstract

We performed new impact experiments onto regolith-like layers of glass spheres to investigate the spatial and velocity distributions of ejecta with velocities higher than several hundred m s^{-1}. Spherical nylon projectiles of 7.0 mm in diameter were accelerated to about 4 km s^{-1} by using a two-stage light-gas gun. The ejecta were detected by thin Al foil targets of different thickness, and the resulting holes on the foil were counted to derive the velocity distribution using an empirical formula of threshold penetration (McDonnell & Sullivan, 1992). The spatial distribution of the ejecta was also derived from the analysis of the position of the penetration holes. The high velocity ejecta concentrated toward downrange azimuth of impacting projectile, because of the oblique impacts of the projectiles into the targets. In order to estimate the total volume of ejecta with velocity higher than a given velocity, the measured spatial distributions were extrapolated to regions where no Al targets were exposed. The results were compared to a scaling formula (Housen et al., 1983) which is based on low velocity data of the ejecta from sand targets. Though our results of the volume of ejecta with higher velocity lie below the extrapolation of the lower velocity data, the differences were within about one order of magnitude.

2.1 Introduction

Impacts of meteoroids on the surface of airless bodies produce dust particles, redistribute material over the surface, and erode the target bodies. Hypervelocity impacts of interplanetary meteoroids on the surface of the Moon provide lunar ejecta with velocities higher than the lunar escape velocity ($\sim$ 2.4 km s^{-1}). Ten meteorites, which have been identified as lunar rock, have been discovered in the Antarctic on the Earth (e.g. Warren, 1994). These large meteorites with masses larger than several grams were produced by sporadic impact of much larger meteoroids (Melosh 1984, 1985). It is natural to assume that lighter lunar micro-sized particles are more frequently ejected than the larger meteorites. Alexander et al. (1984) have formulated a model of cumulative flux of micron and submicron ejecta from the Moon, empirically based on an analysis of impact experiments of rocky targets. Martian dust rings are composed of particles escaping from Phobos and Deimos by hypervelocity impacts of interplanetary meteoroids. The number density of these dust rings has been estimated based on impact experimental data onto rocky materials (e.g., Juhász et al., 1993; Ishimoto & Mukai, 1994; Ishimoto, 1996). However, the surfaces of the Moon and martian satellites as well as asteroids are covered with regolith layers. Large meteoroids excavate deeper, hard rock regions of such bodies. On the contrary, impacts of small particles, which provide a continuous flux of ejecta, produce craters in the regolith layers. Consequently, in order to examine the continuous flux of ejecta produced by impacts of small meteoroids rather than sporadic collisions of large meteoroids, data of velocity distribution of ejecta from regolith targets is highly needed.

Juhász et al. (1993) and Ishimoto (1996) also reported the spatial density of martian dust rings for models of the regolith surfaces of Martian satellites. However, the velocity distribution they used was based on the experimental data onto rocky materials (See Greenberg et al., 1978). Greenberg et al. (1978) hypothesized the velocity distribution of powdery ejecta could be represented by shifting the distribution of basalt, because of lack of the experimental data onto regolith layers.

We now briefly review previous works on regolith-like targets. Braslau (1970) measured contours of the expanding ejecta envelope during the first microseconds of the crater-forming process on photographs. He found no ejecta with speed higher than the projectile speed, and he found that the velocity of the ejecta was the highest immediately after impact. Hartmann (1985) investigated the leading edge of ejecta on films, and the velocity distribution of ejecta of a lower range of ejection velocities ($<$ 4 m s^{-1}) from the spatial distribution of the deposited ejecta. Yanagisawa & Itoi (1994) measured the velocities of ejecta from brittle targets and sands on flash X-ray radiograph. Their measurements were also for a lower range of ejection velocities ($<$ 110 m s^{-1}). Housen et al. (1983) have formulated the velocity distribution of ejecta from sand targets based on a dimensional analysis. Their result was expressed as $V_t(> v) \propto v^{\alpha}$, with $\alpha = -1.22 \pm 0.02$ being obtained for lower velocity ($\sim$ m s^{-1}) ejecta, where v is ejecta velocity and $V_t(> v)$ denotes ejecta volume with velocity greater than v.

The amount of escaping ejecta depends both on the velocity distribution of excavated material and the gravity of target bodies. From the velocity distribution of powdery ejecta derived in the previous works, we can estimate the flux of ejecta escaping from the gravitational field of target bodies of diameter smaller than tens of km. In order to treat larger target bodies of diameter larger than hundreds of km, however, it is necessary to know the amount of ejecta with velocity higher than hundreds of m s^{-1} (e.g. for the Moon, $\sim$ 2.4 km s^{-1}, and for Vesta, $\sim$350 m s^{-1} (Binzel & Xu, 1993)). It is important to examine whether the formula by Housen et al. (1983) can be extrapolated to the ejecta with a higher velocity.

We performed new impact experiments onto regolith-like layers to obtain the velocity distribution of ejecta with velocity higher than several hundred m s^{-1}. We detected the ejecta by exposing secondary targets in a similar way to those in Asada (1985) and Nakamura et al. (1994). Secondary targets of Al foil were set around powdery targets. A detail of experimental procedure will be described in Sect. 2.2. The analytical procedure to obtain the flux of the ejecta penetrated the Al foil targets is described in Sect. 2.3. The velocity distribution of the ejecta is shown in Sect. 2.4. The spatial distribution of the ejecta was derived in Sect. 2.5 from the analysis of positions of the holes on the Al foil targets. In order to estimate the total volume of the ejecta which can penetrate the Al foil of each thickness, the data were interpolated and extrapolated to the regions where no secondary target was exposed. Total volume of ejecta with velocity higher than a given velocity was derived using an empirical relation of threshold penetration (McDonnell & Sullivan, 1992). According to cratering scaling laws, the results were compared with the data of powdery ejecta with lower velocity and the values extrapolated from the results of the low velocity ejecta (Housen et al., 1983; Hartmann, 1985). The results and discussion are summarized in Sect. 2.6.

2.2 Experimental procedure

Spherical nylon projectiles of 7.0mm in diameter and mass 0.213g were accelerated to about 4 km s^{-1} by using a two-stage light-gas gun at the Institute of Space and Astronautical Science (ISAS). Targets were soda-lime glass powders with density of 2.5 g cm^{-3}. The median diameters of the glass spheres were 50μm and 80μm. The bulk density and porosity of the glass powders were, respectively, 1.4 g cm^{-3} and 44%. The glass spheres were put in the experimental chamber with an ambient pressure less than 1.0 Torr. Because the gun can accelerate projectiles horizontally and the angle of repose of powders is around 30° to the target surface (Statham 1974; Mann & Kanagy II, 1990), we performed the experiments of 30° impact angle to the surface of targets. The experimental conditions are summarized in Table 1.

Shot No.	Impact velocity (km s^{-1})	Diameter of target glass sphere	Thickness of Al foil	Ambient pressure (Torr)	Minimum detectable velocity (km s^{-1})
Shot 1	3.92	80μm	40μm, 50μm	0.9	0.60 , 0.83
Shot 2	4.08	80μm	25μm, 75μm	0.9	0.31 , 1.47
Shot 3	3.70	50μm	40μm, 50μm	0.8	1.22 , 1.68
Shot 4	4.00	50μm	15μm, 25μm	0.8	0.30 , 0.62

Table 1: Experimental conditions.

Five supporting panels with Al foil were set as a secondary target at a radial distance of 14cm from the impact site of the target. Because the Al foil gets shredded without a support, the panels of acrylic resin were used to support the thin pieces of Al foil. There are 48 apertures, each 10mm in diameter, at regular intervals on each panel of acrylic resin (Fig. 1). We placed two pieces of Al foil with different thicknesses on each panel bilateral symmetrically. Figure 1 shows the experimental configuration. The target surface

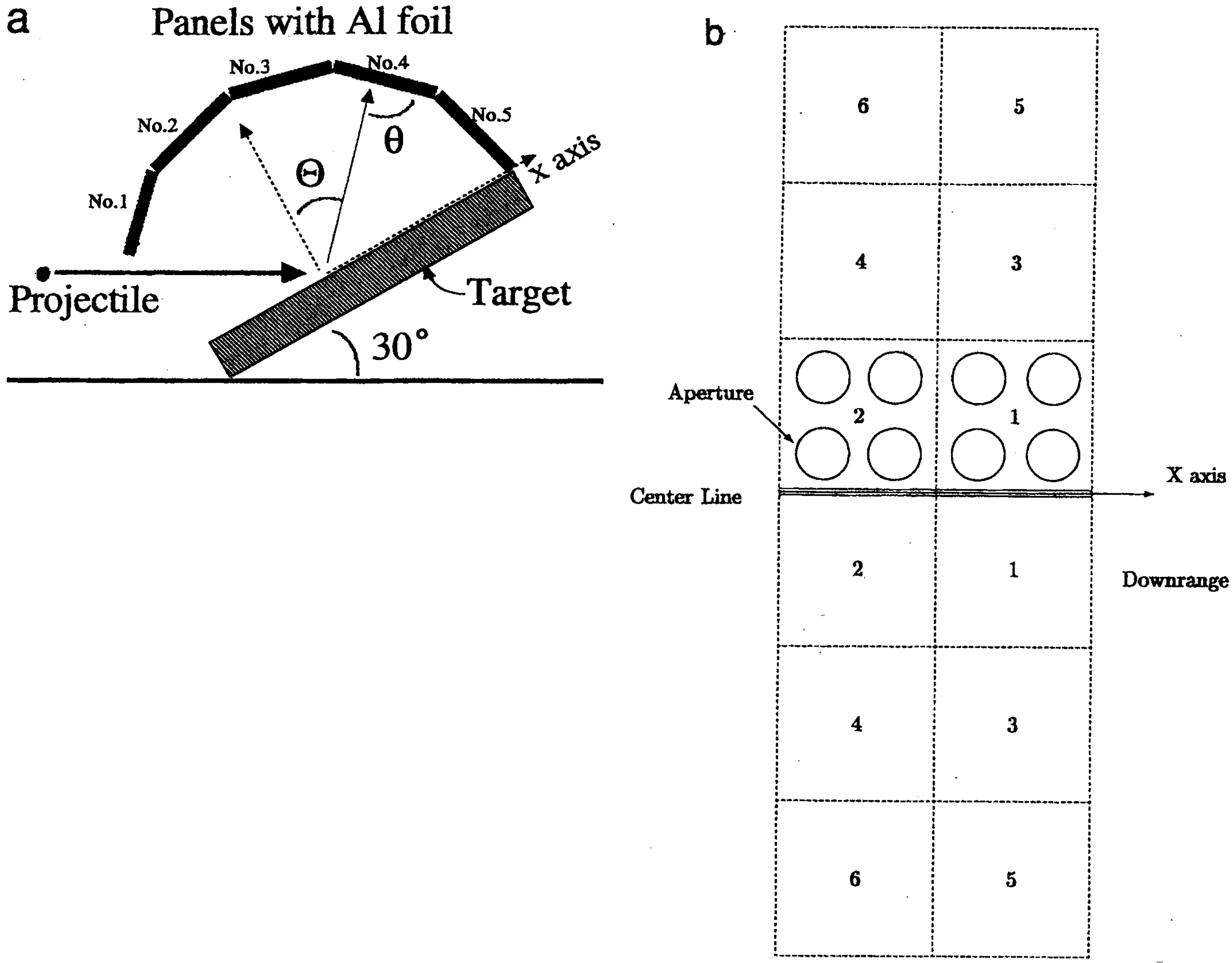

Figure 1: (a) Experimental configuration and coordinate system. Θ and θ are zenith angle in spherical coordinates and incident angle of ejecta to Al foil, respectively. (b) Configuration of apertures on each panel of acrylic resin.

component of the flight direction of the projectile defines the x axis. We define Θ and Φ as zenith angle and azimuth angle in spherical coordinates, respectively. The normal direction of the target surface corresponds to $\Theta = 0°$, and x axis corresponds to $\Phi = 0°$ and $\Theta = 90°$. Table 2 shows the detectable coverage of each panel.

In shot 1 and shot 2, we placed a piezo-electric sensor above the Al foil on No.4 and No.5 panels, respectively. The maximum velocity of particles was directly obtained from the time interval between the instances of projectile's impact into the powdery target and the detection by the piezo-electric sensor.

The ejecta were detected by the Al foil targets of different thicknesses and the resulting holes on them were studied. Ejecta with sufficient velocity penetrated Al foil, and left holes. We approximated that all glass spheres suffer no fragmentation as will be discussed in Sect. 2.3. Microscopic photographs of the Al foil were taken in order to measure the number density and the size distribution of holes penetrated by the ejecta. In our analysis, an empirical relation of threshold penetration was adopted to determine the limiting velocity of the penetrating particles (McDonnell & Sullivan, 1992),

$$T = 0.970 D_p^{0.056} \left(\frac{\delta}{\rho_t}\right)^{0.476} \left(\frac{\sigma_{Al}}{\sigma_t}\right)^{0.134} v^{0.701} \tag{1}$$

where $T = f/D_p$, v is impact velocity [km s^{-1}], f and D_p are, respectively, thickness of foil [μm] and size of incident particle [μm], σ_{Al} and σ_t denote, respectively, tensile strength of aluminum and the sheet material, δ is particle's density, and ρ_t is foil density. In oblique incidence with incident angle of θ, we replaced v by $v \sin\theta$ according to Pailer & Grün (1980). The minimum detectable velocities by each Al foil are shown in Table 1. Nakamura et al. (1994) estimated the error in velocity estimation by using Eq. (1) was within a factor of 2.5.

	Center of each panel (Θ,Φ) (deg)	Coverage Φ(deg)	Coverage Θ(deg)
Panel 1	(45,180)	136 to 224	36 to 58
Panel 2	(15,180)	111 to 249	6 to 41
Panel 3	(15,0)	-69 to 69	6 to 41
Panel 4	(45,0)	-44 to 44	36 to 58
Panel 5	(75,0)	-35 to 35	67 to 82

Table 2: Location and detectable coverage of apertures on panels.

2.3 Size distribution of holes

After experiments, holes with various sizes were left on each Al foil target. Figure 2 shows an example of a perforation on the Al foil after experiments. We compared the size distribution of the glass spheres with that of the holes penetrated on the Al foil (Fig. 3). Since the shapes of the holes were nearly circular as described in the following, we adopted the diameter of an equivalent area circle as the penetration hole size.

The distribution of the holes is shifted to larger size from the original size distribution of the glass spheres. When the projectile size is comparable to the thickness of target, the penetration hole size becomes larger than that of the projectile, in general. The hole diameter is approximately a linear function of velocity of the incident particle (see Gehring, 1970; Baker & Persechino, 1993).

Now we estimate the range of the penetration hole size, D_{min} and D_{max}, by using an empirical relation between impactor size, target thickness, impacting velocity and the penetration hole size. According to the estimated hole size, we count only holes with sizes between D_{min} and D_{max}, and determine the number density of penetration holes. It is expected that large holes are left on the Al foil due to overlapping of plural ejecta or fragments of ricocheting projectile. Therefore, we first discuss the overlapping and the ricochet, and then estimate the range of the penetration hole size in the following.

The overlapping probabilities of ejecta, $P(c,k)$, where c and k are, respectively, total number of ejecta impacting on an aperture and number of overlapping particles, were calculated for particles with diameters of $50\mu m$ and $80\mu m$. Since in our experiments the maximum value of c was about 500, the maximum $P(c,k)$ were calculated for $c = 500$ (Table 3). The value of $k = 0$ corresponds to the case in that no ejecta overlap. From Table 3 the maximum number of overlapping holes was estimated to be roughly about 10% of the total number of ejecta.

Furthermore, we investigate the shape of penetration hole on the Al foil and compare the experimental results with the overlapping probability described above in order to confirm the estimation in Table 3. The circularity of holes on the Al foil is plotted in Fig. 4. The measure of circularity, ϕ, is defined here to be the ratio D_{major}/D_{minor} where D_{major} and D_{minor} are, respectively, the major diameter and the minor diameter of a penetration hole. The value of $\phi = 1$ corresponds to a round hole. The distortion of penetration holes

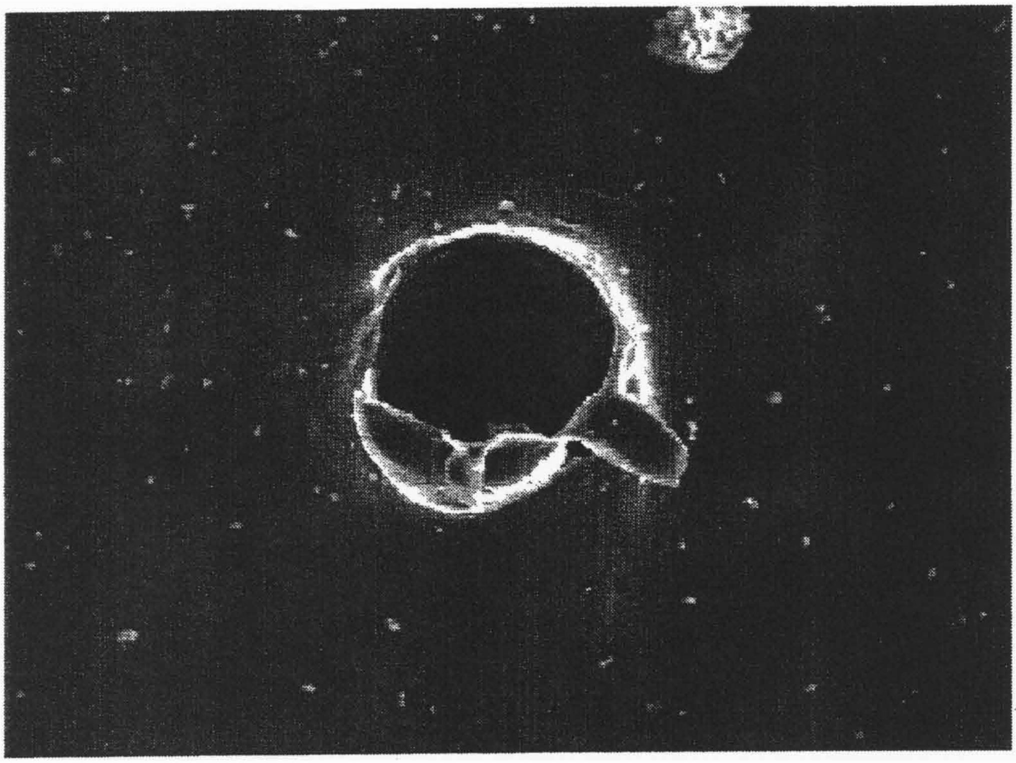

Figure 2: SEM image of $15\mu m$-thick Al foil after shot 4.

was due to an effect of the oblique incidence, the overlapping and disruption of the Al foil. In our analysis, the holes of detectable disruption were ignored and were not counted. The effect of oblique impact on the hole shape was obtained as (Barker & Persechino, 1993),

$$\phi = 1 + (1/\sin\theta - 1)e^{-\lambda v} \tag{2}$$

where θ is an impact angle from the surface of the Al foil and λ is given by the following function

$$\lambda = 0.84(1 - \theta/90^{o})(T - 0.035) \qquad \theta \geq 35^{o}$$

From Eq. (2) the maximum value of circularity due to the oblique incidence is calculated to be 1.3 in our experiment. Since the overlapping caused by two particles (k=1) is dominant (see Table 3) and partial overlapping is more probable than complete overlapping, the most frequent value of circularity due to the overlapping is within 2.0. For the overlapping caused by two particles, the overlapping probability of the circularities between ϕ to $\phi + d\phi$, denoted $p(\phi)d\phi$, is given by

$$p(\phi)d\phi = \frac{\phi - 1}{r_p} \times P(c, 1) \tag{3}$$

where r_p is the particle's radius. Since the probability of the overlapping increases in proportion to ϕ, the overlapping with circularities near 2.0 is more probable than complete overlapping. Thus, we assume that all the circularities between 1.4 and 2.0 are caused by the overlapping. From Fig. 4, the number fractions of the overlapping particles with circularities between 1.4 and 2.0, namely the overlapping probabilities, are from 0.08 to 0.14. These values agree with the result shown in Table 3. Finally, we estimated the overlapping probability was up to around 10%.

Gault & Wedekind (1978) reported that ricochet occurs for low-angle impacts. In this case, projectile shattered into many small fragments and they could tear some part of Al foil. In our experiment the incident

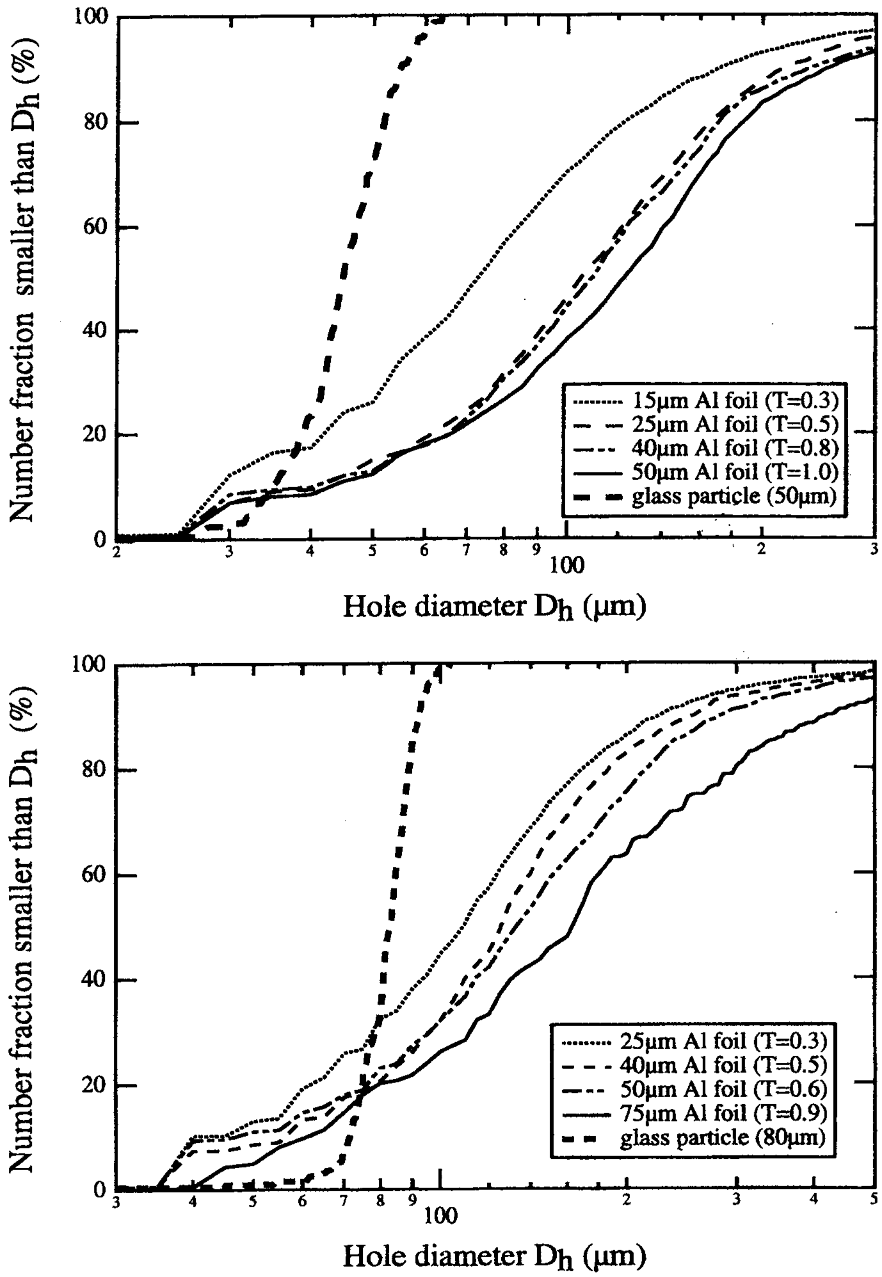

Figure 3: A comparison between size distributions of the prepared glass spheres and the holes perforated on the Al foil.

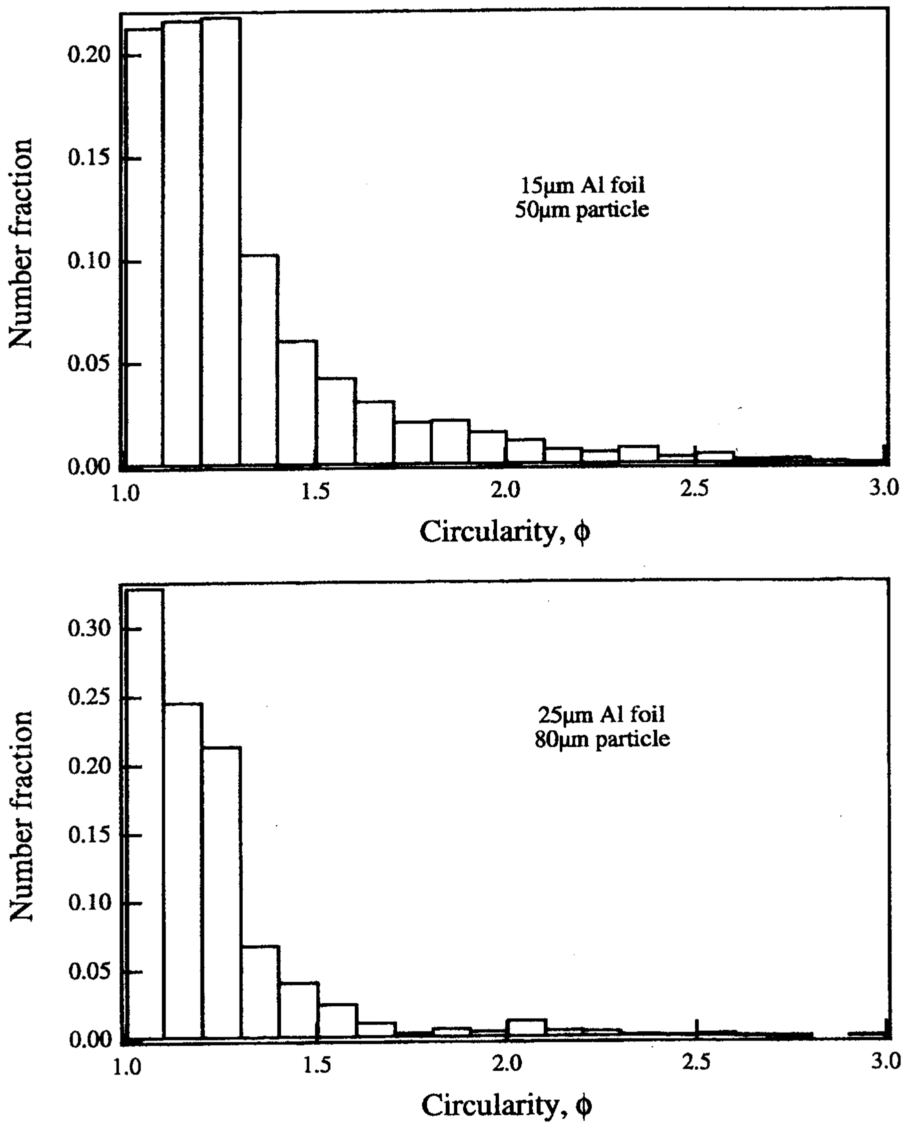

Figure 4: Circularity distribution of holes.

angle was 30° to the surface. According to Gault & Wedekind (1987) the critical value of incident angle for sand targets is about 15° and full development of the ricochet occurs at angles less than 10°. Therefore, the ricochet is expected to be not major source of the distorted holes in our experiments.

Some parts of the Al foil were disrupted since too many ejecta hit in one spot. In this case, the hole becomes irregular and the circularity of the hole can be larger than 2.0. The major sources of the holes with circularities larger than 2.0 came from the overlapping caused by more than three ejecta ($k \geq 2$) and the disruption of foil targets.

We expected penetration hole size as follows. The relation between the penetration hole size and the particle size was experimentally determined (e.g., Hörz et al., 1993; Barker & Persechino, 1993). According to Baker & Persechino (1993), the hole size can be fitted by an equation of the form

$$D_h/D_p = \alpha_n + \sigma_n v \tag{4}$$

where D_h and D_p are, respectively, diameters of the hole and the particle, and v is the impact velocity of the particle. The values of the slope α_n and the intercept σ_n are given by the following function of the target thickness:

$$\begin{aligned}
\sigma_n &= (0.26 + 0.15T)(1 - e^{-3.2(T-0.035)}) \\
\alpha_n &= 1 + 0.085(1 - e^{-18T}) && \text{for } T \leq 0.70 \\
\alpha_n &= 1 + 0.085 - (0.313 + 0.62(T - 0.70))(T - 0.70) && \text{for } T > 0.70
\end{aligned}$$

The equation is derived from experimental data for normal impacts of Al particles into Al foil. However, we used soda-lime glass particles. In order to determine the hole size distribution for the impact of glass particles into Al foil, it is necessary to know the dependency on the material of impacting particle. An equation for soda-lime glass projectiles onto Al foil at 6 km s^{-1} was experimentally determined by Hörz et al. (1993). Table 4 shows a comparison of the experimental data by Hörz et al. (1993) with the values given by Eq. (4) at a velocity of 6 km s^{-1}. For low T, the hole size obtained from Eq. (4) is in good agreement with that obtained from Hörz et al. (1993). However, for high T, the value of Eq. (4) is larger than that of Hörz et al. (1993). Since the counted number of penetration hole is dependent on the expected hole size derived from Eq. (4), the difference of material of impacting particle gives the error in the counted number of penetration holes. From Fig. 3 the number of the penetration holes derived from Eq.(4) may be overestimated roughly by 10% at the maximum.

The effect of oblique incidence of particles changes the hole size (Barker & Persechino, 1993). According to Eq. (2) we replaced D_h in Eq. (4) by $\sqrt{D_{major}D_{minor}}$ for oblique incidence to the foil targets.

From Eq. (2) and (4) we obtained the maximum hole size, D_{max}, using the highest velocity of impacting particles and the maximum size of the prepared glass spheres. As the highest velocity, we used the value of 3 km s^{-1}, because the velocities obtained by the piezo-electric sensor were 2.97 km s^{-1} and 3.15 km s^{-1}. As the maximum size of the glass spheres, we used 64 and 104 μm for 50 and 80 μm particles, respectively (see Fig. 3). The minimum hole size, D_{min}, was taken to be $0.6f$ according to the fact that the marginal penetration limit of D_h/f for Al foil was 0.6 (McDonnell & Sullivan 1992).

It should be noted that some of glass spheres can be comminuted (e.g., Cintala & Hörz, 1990, 1992). The comminution of glass spheres gives an error in our measurement. We measured how many holes on the foil were created by objects smaller than the nominal size of 50 or 80μm. The fraction of holes with diameter smaller than the initial size ranges of glass spheres were from 1% to 13% (see Fig. 3). The smaller holes are created not only by the fragments of comminuted glass spheres but also by marginal perforation of glass spheres. Thus, we estimated the fraction of counted holes created by the fragments of glass spheres was up to about 10%.

2.4 Velocity distribution of ejecta

We obtain the mass flux of ejecta with velocities higher than a given velocity as follows. The ejecta with velocities equal to or higher than the minimum detectable velocity (see Table 1) penetrated the Al foil, and left the holes. We get the number density of these holes in a unit area, n_h, in a diameter range from D_{min} to D_{max}. Then we define the true number density N_{true} as

$$N_{true} = \frac{n_h}{1 - \frac{S_{>D_{max}}}{A}} \tag{5}$$

where A and $S_{>D_{max}}$ are, respectively, the area of the aperture and the total area of holes with diameter larger than D_{max}. The mean value of $S_{>D_{max}}/A$ was ~ 0.01.

By using Eq. (1) and (5), mass flux of ejecta with velocities higher than v per unit solid angle, $M(> v)$ was obtained. The results are shown in Figs. 5 and 6. There were no ejecta penetrating the foil on No.1, No.2 and No.3 panels. In addition, there were also no ejecta penetrated the foil of 75 μm thickness on the No.4 panel in shot 2. These facts indicate that the high velocity ejecta concentrated towards the regions with azimuth angle of $-44° \leq \Phi \leq 44°$. This is due to oblique incidence of projectiles. Since the principal change caused by increasing obliquity is a gradual enhancement of the highest-velocity components of ejecta into downrange azimuths (Gault & Wedekind, 1978), the high velocity ejecta concentrated on No.4 and No.5 panels. The flux on No.5 panel is higher than that on No.4 panel (Figs. 5 and 6). No.5 panel was set at higher zenith angle than No.4 panel (see Table 2).

It should be noted that the upturns to positive slope of mass flux distribution as a function of v are seen in some regions on graphs of Figs. 5 and 6. On the bottom graph of Fig. 5, for instance, the mass flux is greater at 1.68 km s^{-1} than it is at 1.22 km s^{-1}. These data sets at different velocities were not obtained simultaneously in the same shot at the same direction, but were derived from measurements for the Al foil of different thicknesses. For each shot there must be the statistical scatter in the experiment. It is likely that the upturns to positive slope were due to the statistical scatter.

2.5 Comparison with extrapolation of a relation determined for low velocity ejecta

Based on a dimensional analysis, the volume of ejecta with velocities higher than v is expressed by a power law function of $V_t(> v) \propto v^{\alpha}$ (Housen et al., 1983). In the previous works, the power law index α was obtained for ejecta with lower velocity. We will compare our results with the value extrapolated from this formula. For a comparison based on the scaling law of Housen et al. (1983), it is necessary to know the total volume of ejecta with velocity higher than v, $V_t(> v)$. However, the particles ejected toward the regions covered with no panels were not detected in our experiments. In addition, no data was available for the missing regions of the Al foil (that is to say, inside the holes). The area fraction of the missing regions due to the disruption averaged about 22% of the total area of the foil on No.4 and No.5 panels. In order to estimate the total volume of ejecta, it is necessary to interpolate and extrapolate the flux of ejecta over these regions.

We interpolated and extrapolated the flux as follows: The spatial distribution of ejecta was fitted by spherical harmonics,

$$f(\Theta, \Phi) = \sum_{l=0}^{2} Y_l^m(\Theta, \Phi) \tag{6}$$

where $Y_l^m(\Theta, \Phi)$ is the surface harmonic of the first kind. The shape of spatial distribution of ejecta was assumed to be smooth, and here we neglected the terms with $l \geq 3$ in the spherical harmonics. Since there were no ejecta penetrated on the foil on No.1, No.2 and No.3 panels, the flux at $\Theta = 0°$ was zero. Only with this assumption, the fitting function for the hole number of the Al foil has a peak of the flux at $\Phi \approx 90°$. In this case, the extrapolation to the outside of panels can overestimate the total volume of the ejecta. At zenith angles smaller than 41° the fluxes with $\Phi \geq 69°$ and $\Phi \leq -69°$ were zero. The high velocity ejecta concentrated into downrange azimuths, as mentioned in Sect. 2.4. Therefore, we assumed that the fluxes at Φ=90° and -90° were zero.

We fit our data to Eq. (6) with these assumptions by using least-squares fitting. The results are shown in Fig. 7. From the fitting results, we get the total volume of ejecta, $V_t(> v)$, for the Al foil with each thickness. It should be noted that the marginal velocity of the penetrated particles depends on the position

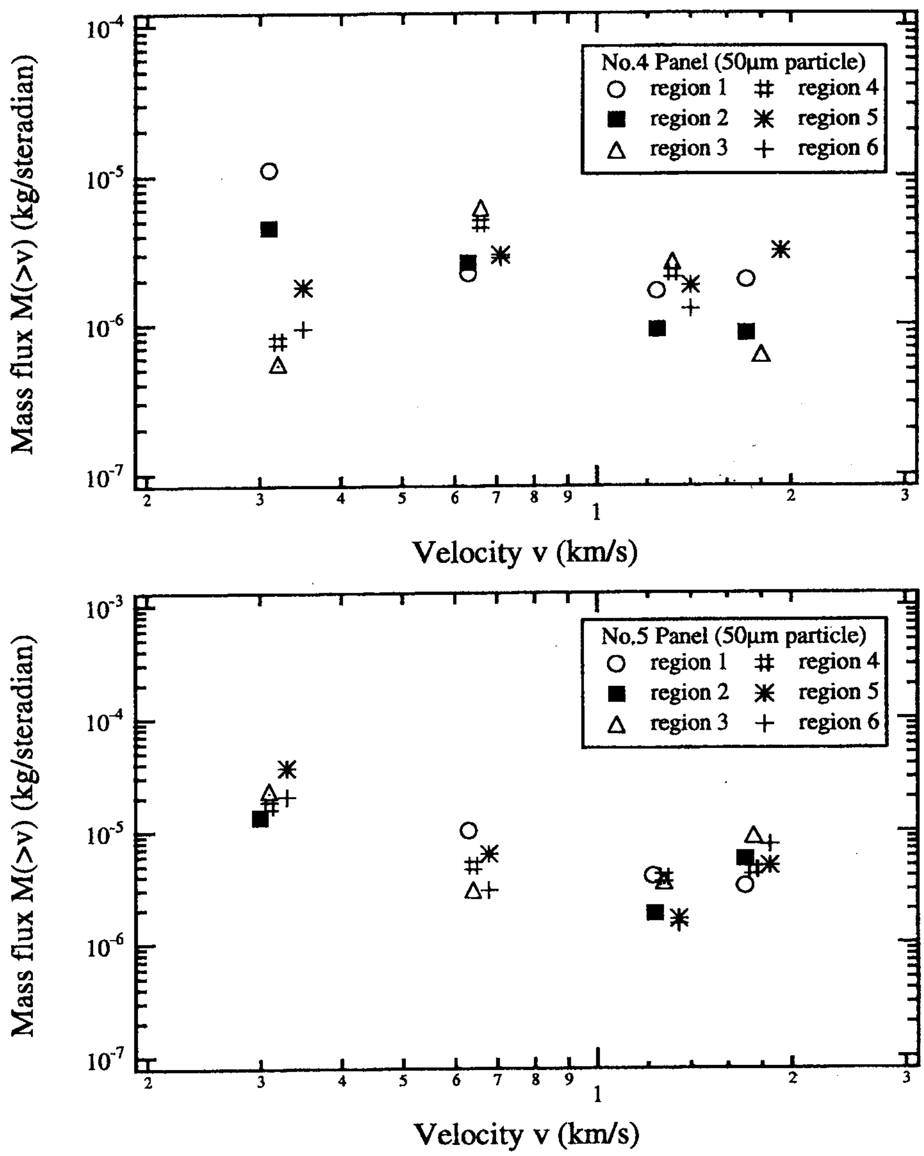

Figure 5: Mass flux of ejecta with velocity higher than v per unit solid angle. The median diameter of glass powder is $50\mu m$.

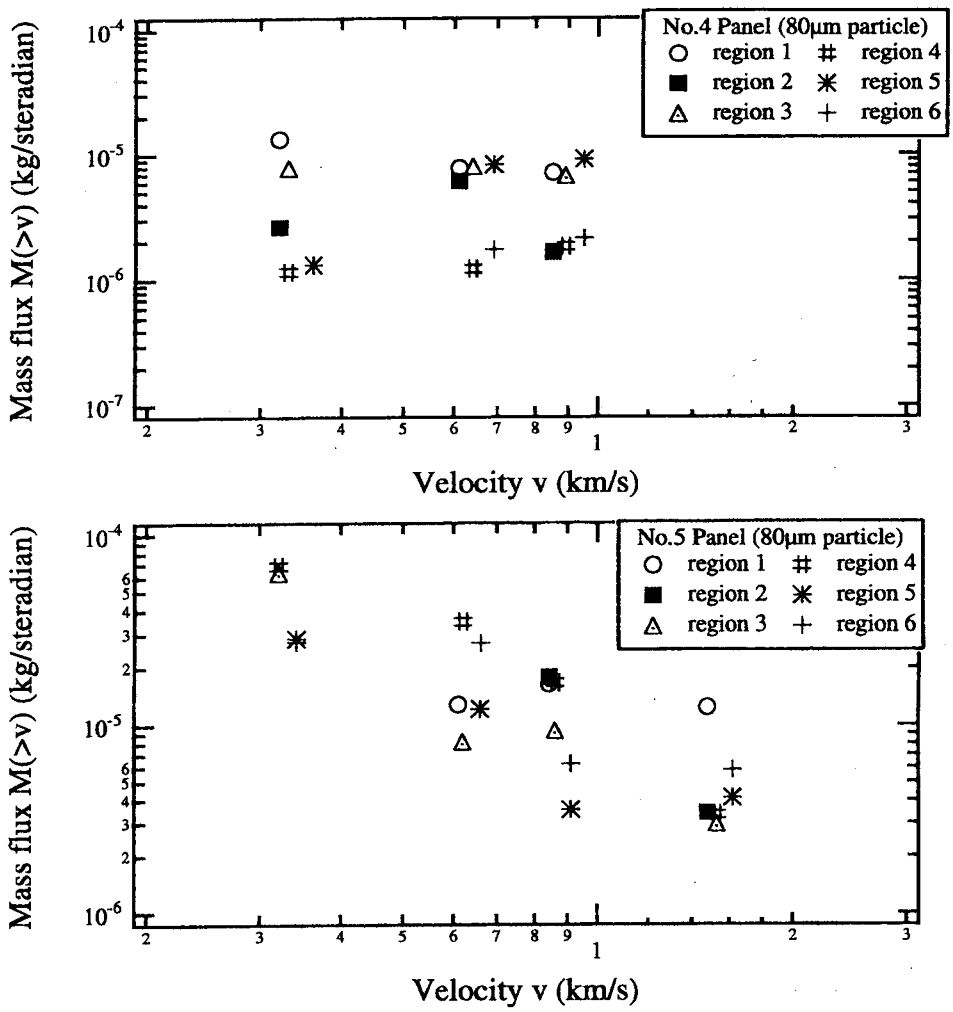

Figure 6: The same as in Fig. 5, but $80\mu m$-diameter glass powder.

of penetration on the Al foil, due to the difference in incident angle (θ) of the penetrating particles. Since the minimum incident angle θ is 60°, the effect of oblique impact is sufficiently small relative to the range of ejecta velocities. Thus, during the fitting, we assumed that the effect of the oblique incidence of penetrating particles on the relative velocity difference was negligible.

In order to calculate the nondimensional volume of ejecta, we need to know the crater radius R. However, the ejecta which do not have sufficient velocity to perforate the Al foil returned onto the target pile, and then covered the crater. It was impossible to measure the crater size directly after shot. Consequently, we derived the crater radius as follows.

According to Schmidt & Holsapple (1982), crater radius R for particulate targets was obtained from the following relation,

$$0.62\left(\frac{R_{90^\circ}}{a}\right)\left(\frac{\delta_{bulk}}{\rho_p}\right)^{1/3}\left(\frac{3.22ga}{U^2}\right)^{0.167} = 0.847 \tag{7}$$

where ρ_p and δ_{bulk} are, respectively, the density of projectile and the bulk density of sand target, U and a are, respectively, the velocity and the diameter of projectile, and g is gravity. The radius of a crater formed by an oblique impact, R_β is related to the radius of a crater formed by a normal impact, R_{90°

$$R_\beta = R_{90^\circ}\sin^{1/3}\beta \tag{8}$$

where β is an incident angle from the surface of a sand target (Gault & Wedekind, 1978). This formula is simplified. While it is not valid at very oblique angles of incidence of projectile, it has negligible error for incident angles $\geq 30°$. From Eq.(7) and (8) we estimated that crater radius R_β was from 8.1cm to 8.3cm according to the projectile's velocity. With $V_t(> v)$ and R_β, we get the nondimensional volume of ejecta with velocity greater than a given velocity (Fig. 8). Housen et al. (1983) obtained a scaling formula based on the low velocity data of ejecta from impact cratering experiments of sand targets. Their result is expressed as $V_t/R^3 = 0.32 \times (v/\sqrt{gR})^{-1.22\pm0.02}$. The effect of gravity constant in this scaling formula is not examined in the following. For comparison, the data they used are plotted in Fig. 8. Hartmann (1985) measured the velocity distribution of ejecta from impacts into regolith. Their data was not expressed in the scaling formula. We estimated the nondimensional form from their data. The result is also shown in Fig. 8. Our experiments were oblique impacts of projectiles into the targets. Though our results, shown in Fig. 8, lie below the extrapolation of the scaling formula based on the low velocity data of ejecta (Housen et al., 1983), the differences were within about one order of magnitude. There is a downturn in slope for the higher velocity ejecta in the data Housen et al. (1983) used. A line drawn through this would pass through or underneath our data set. If we assume that the crater radii are halves of the values estimated above then our data set will shift upward by a factor of eight. In this case the line of scaling formula of Housen et al. (1983) would pass through our data set. These different data sets of higher and lower velocity ejecta may be connected.

As a lower limit, the data without extrapolation for the regions covered with no panels are also shown in Fig. 8. The total volumes of ejecta derived from the fitting are higher by a few times than the data set without the interpolation and extrapolation. The disruption of Al foil is usually due to a large number of ejecta. Therefore the interpolation to the missing regions of the Al foil due to the disruption led to the major increase of total volume of ejecta. Thus, the extrapolation to the regions covered with no panel gave the slight increase of the total volume of ejecta (see Fig. 8).

Error bars in Fig. 8 were determined as follows. The number of the penetration holes derived from Eq.(4) was overestimated by 10% at a maximum due to the material difference between aluminum and glass, as mentioned in Sect. 2.3. The overlapping probability was estimated to be around 10%. In addition, the comminution of glass sphere gives an error of measurement, up to about 10%, as mentioned in Sect. 2.3. However, these errors are sufficiently small relative to the error in the fitting of the data set. Figure 7 shows differences between the fitting results and experimental data. The standard deviations of the differences were factors between 1.65 and 2.86. In summary, the error in the fitting of the data set is a major source of uncertainty in the results reported here. The error bars associated with the fitting error are shown in Fig.

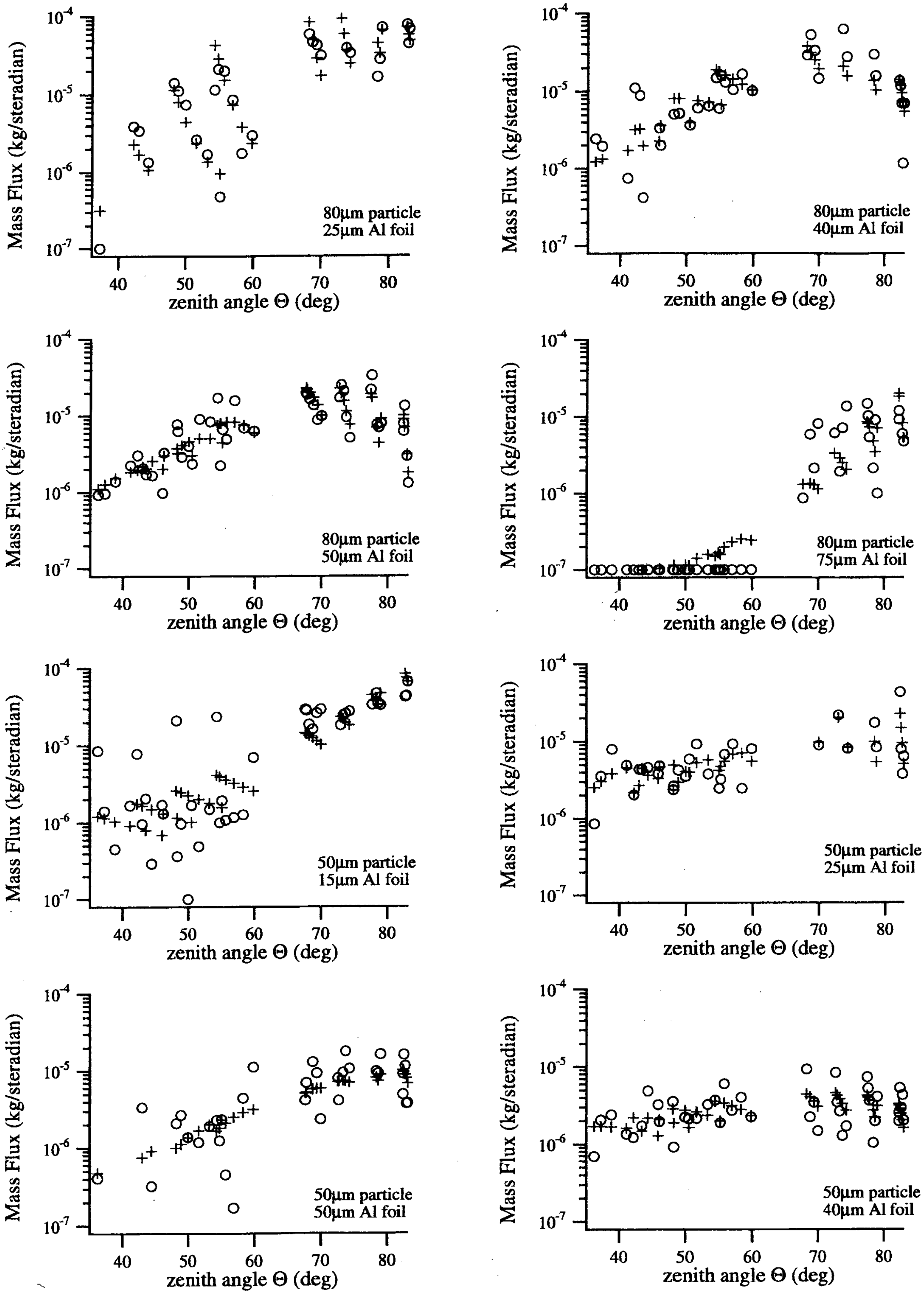

Figure 7: A comparison between the fitting data (cross symbol) and the experimental data (open circle).

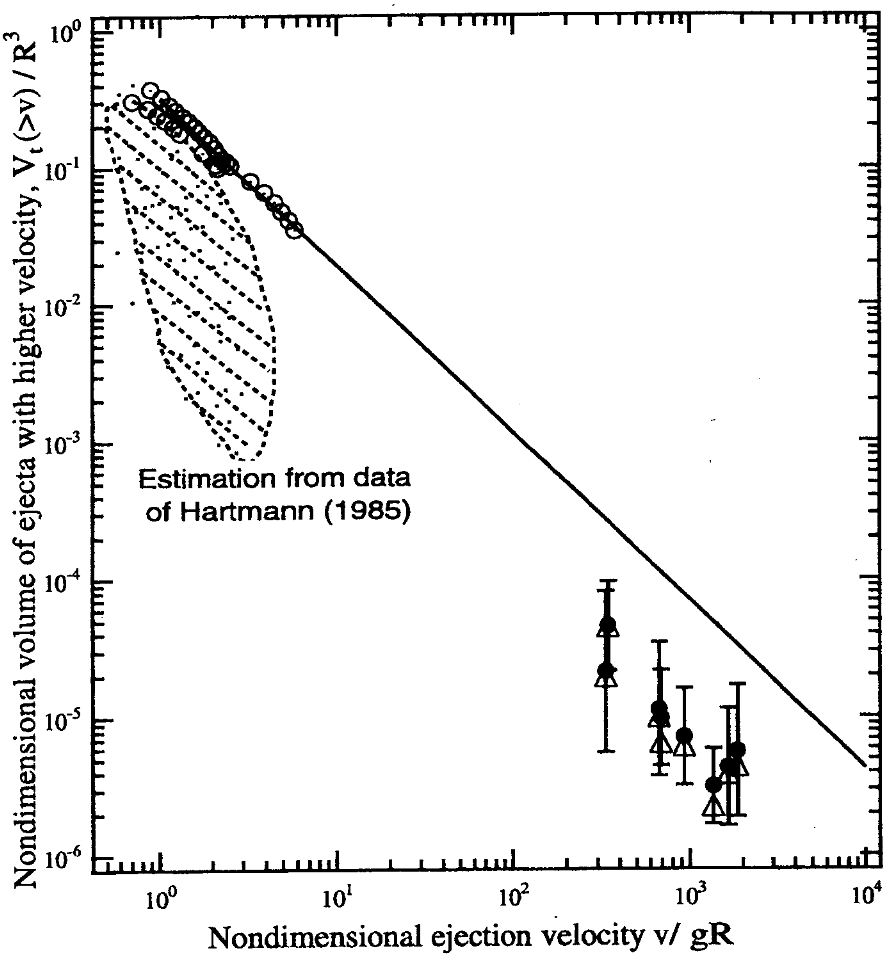

Figure 8: The volume of ejecta with velocity greater than a given value (filled circle). For comparison, a scaling formula based on the low velocity data (open circle) of ejecta from impact cratering experiments of sand targets (R=12.7cm and 11.3cm)(Housen et al., 1983)(solid line), and data obtained for ejecta from experimental impacts into sand targets (R = 1.95cm ~ 8.9cm) (Hartmann, 1985) are also shown. As a lower limit, the data with only the interpolation (see text) are also shown (open triangle).

8. Because of the error in velocity estimation by using Eq.(1), the data set can shift horizontally within a factor of 2.5 (Nakamura et al., 1994).

2.6 Summary

This paper presents spatial and velocity distributions of powdery ejecta with velocity higher than several hundred m s^{-1} by counting holes on Al foil exposed to the ejecta. According to the estimated hole size based on empirical formulae, only the penetration holes were sorted out and counted. We estimated the ejection velocity with the aid of an empirical formula for threshold penetration. The high velocity ejecta concentrated toward downrange azimuth of impacting projectile. This is due to oblique incidence of projectiles. In order to estimate the total volume of ejecta with velocity higher than a given velocity, the measured spatial distributions were extrapolated to the regions where no Al foil target was exposed, and were interpolated to the missing regions of Al foil due to the disruption. The major source of uncertainty in our results was the error in the fitting. The results were compared with the data of powdery ejecta with lower velocity and a scaling formula based on the data of low velocity ejecta from sand targets (Housen et al., 1983; Hartmann, 1985). Our experiments were oblique impacts of the projectiles to the targets. However, the differences between our results for ejecta with higher velocity and the extrapolation from the results of ejecta with lower velocity were within about one order of magnitude. These different data sets of higher and lower velocity ejecta may be connected. In order to clarify the effects of oblique impact on the spatial and velocity distribution of ejecta with high ejection velocity, further investigations are required.

In previous works the velocity distributions of powdery ejecta were obtained only for a lower range of ejection velocities. These results provide the flux of ejecta escaping from the gravitational field of bodies of diameter smaller than tens of km. This paper presents velocity distribution of powdery ejecta with velocity higher than several hundred m s^{-1}. These velocities correspond to escape velocities of bodies with diameter of hundreds of km to thousands of km. Consequently, our new results make it possible to derive the continuous fluxes of ejecta escaping from the gravitational field of larger target bodies covered with regolith layers, such as the Moon or larger asteroids.

The sizes of the Centaurs objects are tens of km to hundreds of km in diameter (Stern & Campins, 1996). It has been suggested that Chiron, which belongs to the Centaurs groups, has thin regolith layer (e.g., Luu et. al, 1994; Stern & Campins, 1996). These objects are considered to originate in the Kuiper belt. Thus, our new data may provide useful information for studies of the surface evolution of Centaurs and the Kuiper belt objects.

Acknowledgement We are grateful to E. Asphaug and I. Giblin for giving valuable comments and suggestions as reviewers. We are also grateful to H. Iglseder for setting his piezo-electric sensors. We thank K. Tomeoka and T. Kojima for allowing us to use their transmission microscope and scanning electron microscope. We also thank A. Fujiwara of the Institute of Space and Astronautical Science, for giving us opportunities of using of the two-stage light-gas gun. This work has been partially supported by the Inamori-Foundation Grant and by the Grant-in-Aid for Scientific Research of the Ministry of Education, Science, and Culture of Japan.

References

Alexander, M., Anz, P., Lyons, D., et al., 1984, Adv.Space Res., 4, 23.

Asada, N., 1985, J. Geophys. Res., 90, 12445.

Baker, J.R., Persechino, M.A., 1993, Int. J. Impact Engng, 14, 73.

Binzel, R.P., Xu., S. 1993, Science, 260, 186.

Braslau, D., 1970, J. Geophys. Res., 75, 3987.

Cintala, M.J, Hörz, F., 1990, Meteoritics 25, 27.

Cintala, M.J, Hörz, F., 1992, Meteoritics 27, 395.

Gault, D.E., Wedekind, J.A., 1978, Proc. Lunar Planet. Sci. Conf., 9th, 3843.

Gehring, J.W., 1970, High Velocity Impact Phenomena (edited by Kinslow, A.), pp. 105. Academic Press, New York.

Greenberg, R., Wacker, J.F., Hartmann, W.K., Chapman, C.R., 1978, Icarus, 35, 1.

Hartmann, W.K., 1985, Icarus, 63, 69.

Hörz, F., Cintala, M.J., Bernhard, R.P., See, T.H., 1993, Int. J. Impact Engng, 14, 347.

Housen, K.R., Schmidt, R.M., Holsapple, K.A., 1983, J. Geophys. Res., 88, 2485.

Ishimoto, H., Mukai, T., 1994, Planet. Space. Sci., 42, 691.

Ishimoto, H., 1996, Icarus, 122, 153.

Juhász, A., Tátrallyay, M., Gévai, G., Horányi, M., 1993, J. Geophys. Res., 98, 1205.

Luu, J., Jewitt, D., Cloutis, E., 1994, Icarus, 109, 133.

Mann, C.J., Kanagy II, S.P., 1990, Geology, 18, 358.

McDonnell, J.A.M., Sullivan, K., 1992, Hypervelocity Impacts in Space (edited by McDonnell, J.A.M.), pp. 39, Unit for Space Sciences, University of Kent (Canterbury).

Melosh, H.J., 1984, Icarus, 59, 234.

Melosh, H.J., 1985, Geology, 13, 144.

Nakamura, A.M., Fujiwara, A., Kadono, T., 1994, Planet. Space Sci., 42, 1043.

Pailer, N., Grün, E., 1980, Planet. Space Sci., 28, 321.

Schmidt, R.M., Holsapple, K.A., 1982, Geol. Soc. Amer. Spec. Pap., 190, 93.

Statham, I., 1974, Sedimentology, 21, 149.

Stern, A., Campins, H., 1996, Nature, 382, 507.

Warren, P.H., 1994, Icarus, 111, 338.

Yanagisawa, M., Itoi, T., 1994, Proc. of the seventy-five years Hirayama asteroid families: The role of collisions in the solar system history. in A.S.P. Conference series 63 (Edit by Kozai, Y., Binzel, R.P., & Hirayama, T.), pp. 243.

	k		
	0	1	2
50μm particles	0.951	0.047	0.001
80μm particles	0.879	0.110	0.007

Table 3: The overlapping probability for c=500. The values of k=1, 2 and 3 correspond to single (no overlaps), double and triple impacts, respectively.

Impact particle diameter (μm)	Target thickness (μm)	Hole diameter (μm) Eq.(4)	Hole diameter (μm) (Hörz et al., 1993)
80	25	174	170
	40	211	193
	50	231	204
	75	259	227
50	15	107	105
	25	132	121
	40	157	136
	50	164	144

Table 4: Comparison of the experimental data by Hörz et al. (1993) with the values given by Eq.(4) at a velocity of 6 km s^{-1}.

3 New Model of Continuous Dust Production from the Lunar Surface

S.Yamamoto & A.M.Nakamura
submitted to *A&A*, (1998)

Abstract

We estimate production rate of lunar ejecta escaping from the Moon, taking into account probable surface condition of the Moon, i.e., regolith layer. The mass production of lunar ejecta from the particulate surface is more effective compared with that from hard surface. In the previous studies based on the hard surface model (Alexander et al. 1984; Yamamoto & Mukai 1996), the maximum sizes of lunar ejecta are estimated to be a few μm. On the other hand, our new results suggest that, in addition to micron and submicron ejecta, the lunar ejecta with radii larger than tens of μm can escape from the Moon. These large grains from the Moon may contribute to the IDPs collected in the upper atmosphere of the Earth.

3.1 Introduction

Continuous bombardment of interplanetary meteoroids onto airless bodies, such as the Moon and Martian satellite, results in enhancement of dust in the vicinity of the planetary bodies and can result in formation of dust rings (e.g. Alexander et al. 1984; Ishimoto 1996; Yamamoto & Mukai 1996). Impact ejecta with having enough ejection velocity to escape from the Moon (the so-called "lunar ejecta") evolve their orbits under the effects of the gravitational forces, mutual collisions, solar radiation pressure, Poynting-Robertson effects, and electromagnetic forces in the Earth-Moon system. These dynamical processes depend strongly on the grain size as well as its shape and material component. In order to study the contribution of lunar ejecta to zodiacal cloud and IDPs collected in the stratosphere of the Earth, it is important to investigate the production process of lunar ejecta as a function of size.

In previous studies of lunar ejecta, the surface of the Moon is treated as hard rock and the velocity distribution of ejecta from hard surface is incorporated (e.g. Alexander et al. 1984; Yamamoto & Mukai 1996). Alexander et al. (1984) formulated the cumulative flux of lunar ejecta based on the results of impact experiments onto rocky targets. Their model assumes that the size distribution of lunar ejecta was $n_{esc}(a) \propto a^q$ where a is radius of lunar ejecta and power law index q was $3.43 - 3.49$, which was obtained by impact experiments onto rocky targets (e.g. Zook et al. 1975). Namely, in Alexander et al. model, the size distribution of lunar ejecta produced by the impacts of interplanetary meteoroids with various sizes was assumed to be the same as that of fragments produced by a single impact of one particle. On the other hand, Yamamoto & Mukai (1996) derived the cumulative flux of lunar ejecta from hard surface, summing all the escaping ejecta produced by impacting particles with various sizes. Both in the models of Alexander et al. (1984) and Yamamoto & Mukai (1996), the lunar ejecta with radii larger than a few μm cannot escape from the Moon due to their low ejection velocities.

Real surface of the Moon is covered by regolith layer. Large meteoroids excavate deeper, hard rock regions. On the other hand, continuous impacts of interplanetary meteoroids, which provide continuous flux of lunar ejecta, produce craters in the regolith layer. The lunar regolith has a wide range in size distribution (McKay et al. 1991). If the size of particles in the layer is much larger than that of an impacting particle, an impact crater is produced on individual grain of the layer. This case corresponds to the hard surface model. On the other hand, if the size of particles at impact site is smaller than that of an impacting particle, the production process of lunar ejecta should be investigated based on the cratering on particulate surface.

In the following, we first derive the mass production rate of the lunar ejecta both for hard surface and for particulate surface and compare two cases in Sect. 3.2. We refer to crater scaling formulae (e.g. Holsapple & Schmidt 1982; Schmidt & Holsapple 1982; Housen et al. 1983) and recent experimental result on regolith-like targets (Yamamoto & Nakamura 1997). Based on the resulting mass production rate, we estimate the cumulative flux of lunar ejecta as a function of size in Sect. 3.3. We assume that the size distribution of the lunar ejecta is related to that of the lunar soil sample (McKay et al. 1991) from the Moon. Summary of our results is presented in Sect. 3.4.

3.2 Mass production rate of the lunar ejecta

Before we estimate the size distribution of the lunar ejecta from the particulate surface, it is important to show how the production of lunar ejecta for case of the particulate surface becomes effective compared with that of hard surface. Thus, we estimate the total mass production rate of the lunar ejecta produced by continuous impacts of interplanetary meteoroids in this section. The results are also used to estimate the production rate of the lunar ejecta as a function of size in Sect. 3.3.

The major part of the interplanetary meteoritic mass impacting onto the Moon is in particles of mass 10^{-13}kg to 10^{-1}kg (Grün et al. 1985, Fig. 3). This means that the interplanetary meteoroids with masses ranging from 10^{-13}kg to 10^{-1}kg mainly contribute to the continuous production of lunar ejecta. The equivalent radii range from a few micron to a few centimeter. On the other hand, the lunar regolith layer has a wide range in size distribution (McKay et al. 1991). Therefore, the ratio of size of impacting particle to that of grains in the impact site becomes a key factor. Namely, there are two cases of the particulate surface and hard surface for the production of lunar ejecta by impacts of interplanetary meteoroids onto the regolith layer. Since the mixed processes of both cases provide the lunar ejecta from the regolith layer, it is very complicated to estimate the mass production rate of lunar ejecta rigorously. Therefore, we evaluate the mass production rate of lunar ejecta separately both for a layer of particles (a particulate surface) and for a hard surface.

We take that gravitational acceleration is $g = 1.62$ m s^{-1}, the effective meteoroid density is $\delta = 2.5 \times 10^3$ kg m^{-3} (Grün et. al 1985), and the density of the grains is $\rho_g = 3 \times 10^3$kg m^{-3} (Carrier et al. 1991). The bulk density of regolith layers ρ_b depends on the porosity. We assume that the porosity is 0.5 (Yen & Chaki 1992) and adopt $\rho_b = 1.5 \times 10^3$ kg m^{-3}. Substituting these values into Eq. (33) in Appendix A, the total mass $M(> v_e)$ of ejecta with velocity higher than v_e produced by an impact of particle with mass of m_i is derived,

$$M(> v_e) = 3.5 \times 10^2 K_3 (0.15 v_i^{0.334})^\gamma v_e^{2(3-\gamma)} m_i^{\frac{0.833\gamma}{3}}, \tag{9}$$

where v_i is impact velocity of interplanetary meteoroids, K_3 is a constant, $\gamma = 3 + e_v/2$, and e_v is a constant exponent. Housen et al. (1983) reported $K_3 = 0.32$ and $e_v = 1.22$ based on the low velocity data ($\sim$m s^{-1}) of experimental investigation onto sand targets. On the other hand, Yamamoto & Nakamura (1997) measured the velocity distribution of powdery ejecta with velocities higher than several hundred m s^{-1}. Their results of the total volume of high velocity ejecta lie below the extrapolation of the lower velocity data of Housen et al. (1983). When we assumed $e_v = 1.2$, we derived $K_3 = 0.03$ by fitting the data of Yamamoto & Nakamura (1997) to the same scaling formula of Eq.(30). The difference of K_3 gives the difference of the mass production rate of the lunar ejecta derived from Eq. (9). We define the former and the latter, respectively, as the upper estimation and the lower estimation of the mass production rate of lunar ejecta for the case of particulate surface.

When $e_v = 1.2$, $0.833\gamma/3 \sim 1$. In this case, Eq.(9) can be expressed as

$$M(> v_e) = 3.5 \times 10^2 K_3 (0.15 v_i^{0.334})^\gamma v_e^{2(3-\gamma)} m_i. \tag{10}$$

For the case of hard surface, $M(> v_e)$ is derived from (37) in Appendix B,

$$M(> v_e) = 1.3 \times 10^2 Y^{-0.709} v_i^{1.42} \left(\frac{v_e}{v_{min}}\right)^{-2} m_i, \tag{11}$$

where v_{min} is minimum velocity of fragments from the crater and depends on the strength of grain Y. The velocity distribution of ejecta from rocky target has been derived from the impact experiments into basalt targets by Gault et al. (1963). Based on the results of experiment of Gault et al.(1963), Housen (1992) inferred $v_{min} = 45$ m s^{-1}. In addition, Housen et al. (1983) inferred $Y = 8.8 \times 10^7$ Pa for the basalt target used by Gault et al. (1963). In this case, Eq.(11) is

$$M(> v_e) = 0.61 v_i^{1.42} v_e^{-2} m_i. \tag{12}$$

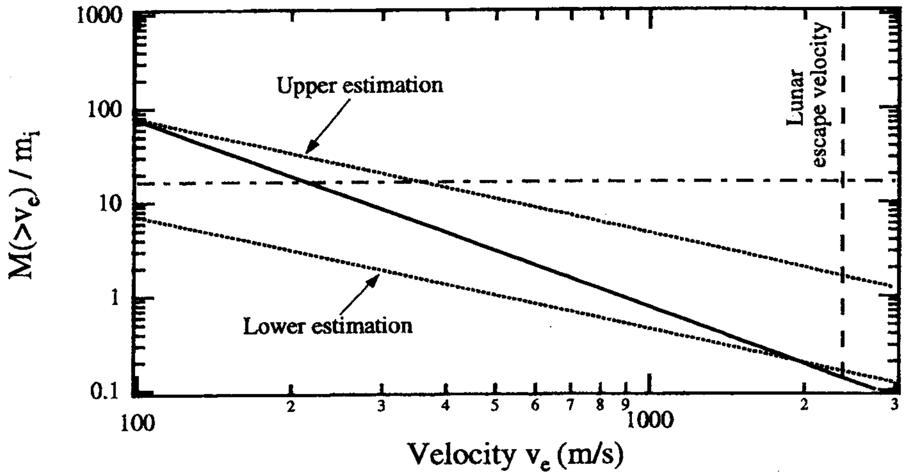

Figure 9: Ratio of mass production rate of ejecta with velocities higher than a given velocity to a mass of impacting particle for the cases of particulate surface (dotted line) and hard surface (solid line). The dash-dotted line indicates M_m/m_i for $v_i = 20$ km s^{-1}. The vertical dashed line indicates the lunar escape velocity (~2.38 km s^{-1}).

In the analysis of flux of interplanetary meteoroids, Grün et al. (1985) assumed that the effective velocity between different meteoroids onto the Moon is 20 km s^{-1}. However, some of excavated material melt due to hypervelocity impact of $v_i \doteq 20$ km s^{-1}. Based on the results of O'keefe & Ahrens (1982), when $v_i > 12$ km s^{-1}, the ratio of the mass of melted material M_m to m_i is approximately by Melosh (1989),

$$\frac{M_m}{m_i} = 0.14\frac{v_i^2}{\epsilon_m}, \tag{13}$$

where ϵ_m is the specific internal energy for melting the target material. Substituting $\epsilon_m = 3.4 \times 10^6$ J kg^{-1} for gabbroic anorthosite (Melosh 1989) and $v_i = 20$ km s^{-1}, we obtained $M_m/m_i \sim 16$. Substituting $v_i = 20$ km s^{-1} into Eqs.(10) and (12), $M(> v_e)/m_i$ is calculated as a function of v_e for both cases of particulate surface and hard surface (Fig. 9). From Fig. 9, the values of $M(> v_e)/m_i$ at $v_e = 2.38$ km s^{-1} are less by two orders of magnitude than the resulting value of M_m/m_i (dash-dotted line). This indicates that most of the lunar ejecta escaping from the Moon melt for the case of $v_i = 20$ km s^{-1}. In this case, we have no warrant for using the scaling law of ejection velocity distribution in Eqs. (30) and (35) to estimate the amount of lunar ejecta.

According to Ahrens & O'Keefe (1977), when $v_i = 5$ km s^{-1}, the peak shock pressure is slightly lower than the threshold pressure to induce melting. In this case, the lunar ejecta can escape from the Moon without melting or vaporization. Zook (1975) reviews several reports of impact velocity of meteoritic material onto the Moon based on meteor velocity observations. He reported that the impact velocity on the Moon ranges from 2.78 km s^{-1} to more than 50 km s^{-1}. Although the major part of bombardments with average impact velocity of 20 km s^{-1} induce the melting, the impacts of $v_i \leq 5$ km s^{-1} provide the lunar ejecta without melting or vaporization. Therefore, we estimate the production rate of the lunar ejecta at $v_i = 5$ km s^{-1}.

Substituting $v_i = 5$ km s^{-1} into Eqs.(10) and (12), $M(> v_e)$ is derived as

$$M(> v_e) = 3.5 \times 10^2 K_3 2.6^{\gamma} v_e^{2(3-\gamma)} m_i, \tag{14}$$

for the case of particulate surface, and

$$M(> v_e) = 1.1 \times 10^5 v_e^{-2} m_i, \tag{15}$$

	production rate of lunar ejecta
particulate surface	$5.3 \times 10^{-6} \sim 4.9 \times 10^{-5}$ [kg s^{-1}] (depending on the values of K_3 and e_v)
hard surface model	3.5×10^{-6}[kg s^{-1}]
Alexander et al. (1984) model	4.8×10^{-5} [kg s^{-1}] ($v_i \sim 20$ km s^{-1})

Table 5: The mass production rate of lunar ejecta both for the case of a particulate surface and for a hard surface ($v_i = 5$ km s^{-1}). For comparison, the result of hard surface model by Alexander et al. (1984) ($v_i \sim 20$ km s^{-1}) is also given.

for the case of hard surface. By using Eqs.(14) and (15), we calculate the mass production rate of lunar ejecta, $P_t(> v_{esc})$, where the lunar escape velocity is $v_{esc} = 2.38$ km s^{-1} as,

$$P_t(> v_{esc}) = S \int_{i_{min}}^{i_{max}} f(m_i) M(> v_{esc}) dm_i, \tag{16}$$

where $f(m_i)dm_i$ is the flux of interplanetary meteoroids with masses between m_i and $m_i + dm_i$ for $v_i = 5$ km s^{-1}, i_{max} and i_{min} are, respectively, a maximum mass and minimum mass of interplanetary meteoroids, and S is the total area of lunar surface. We use the mass distribution of the interplanetary flux model derived by Grün et al. (1985). According to Fig. 3 in Zook (1975), the fraction of interplanetary meteoroids with $v_i \leq 5$ km s^{-1} is about a few percents. For simplicity, the absolute magnitude of meteoroid flux with $v_i = 5$ km s^{-1} is assumed to be 1% of that of interplanetary flux model with $v_i = 20$ km s^{-1}. Since the major part of the interplanetary meteoric mass are in particles of mass 10^{-13}kg to 10^{-1}kg, we set that i_{min} and i_{max} are, respectively, 10^{-13}kg and 10^{-1}kg. We assume that the impact of interplanetary meteoroids onto the Moon is isotropic (Grün et al. 1985) and $S = 3.8 \times 10^{13}$m^2. Substituting these values into Eqs.(14), (15), and (16), the mass production rate of lunar ejecta is derived (Table 5).

The mass production rate of lunar ejecta for the case of particulate surface is higher than that of the hard surface. Alexander et al. (1984) have estimated that the mass production rate of the lunar ejecta, based on results of impact experiments onto rocky targets. They do not take into account melting due to hypervelocity impacts, and used the interplanetary flux model with $v_i \sim 20$ km s^{-1}. While our results for the case of hard surface model are lower than that of Alexander et al. (1984), due to our use of $v_i = 5$ km s^{-1}, the maximum value of total production rate for the case of particulate surface is comparable to that of Alexander et al. (1984). Consequently, the production of lunar ejecta from the particulate surface is more effective compared with that for the case of hard surface.

3.3 Production rate of the lunar ejecta as a function of size

In this section, we estimate the production rate of the lunar ejecta as a function of size for the case of particulate surface. We determine the size distribution of lunar ejecta for the $M(> v_{esc})$ in Eqs.(14) as following.

We assume that the size distribution of lunar ejecta is related to that of the lunar surface soil. In this study, we use three typical lunar soil samples of 71501,1 Mare, 73261,1 Massif, and 78421,1 Massif of Apollo 17 soils (McKay et al. 1991, Fig. 7.9). Some of original grains are comminuted during cratering processes (Cintala & Hörz 1990; 1992). The comminution of original grains changes the size distribution in the lunar soil. According to Cintala & Hörz (1990), the comminuted target mass M_c due to an impact of particle with radius a and velocity v_i is given by an equation of the form

$$M_c = 1.2 \times 10^{-2} \delta^{5.72} \rho_b^{-5.20} (2a)^{1.46} k^{0.18} \mu^{0.21} s^{-0.29} (\rho_b V_{total})^{0.48} \left(\frac{v_i}{C_g}\right)^{0.65}, \tag{17}$$

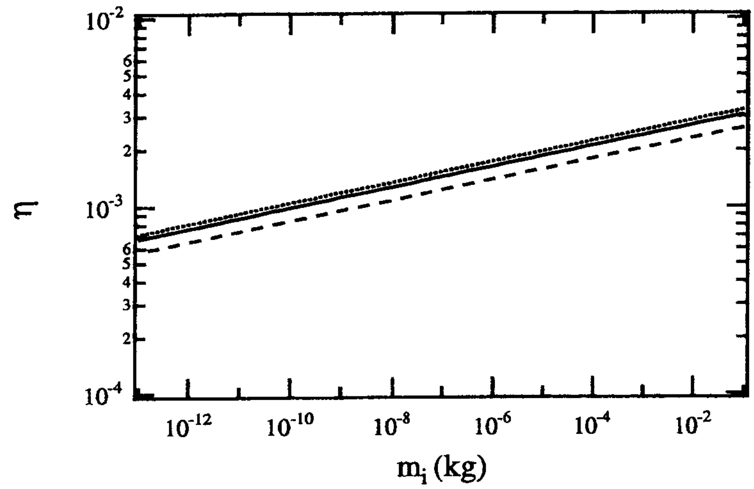

Figure 10: Ratio η of comminuted target mass to total excavated mass. Solid line, dotted-line, and dashed line correspond to 71501,1 Mare, 73261,1 Massif, and 78421,1 Massif (McKay et al. 1991), respectively.

where the mass of excavated material $\rho_b V_{total}$ is obtained from Eq.(29) in Appendix A, k and μ are, respectively, mean crystal size and mean grain size of the lunar soil, s is sorting of the grains (that is the standard deviation of the size-frequency distribution) (cf. McKay et al. 1991), and C_g is sound speed of the grains. Substituting $C_g = 2.6 \times 10^3$m s^{-1} for basalt (Melosh 1989), $v_i = 5$ km s^{-1}, $\rho_b = 1.5 \times 10^3$ kg m^{-3}, $\delta = 2.5 \times 10^3$ kg m^{-3}, and $a = (3m_i/4\pi\delta)^{1/3}$ into Eq.(17), the ratio η of M_c to $\rho_b V_{total}$ is,

$$\eta = \frac{M_c}{\rho_b V_{total}} = 7.6 \times 10^{-3} k^{0.18} \mu^{0.21} s^{-0.29} m_i^{0.055}. \quad (18)$$

For each lunar soil sample, μ and s are given in Carrier et al. (1991). The value of k depends on the grains' size. The value of k for the targets used by Cintala & Hörz (1990) is ranging from 3.5×10^{-4} to 2.5×10^{-3} m. For simplicity, we adopted $k = 10^{-3}$. The value of η is insensitive to the value of k in Eq.(18). From Eq.(18), the value of η is calculated as a function of m_i for each lunar soil sample (Fig. 10). The resulting η is ranging from 6×10^{-4} to 3×10^{-3}, depending on μ and s as well as m_i.

From Figs. 9 and 10, we found that the total mass of lunar ejecta is smaller than that of comminuted grains, that is $M(> v_{esc}) < M_c$. From Eqs.(14), (18), and (29), the ratio ζ of $M(> v_{esc})$ to M_c is

$$\zeta = \frac{M(> v_{esc})}{M_c} = \begin{cases} 4.5 \times 10^{-2} \mu^{-0.21} s^{0.29} m_i^{0.11}, & \text{for } K_3 = 0.32 \text{ and } e_v = 1.22. \\ 4.9 \times 10^{-3} \mu^{-0.21} s^{0.29} m_i^{0.11}, & \text{for } K_3 = 0.03 \text{ and } e_v = 1.2. \end{cases} \quad (19)$$

When the value of m_i ranges from 10^{-13}kg to 10^{-1}kg, $\zeta \ll 1$. If the fragments produced by the comminution have higher velocity compared to the ejection velocity of intact grains in the lunar soil, most of lunar ejecta are the comminuted component. In their impact experiments onto regolith targets, Yamamoto & Nakamura (1997) found that grains with velocities higher than a few km s^{-1} from powdery targets are both the original grains and comminuted fragments. Therefore, it is likely that the lunar ejecta are not only comminuted fragments but also original lunar soil grains. Since the relation between size distribution and velocity distribution of ejecta from regolith targets has not been investigated in previous impact experiments onto regolith targets, it is difficult to determine how many intact grains and comminuted grains have enough velocity to escape from the Moon. Therefore, we examine both cases of comminuted grains and intact lunar soil grains separately. When all the lunar ejecta are from the comminuted component, the largest size of the lunar ejecta becomes to be sufficiently smaller than that of original lunar grain, as shown in 3.1. On the other hand, when the size distribution of lunar ejecta is the same as that of the lunar soil samples, the larger lunar ejecta can escape from the Moon. We consider that the former case and latter case are, respectively, the minimum case and the maximum case of size distribution of lunar ejecta for the model of particulate surface.

3.3.1 Minimum case: Model for comminuted grain

In this model, the lunar ejecta are produced by the comminution of grains in the regolith layer. We assume that the fraction of comminuted grains amongst the lunar soil is independent of their size, and that the finer fragments produced by the comminution have higher ejection velocity. The maximum size of lunar ejecta depends on the peak pressure loaded on the comminuted grains. Since we consider this model as the minimum case of size distribution of lunar ejecta from the particulate surface, the grain is assumed to be comminuted under an initial (maximum) peak pressure. In this case, the grain is sufficiently destroyed into fine fragments and the size distribution of the comminuted fragments is well presented by single power law distribution (Mizutani et al. 1990). The number $n_f(a, a_c)da$ of comminuted fragments in radius ranging from a to $a + da$ is

$$n_f(a, a_c)da = C(a_c)a^{3q+2}da \propto m^q dm, \tag{20}$$

where $C(a_c)$ is a constant and a_c is the radius of original grain before the comminution. When an impact stress in grain is sufficiently high, the power law index approaches $q = -5/3$ (Mizutani et al. 1990), that is $n_f(a, a_c) = C(a_c)a^{-3}$. Assuming a spherical shape of lunar soil grain, the mass of comminuted grains is $\eta N(a_c)da_c \times 4\pi\rho_g a_c^3/3$ where $N(a_c)da_c$ is the number of grains with radii ranging from a_c and $a_c + da_c$ in the lunar soil sample derived from McKay et al. (1991). By using this, the value of $C(a_c)$ is determined by

$$C(a_c)da_c \int_{a_{c2}}^{a_{c1}} a^{-3}a^3 da = a_c^3 \eta N(a_c)da_c, \tag{21}$$

where a_{c1} and a_{c2} are, respectively, the maximum and minimum radii of the comminuted fragments. From Eqs. (20) and (21), the number of comminuted fragment is

$$n_f(a, a_c)da_c = \frac{a^{-3}a_c^3 \eta N(a_c)}{a_{c1} - a_{c2}} da_c. \tag{22}$$

The value of a_{c1} depends on the magnitude of impact stress (e.g. Fujiwara et al. 1977; Mizutani et al. 1990). According to Mizutani et al. (1990), the initial peak pressure is given by,

$$P_0 = \frac{1}{2}\xi\rho_b C_t v_i (1 + \frac{1}{2}s_t \xi \frac{v}{C_t}) \tag{23}$$

where C_t is bulk sound speed of regolith, s_t is a constant, and ξ is the parameter related to shock impedance matching. Since the value of ξ is on the order of 1 (Mizutani et al. 1990), we set $\xi = 1$ for simplicity. Substituting $C_t = 1.7 \times 10^3$m s^{-1} and $s_t = 1.31$ for dry sand (Melosh 1989), $\rho_b = 1.5 \times 10^3$kg m^{-3}, and $v_i = 5$ km s^{-1} into Eq.(23), we estimated $P_0 = 1.9 \times 10^{10}$Pa. Since the comminuted grain is smaller than impacting particle, we assume that the attenuation of the peak pressure P_0 in the grain is negligibly small and a nondimensional impact stress (NDIS) (Mizutani et al. 1990) is $P_I = P_0/Y$. Substituting the value of P_I into Eq.(34) in Mizutani et al. (1990), the mass ratio of largest fragment to original grain is $\sim 1.5 \times 10^{-4}$ for $Y = 8.8 \times 10^7$Pa. Thus, assuming spherical comminuted fragment and lunar soil grain, we got $a_{c1} = 0.05a_c$. We set $a_{c2} = 0.1\mu$m, because Asada (1985) detected the fine fragments with size of about $0.1\mu m$ in his impact experiments into basalt targets. In this case, Eq.(22) is valid ($a_{c1} > a_{c2}$), because $a_c > 2\mu$m for the lunar soil grains of McKay et al. (1991).

From Eq.(22), we calculated the size distribution $n_c(a)$ of fragments produced by the comminution of the lunar soil grains as,

$$n_c(a) = \int_{\frac{a}{0.05}}^{a_{max}} n_f(a, a_c)da_c = a^{-3}\int_{\frac{a}{0.05}}^{a_{max}} \frac{a_c^3 \eta N(a_c)}{a_{c1} - a_{c2}} da_c \tag{24}$$

lunar soil sample	largest size of lunar ejecta
71501,1 Mare	2 μm $\sim$ 20 μm
73261,1 Massif	2 μm $\sim$ 20 μm
78421,1 Massif	3 μm $\sim$ 25 μm

Table 6: The largest size of lunar ejecta from each lunar soil sample.

where a_{max} is the maximum radius of lunar soil grains. Since we assume that the size of grains in the regolith layer is smaller than that of impacting particle for the case of particulate surface, we set $a_{max} = a_i$ where a_i is a radius of impacting particle. From Eq.(14) and Eq.(24), the size distribution of lunar ejecta $n_{esc}(a, m_i)$ is derived,

$$n_{esc}(a, m_i) = \frac{M(> v_{esc})}{\int_{a_{c2}}^{a_{e1}} n_c(a') \frac{4\pi \rho_g a'^3}{3} da'} n_c(a) \tag{25}$$

where a_{e1} is the maximum radius of fragments escaping from the Moon. Eq.(25) cancels the value of η in Eq.(24). Since $M(> v_{esc}) < M_c$, the largest size a_{e1} of fragments escaping from the Moon is smaller than $a_{c1} = 0.05a_i$. Since we assume that the smaller fragments have higher ejection velocity, a_{e1} is derived by the following relation,

$$\zeta = \frac{M(> v_{esc})}{M_c} = \frac{\int_{a_{c2}}^{a_{e1}} n_c(a) \frac{4\pi\rho_g a^3}{3} da}{\int_{a_{c2}}^{0.05a_i} n_c(a) \frac{4\pi\rho_g a^3}{3} da}. \tag{26}$$

From Eqs.(26) and (19), the largest sizes of lunar ejecta for the case of $a_i = 0.02\mu$m (10^{-1} kg) are derived for each lunar soil used here (Table 6). The largest sizes of lunar ejecta are about 2 μm for the lower estimation and 20 μm for the upper estimation.

By using Eq. (25) and the flux of interplanetary meteoroids $f(m_i)$ in Eq. (16), the cumulative flux of lunar ejecta $F(a_e)$ at the lunar surface is derived,

$$F(a_e) = \int_{a_e}^{\infty} da \int_{i_c}^{10^{-1}kg} n_{esc}(a, m_i) f(m_i) dm_i, \tag{27}$$

where i_c is the minimum mass which can produce the lunar ejecta with radii of a_e. $F(a_e)$ are calculated for the cases of the lunar soil samples of 71501,1 Mare, 78421,1 Massif, and 73261,1 Massif (Fig. 11). The dotted curve and the dashed curve correspond to the upper estimation and the lower estimation of $M(> v_{esc})$ in Eq.(14), respectively. The difference of lunar soil sample (i.e., 71501,1 Mare, 78421,1 Massif, and 73261,1 Massif) does not have influence on the results in Fig. 11 significantly. For comparison, the cumulative flux of interplanetary meteoroids with v_i=20 km s^{-1} (Grün et al. 1985) (solid curve) and the cumulative flux of meteoroids at v_i = 5 km s^{-1} (dash-dotted curve) are plotted in Fig .11. The cumulative flux of submicron-sized lunar ejecta is comparable to or higher than those of interplanetary meteoroids.

3.3.2 Maximum case: Model for intact grain

Next, we assume that the lunar ejecta are the intact lunar soil grains. Since the data of lunar soil sample have no grains with radii smaller than about 2μm (McKay et al. 1991), we consider only the lunar ejecta with radii larger than 2μm. In this model, the ejection velocity is assumed to be independent of its size. Namely, the size distribution of lunar ejecta produced by one impact of meteoroid is the same as that of lunar soil in the regolith layer. Thus, the size distribution of lunar ejecta n_{esc} produced by one impact of meteoroid is derived,

$$n_{esc}(a, m_i) = \frac{M(> v_{esc})}{\int_{a_{c2}}^{a_i} N(a') \frac{4\pi\rho_g a'^3}{3} da'} N(a), \tag{28}$$

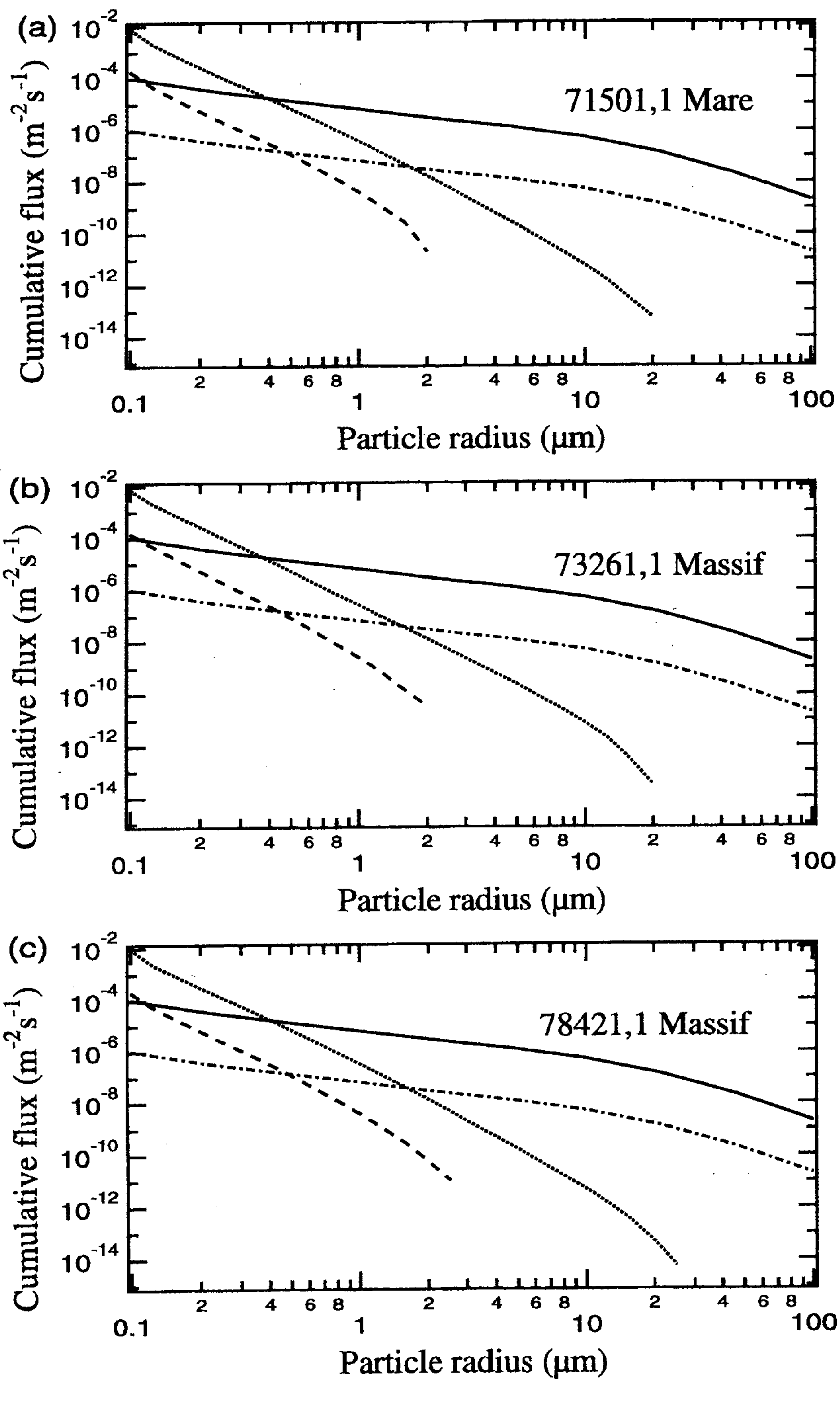

Figure 11: Cumulative flux of lunar ejecta at the lunar surface, for the model of comminuted grain. Dotted curve and dashed curve are the upper estimation ($K_3 = 0.32$ and $e_v = 1.22$) and lower estimation ($K_3 = 0.03$ and $e_v = 1.2$), respectively. We use three typical samples of lunar surface soil of (a) 71501,1 Mare, (b) 73261,1 Massif, and (c) 78421,1 Massif (McKay et al. 1991). For comparison, the interplanetary flux model (Grün et al. 1985) (solid curve) and the cumulative flux of meteoroids at $v_i = 5$ km s^{-1} (dash-dotted curve) are plotted .

where $N(a)$ is given by McKay et al. (1991). Substituting Eq.(28) into Eq.(27), we calculated the cumulative flux of lunar ejecta as a function of size for the model of intact grain (Fig. 12). We set $i_c = 10^{-13}$ kg in Eq.(27). In this model, there are the lunar ejecta with sizes larger than tens of μm escaping from the Moon. The difference of lunar soil sample does not have influence on the results in Fig. 12 significantly. For comparison, the cumulative flux of interplanetary meteoroids with v_i=20 km s^{-1} (Grün et al. 1985) (solid curve) and the cumulative flux of meteoroids at v_i = 5 km s^{-1} (dash-dotted curve) are plotted in Fig. 12. Although the cumulative fluxes of lunar ejecta escaping from the Moon lie below the interplanetary flux model of Grün et al. (1985), the maximum value of cumulative flux of micron-sized lunar ejecta becomes comparable to the interplanetary flux model.

3.3.3 Discussion

We estimated the production rate of lunar ejecta as a function of size for both cases of comminuted grain and intact lunar soil grain separately. For the model of comminuted grain (minimum case of size distribution), the largest size of the lunar ejecta ranges from about 2μm to 20μm (Table 6). On the other hand, in the previous results based on the hard surface model (Alexander et al. 1984; Yamamoto & Mukai 1996), no lunar ejecta with radii larger than a few μm escape from the Moon. Although we consider the minimum case of size distribution, the largest size of lunar ejecta for the model of comminuted grain is comparable to or greater than that for the case of hard surface.

For the model of intact grain (maximum case), the lunar ejecta with sizes larger than tens of μm can escape from the Moon. It is likely that the practical cumulative flux of the lunar ejecta lies between the minimum case and the maximum case. However, it is difficult to predict rigorously how many intact grains have enough ejection velocity to escape from the Moon as the lunar ejecta.

Based on the results of impact experiments onto regolith targets by Yamamoto & Nakamura (1997), we calculated $M(> v_e)$ of Eq.(14) and M_c of Eq.(17) for their results. We found that the resulting total mass of ejecta with velocity higher than a few km s^{-1} is smaller than the total mass of comminuted grains, that is $M(> v_e) < M_c$ at v_e of a few km s^{-1}. This is the same condition of lunar ejecta shown above. Yamamoto & Nakamura (1997) estimated that the fraction of comminution fragments was up to 10%. Most of the high velocity ejecta detected in their experiments were original grains from the regolith target. Consequently, it is likely that a large number of original lunar soil grains escape from the Moon. We conclude that, in addition to micron and submicron lunar ejecta, the lunar ejecta with radii larger than tens of μm escape from the Moon for the case of particulate surface.

Even for the impact of interplanetary meteoroids with $v_i > 5$ km s^{-1}, some ejecta may escape from the Moon without melting or vaporization. In this case, the contribution of the lunar ejecta produced by impacts of interplanetary meteoroids with $v_i > 5$ km s^{-1} are added to the results of Figs. 11 and 12. The presented results may correspond to the lower estimation on the production rate of lunar ejecta. Further investigations are required to understand melting process as well as size distribution of ejecta from regolith layers.

3.4 Summary

We estimated the production rate of lunar ejecta escaping from the Moon, taking into account the lunar regolith surface. Since most of impacts of interplanetary meteoroids onto the Moon induce melting and/or vaporization due to their hypervelocity impacts, we estimated the production rate of lunar ejecta due to the partial contribution of meteoroids at v_i=5 km s^{-1}. The mass production rate of lunar ejecta for the case of particulate surface is higher than that of hard surface. Furthermore, the maximum value of production rate for the case of particulate surface with v_i = 5 km s^{-1} is comparable to that of hard surface model of Alexander et al. (1984) with v_i = 20 km s^{-1}. Consequently, the production of lunar ejecta from the particulate surface is more effective compared with that from the hard surface.

In addition, we estimated the size distribution of lunar ejecta as a function of size for the case of particulate surface. For the hard surface model by Alexander et al. (1984) and Yamamoto & Mukai (1996), the

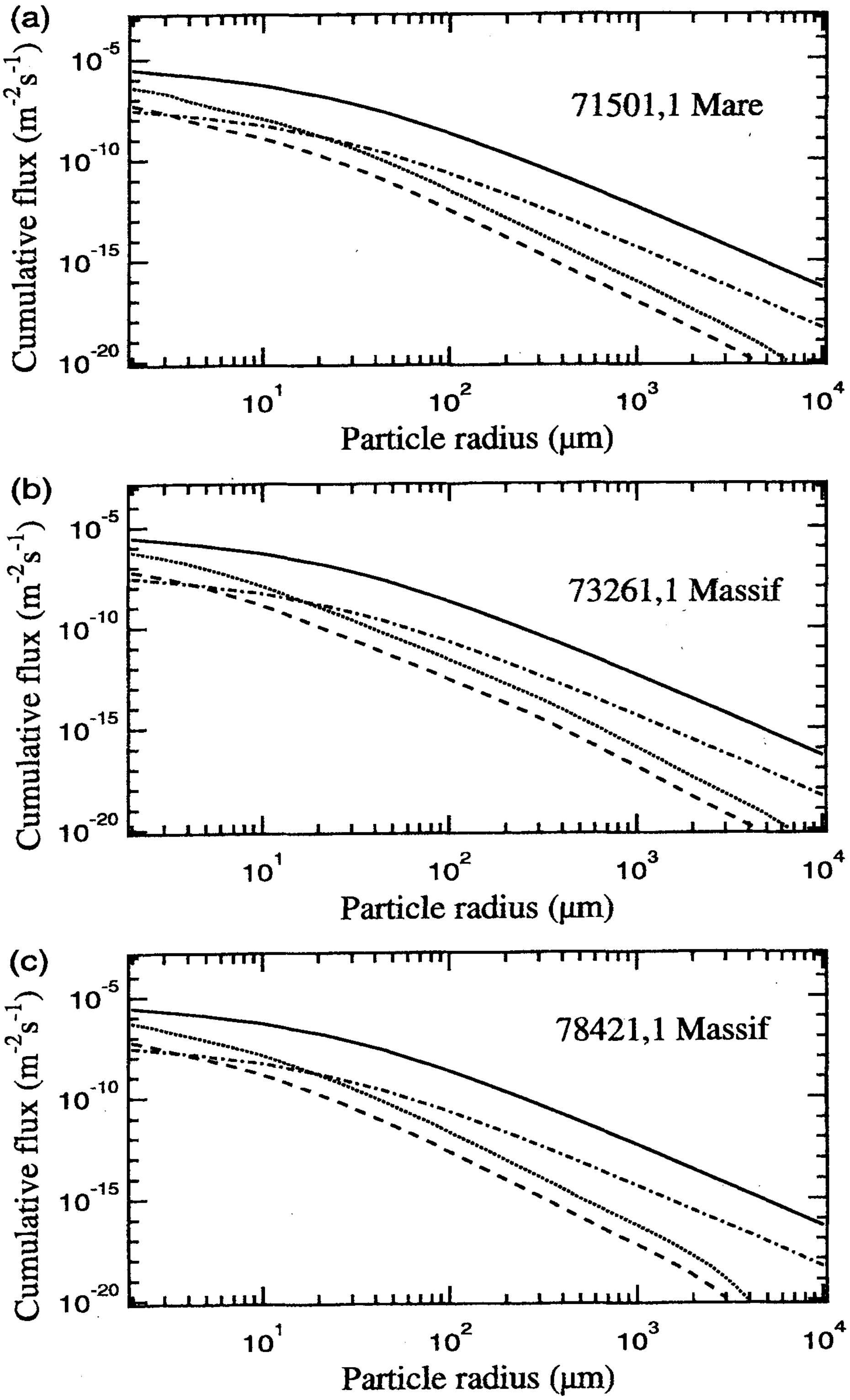

Figure 12: Cumulative flux of lunar ejecta at the lunar surface for the model of intact grain. Dotted curve and dashed curve are the upper estimation and lower estimation, respectively. We use three typical samples of lunar surface soil of (a) 71501,1 Mare, (b) 73261,1 Massif, and (c) 78421,1 Massif (McKay et al. 1991). For comparison, the interplanetary flux model (Grün et al. 1985) (solid curve) and the cumulative flux of meteoroids at $v_i = 5$ km s^{-1} (dash-dotted curve) are plotted.

maximum sizes of lunar ejecta are a few μm. On the other hand, for the case of particulate surface, the lunar ejecta with radii larger than tens of μm, as well as micron and submicron lunar ejecta, can escape from the Moon.

The lunar ejecta with sizes smaller than a few μm are significantly influenced by the solar radiation pressure (Burns et al. 1979), and some of them take hyperbolic orbits due to the solar radiation pressure. On the other hand, the large lunar ejecta with sizes of tens of μm can enter into geocentric orbits, because the effect of solar radiation pressure is too small to change their orbits significantly. Some of these lunar ejecta arrive at the Earth and may contribute to the IDPs collected in the upper atmosphere of the Earth.

Appendix A: Model of a particulate surface The first model assumes that an impact site on the Moon is covered by a layer of fine particles compared to the impacting particle. In this case, the effect of gravity dominates for cratering processes, referred to as the gravity regime (e.g. Housen et al. 1983). In the gravity regime, the total volume of ejecta V_{total} was obtained from the following relation (Schmidt & Holsapple 1982),

$$\frac{\rho_b V_{total}}{m_i} = 0.234 \left(\frac{3.22 g a_i}{{v_i}^2}\right)^{-0.506}, \tag{29}$$

where g is a gravitational acceleration, v_i is an impact velocity of projectile, a_i and m_i are, respectively, radius and mass of projectile, and ρ_b is a bulk density of the layer of particles. The amount of ejecta escaping from the Moon depends on the velocity distribution of ejecta and gravity. In the gravity regime, Housen et al. (1983) formulated a scaling formula of the velocity distribution of powdery ejecta. The volume of ejecta $V_t(> v_e)$ with velocity higher than a given velocity v_e was expressed as,

$$\frac{V_t(> v_e)}{R^3} = K_3 \left(\frac{v_e}{\sqrt{gR}}\right)^{-e_v}, \tag{30}$$

where R, K_3 and e_v are radius of crater, a constant, and a constant exponent, respectively. The value of R is given for a sand target from the following relation (Schmidt & Holsapple, 1982),

$$R = 0.847 \left(\frac{\rho_b}{m_i}\right)^{-1/3} \left(\frac{3.22 g a_i}{{v_i}^2}\right)^{-0.167}. \tag{31}$$

When we assume $a_i = (3m_i/4\pi\delta)^{1/3}$ where δ is a density of projectile,

$$R = 0.75 \rho_b^{-1/3} \left(\frac{\delta^{1/3} v_i^2}{g}\right)^{0.167} m_i^{0.833/3}. \tag{32}$$

Substituting Eq. (32) into Eq. (30), the total mass $M(> v_e) = \rho_b V_t(> v_e)$ of ejecta with velocity higher than v_e produced by an impact of particle with mass of m_i is derived by,

$$M(> v_e) = K_3 \times 0.75^{\gamma} \rho_b^{-e_v/6} \left(\frac{\delta^{1/3} v_i^2}{g}\right)^{0.167\gamma} g^{e_v/2} v_e^{-e_v} m_i^{\frac{0.833\gamma}{3}}, \tag{33}$$

where $\gamma = 3 + e_v/2$.

Appendix: Model of a hard surface If a size of grain at the impact site is sufficiently larger than that of an impacting particle, the impact produces a crater on the surface of individual grain. This process should be treated as a hard surface model. In this case, the effects of material strength of grain dominate for cratering processes, referred to as the strength regime (e.g. Housen et al. 1983). According to Holsapple & Schmidt (1982), in the strength-regime, a crater volume V_{total} was given by the following relation,

$$\frac{\rho_g V_{total}}{m_i} = 0.457 \left(\frac{\delta}{\rho_g}\right)^{-0.523} \left(\frac{Y}{\delta v_i^2}\right)^{-0.709}, \tag{34}$$

where Y is a target strength and ρ_g is a density of target grain. The amount of ejecta escaping from the Moon depends on the velocity distribution of ejecta, as mentioned above. In the strength regime, the volume of ejecta $V_t(> v_e)$ with velocity higher than v_e for basalt target can be expressed by Housen et al. (1983),

$$\frac{V_t(> v_e)}{R^3} = K_4 \left(v_e \sqrt{\frac{\rho_g}{Y}} \right)^{-2}, \tag{35}$$

where K_4 is a constant.

From the definition of $V_t(> v_{min}) = V_{total}$,

$$\frac{V_{total}}{R^3} = K_4 \left(v_{min} \sqrt{\frac{\rho_g}{Y}} \right)^{-2}, \tag{36}$$

where v_{min} is a minimum velocity of ejecta. From Eqs.(34), (35) and (36), we obtained the total mass $M(> v_e) = \rho_g V_t(> v_e)$ produced by an impact of particle with mass of m_i as,

$$M(> v_e) = 0.457 \left(\frac{\delta}{\rho_g} \right)^{-0.523} \left(\frac{Y}{\delta v_i^2} \right)^{-0.709} \left(\frac{v_e}{v_{min}} \right)^{-2} m_i. \tag{37}$$

References

Ahrens, T.J., O'Keefe, J.D., 1977, Impact and explosion cratering (edited by Roddy, D.J., Pepin, R.O., Merrill, R.B.), pp. 639, Pergamon Press, New York.

Alexander, M., Anz, P., Lyons, D., et al., 1984, Adv.Space Res., 4, 23.

Asada, N., 1985, J. Geophys. Res., 90, 12445.

Burns, J.A., Lamy, P.L., Soter, S., 1979, Icarus, 40, 1.

Carrier III, W.D., Olhoeft, G.R., Mendell, W., 1991, Lunar sourcebook, a user's guide to the Moon (edited by Heiken, G., Vaniman, D., French, B.M.), pp. 475, Cambridge Univ. press.

Cintala, M.J, Hörz, F., 1990, Meteoritics, 25, 27.

Cintala, M.J, Hörz, F., 1992, Meteoritics, 27, 395.

Gault, D.E., Shoemaker, E.M., Moore, H.J., 1963, NASA TND-1767.

Grün, E., Zook, H.A., Fechtig, H., Giese, R.H., 1985. Icarus, 62, 244.

Fujiwara, A., Kamimoto, G., Tsukamoto, A., 1977. Icarus, 31, 277.

Holsapple, K.A., Schmidt, R.M., 1982, J. Geophys. Res., 87, 1849.

Housen, K.R., Schmidt, R.M., Holsapple, K.A., 1983, J. Geophys. Res., 88, 2485.

Housen, K.R., 1992, LPSC, XXIII, abst., 555.

Ishimoto, H., 1996, Icarus, 122, 153.

McKay, D.S., Heiken, G., Basu, A., et al., 1991, Lunar sourcebook, a user's guide to the Moon (edited by Heiken, G., Vaniman, D., French, B.M.), pp. 285, Cambridge Univ. press.

Melosh, H.J., 1989, Impact cratering., Oxford Univ. Press, New York.

Mizutani, H., Takagi, Y., Kawakami, S., 1990, Icarus, 87, 307.

O'Keefe, J.D, Ahrens, T.J., 1982, J. Geophys. Res., 87, 6668.

Schmidt, R.M., Holsapple, K.A., 1982, Geol. Soc. Amer. Spec. Pap., 190, 93.

Yamamoto, S., Mukai, T., 1996, Physics, Chemistry, and Dynamics of Interplanetary Dust (edited by Gustafson, B.A.S., Hanner, M.S.), pp. 47, PASP Conference Series, Provo, Utah.

Yamamoto, S., Nakamura, A.M., 1997. Icarus, 128, 160.

Yen, K.Z.Y., Chaki, T.K., 1992, J. Appl. Phys., 71, 3164.

Zook, H.A., 1975, Proc. Lunar Sci. Conf. 6th, 1653.

4 Dust Production by Impacts of Interstellar Dust on Edgeworth-Kuiper Belt Objects

S.Yamamoto & T.Mukai
A&A, **329**, 785-791 (1998)

Abstract

We estimated the production rate of dust grains by the impacts of interstellar dust grains on Edgeworth-Kuiper Belt objects (EKOs). In this scenario, the impact ejecta become interplanetary dust particles with radii smaller than about 10 μm. If the EKOs have hard icy surfaces and there are $\sim 10^{13}$ of these with radii $\geq$0.1 km, the total dust production rate over the entire Edgeworth-Kuiper Belt ranges from 3.7×10^5g s^{-1} to 2.4×10^6g s^{-1}, depending on the adopted minimum ejection velocity (10 cm s^{-1} $\sim$10^3 cm s^{-1}). If the surfaces of EKOs are covered by a layer of icy particulates with radii smaller than those of the incident dust grains, then the total dust production rate is enhanced slightly to about 3.1×10^7g s^{-1}. Adopting the different collisional parameters used by Stern (1996), we find that the production rate of dust grains with radii smaller than 10μm by mutual collisions of EKOs is between 8.6×10^4g s^{-1} and 2.9×10^7g s^{-1}. Therefore dust production due to the impacts by interstellar dust on EKOs is a significant source of interplanetary dust grains, at least for those far from the sun with radii smaller than about 10 μm.

4.1 Introduction

Meteoroid detectors on board Pioneer 10 and 11 recorded a near constant rate of impact by dust grains, which have moderately eccentric orbits with random inclinations, out to a distance of 18AU (Humes 1980). Recent space probes such as Ulysses and Galileo, furthermore, detected dust grains in the ecliptic plane at heliocentric distances between 0.7 and 5.4 AU, and in an almost perpendicular-plane from ecliptic latitude $-79°$ to $+79°$ (Grün et al. 1995a,b). Although these dust grains may originate from different sources of interplanetary dust, the variation of the impact flux of meteoroids with heliocentric distance suggests the existence of dust sources in the outer Solar System.

Active comets can be major contributors to these dust grains. However, since small dust grains released from active comets are likely to have large eccentricities, most of them escape from the Solar System due to solar radiation pressure forces (Mukai 1985). Therefore it is unlikely that active comets are a major source of interplanetary dust at large heliocentric distances.

Recently, it has been suggested that significant dust production occurs in the Edgeworth-Kuiper Belt due to the mutual collisions of Edgeworth-Kuiper Belt objects (EKOs) (e.g. Backman et al. 1995; Liou et al. 1996; Stern 1996). Jewitt & Luu (1995) estimated that about 3.5×10^4 objects with diameters larger than 100km exist in the Edgeworth-Kuiper Belt. Observations by the Hubble Space Telescope suggest that there are more than 2 $\times10^8$ Halley-sized objects in the region (Cochran et al. 1995). Duncan et al. (1995) estimated that, within 50 AU, the total number of comets in the Belt is roughly 5×10^9. It has been proposed that the collisions between these objects provide a significant amount of dust grains in the Edgeworth-Kuiper Belt. Stern (1996) estimated the production rate of collisional debris, and predicted a time-averaged mass supply rate of $3\times10^{16}\sim10^{19}$g yr^{-1}, for collisional debris ranging from multi-kilometer blocks to fine dust.

The in situ measurements by the Ulysses space craft show that the stream of interstellar grains penetrates into the Solar System (Grün et al. 1993). In this paper, we propose that the impacts by such interstellar dust on EKOs produce a considerable amount of dust grains. EKOs are continuously bombarded by interstellar dust grains with high relative velocities ($\sim$ 26 km s^{-1}). Although the amount of target material excavated by the individual impacts of interstellar dust is smaller than the amount produced by collisions between large EKOs, impacts by interstellar dust grains occur more frequently. Moreover, all EKOs are bombarded by interstellar dust simultaneously, whereas mutual collisions of EKOs occur locally. As a consequence, the continuous impact by interstellar dust should provide a considerable amount of dust grains all over the Edgeworth-Kuiper Belt region.

In Sect. 4.2, we investigate dust production under two different surface conditions. In one model the surfaces are composed of hard icy material. In the other model the surfaces are covered by loose icy particulate, produced by collisional resurfacing of EKOs. In Sect. 4.3 the total dust production rate over the entire Edgeworth-Kuiper Belt is calculated by using the same size distribution of EKOs modeled by Stern (1996). Our results are compared with the production rate of collisional debris predicted by Stern (1996) in Sect. 4.3.3. A summary of our results is presented in Sect. 4.5.

4.2 Model Construction

We shall estimate the dust production rate of hypervelocity impacts on EKOs by interstellar dust. The surface condition of the target is an important parameter in the cratering process. Since the escape velocity of EKOs is small (less than about 10^4 cm s^{-1}), for hard icy surfaces the effect of material strength dominates over the effect of gravity in the cratering process. If the surface of an EKO is covered by a layer of icy particulate (Luu & Jewitt 1996), however, the effect of gravity dominates the cratering process. Therefore, we shall estimate the dust production rate separately for both a hard surface and for a surface covered by icy particulate.

4.2.1 Model for a hard surface of ice material

The first model assumes that EKOs have a hard surface of ice material. In previous works, impact experiments onto water ice targets were performed to investigate the crater volume (e.g., Lange & Ahrens 1987; Frisch 1992; Eichhorn & Grün 1993). Frisch (1992) used particles with masses 7.6×10^{-9}g to 2.5×10^{-6}g for the projectile, while Lange & Ahrens (1987) applied a particle mass of 8 g for the projectile. On the other hand, Eichhorn & Grün (1993) used smaller particles with masses between 10^{-14}g and 8×10^{-11}g as the projectiles. The data of Eichhorn & Grün (1993) is appropriate for the study of craters produced by the impacts of interstellar dust grains, which have an average mass of about 8×10^{-13}g (Grün et al. 1993). Eichhorn & Grün (1993) compared their results with those obtained by Frisch (1992) and Lange & Ahrens (1987), and gave an expression for the crater volume V_c [cm^3], as a function of the kinetic energy E_{kin} [eV] of the projectile, which holds over 10 orders of magnitude in kinetic energy:

$$V_c\rho = 2.34 \times 10^{-20} E_{kin}^{0.98} \times \rho, \tag{38}$$

$$E_{kin} = 0.5 m_i v_i^2 \tag{39}$$

where ρ [g cm^{-3}] is the density of the ice, and v_i [cm s^{-1}] and m_i [g] are the impact velocity and mean mass of interstellar dust grains respectively. We assume that the density of ice targets ρ is 1.0 g cm^{-3}, the mean particle mass of interstellar dust m_i is 8×10^{-13}g, and the impact velocity v_i is 26 km s^{-1} (Grün et al. 1993). Substituting these values into Eqs.(38)-(39), we obtain,

$$V_c\rho = 2.25 \times 10^{-8} [\mathrm{g}]. \tag{40}$$

Since the impact velocity is sufficiently high (26 km s^{-1}), the total mass of the ejecta is about four orders of magnitude higher than the mass of the impacting particle.

It should be noted that some of the excavated material may melt or vaporize. According to Melosh (1989), the ratio of the mass of melted material M_m to the mass of the projectile m_i is given by

$$M_m/m_i = 0.14 v_i^2/\epsilon_m, \tag{41}$$

where ϵ_m is the specific internal energy for melting the target material. Substituting $\epsilon_m = 2 \times 10^{10}$erg g^{-1} for an ice target (Melosh 1989) and $m_i = 8 \times 10^{-13}$g, we found $M_m = 3.8 \times 10^{-11}$g. Therefore, the mass of the melted material is about 0.2% of the total mass of excavated material. In addition, the former is always larger than the vapor mass by a factor of nearly 10 (Melosh 1989). Consequently, both the masses of the melted and vaporized material are negligibly small compared to the total mass of excavated material.

Impact ejecta with velocity smaller than the escape velocity of the target body would eventually fall back and deposit on the surface. The amount of escaping ejecta depends on the velocity distribution of excavated material and on the gravity of the target body. Unfortunately, the velocity distribution of icy ejecta has not yet been investigated in previous impact experiments onto icy targets. Therefore, the amount of ejecta escaping from the icy target bodies is estimated in the following way.

When the target is composed of hard materials, the effect of material strength dominates the cratering process; this is referred to as the strength regime (e.g., Housen et al. 1983). According to Housen et al. (1983), the volume $V_t(> v_e)$ of ejecta with velocity higher than v_e can be expressed in the strength regime by:

$$\frac{V_t(> v_e)}{R^3} = K_4 \left(v_e \sqrt{\frac{\rho}{Y}} \right)^{\frac{6\alpha}{\alpha-3}} \tag{42}$$

where R is the crater radius, Y the target strength, K_4 a constant, and α is a parameter related to energy and momentum coupling in cratering events. By presenting the physical arguments for α, Holsapple & Schmidt (1982) restricted α to the range $3/7 \le \alpha \le 3/4$. Physically, when $\alpha = 3/4$, the projectile energy is important for the crater dimensions. On the other hand, when $\alpha = 3/7$, the projectile momentum is important (Holsapple & Schmidt 1982). From the results of impact experiments, Housen et al. (1983) reported $\alpha = 3/4$ for a basalt target, and 0.51 for a sand target. The cratering process in an ice target is expected to be similar to that for a basalt target rather than that for a loose sand target. Since the value of $\alpha = 3/4$ for a basalt target seems to be the theoretical upper limit of α, we assume that the value of α for an ice target is equal to or smaller than 3/4. When the target body has a larger mass (e.g., the Moon), the amount of escaping ejecta is very sensitive to the velocity distribution of the ejecta. In that case, the value of α is a key factor. But since the majority of EKOs have low escape velocities, the amount of escaping ejecta is not so sensitive to the value of α. Therefore in the following we adopt $\alpha = 3/4$ for impacts on hard icy surfaces.

Substituting $\alpha = 3/4$ into Eq.(42), we obtained,

$$\frac{V_t(> v_e)}{R^3} = K_4 \left(v_e \sqrt{\frac{\rho}{Y}} \right)^{-2}. \tag{43}$$

From the definition of $V_t(> v_{min}) = V_c$,

$$\frac{V_c}{R^3} = K_4 \left(v_{min} \sqrt{\frac{\rho}{Y}} \right)^{-2} \tag{44}$$

where v_{min} is the minimum velocity of the ejecta. From Eqs.(43) and (44), we obtained,

$$V_t(> v_e) = V_c \left(\frac{v_e}{v_{min}} \right)^{-2}. \tag{45}$$

Substituting Eq.(40) into Eq.(45), we obtained the total mass of ejecta with velocities higher than the escape velocity v_{esc} of target body, as

$$V_t(> v_{esc})\rho = 2.25 \times 10^{-8} \left(\frac{v_{esc}}{v_{min}} \right)^{-2}. \tag{46}$$

If we assume that the EKO with $\rho = 1$ g cm^{-3} has a spherical shape with radius s [cm], v_{esc} is presented by

$$v_{esc}[\mathrm{cm\ s^{-1}}] = 7.48 \times 10^{-4} \times s. \tag{47}$$

From the observations by the Ulysses space craft, the flux of interstellar grains f is estimated to be 8×10^{-9}cm^{-2}s^{-1} (Grün et al. 1993). Using this value and Eqs.(46) & (47), we can calculate the mass flux of escaping ejecta $F_t(> v_{esc})$ produced by the impact of an interstellar dust particle,

$$\begin{aligned} F_t(> v_{esc}) &= V_t(> v_{esc})\rho f \\ &= 3.2 \times 10^{-10} \left(\frac{s}{v_{min}}\right)^{-2} [\text{ g s}^{-1}\text{cm}^{-2}]. \end{aligned} \tag{48}$$

We set minimum velocities ranging from 10 cm s^{-1} to 10^3 cm s^{-1} in Eq.(48). From impact experiments onto water ice targets, Frisch (1992) measured velocities of ice ejecta ranging from 4×10^2 cm s^{-1} to 5.7×10^4 cm s^{-1}. Due to the detection limit of the experimental setup, the real minimum velocity could be lower than 4×10^2 cm s^{-1}. Based on her laboratory measurements, Onose (1996) reported that the minimum velocity of ice ejecta was around tens of cm s^{-1}. Thus the minimum velocities ranging from 10 cm s^{-1} to 10^3 cm s^{-1} employed here seem to be reasonable for icy ejecta.

4.2.2 Model for a layer of icy particulate

The second model assumes that the surfaces of EKOs are covered by a layer of icy particulate. We note that if the size of the particulate is sufficiently larger than that of the interstellar dust grain, the impact by the latter produces a crater on the surface of an individual particulate. This process can then be treated as the hard surface case presented in Sect. 4.2.1. On the other hand, if the layer of particulate is composed of fine grains which are smaller than the interstellar dust grains, an impact crater will be produced in the layer of the particulate. This case shall be examined in the following.

Gravity dominates over material strength for cratering in a layer of particulate; this is generally referred to as the gravity regime (Housen et al. 1983). Therefore the cratering process is not sufficiently affected by the properties of the target material. Hence we assume that the cratering process in an icy particulate is similar to that of sand targets.

Housen et al. (1983) formulated the distribution of velocity in the lower velocity ($\sim$ m s^{-1}) region of powdery ejecta, based on experiments of impact cratering on sand targets. Their result is expressed as,

$$\frac{V_t(> v_e)}{R^3} = 0.32 \left(\frac{v_e}{\sqrt{gR}}\right)^{-1.22} \tag{49}$$

where g is the surface gravity and R is the carter radius. On the other hand, the velocity distribution of powdery ejecta with velocities higher than several hundred m s^{-1} has been detected recently by Yamamoto & Nakamura (1997). Their data are fitted by the same scaling formula to give the following relation:

$$\frac{V_t(> v_e)}{R^3} = 0.03 \left(\frac{v_e}{\sqrt{gR}}\right)^{-1.2} . \tag{50}$$

In this study we estimate the impact ejecta from target bodies with radii ranging from hundreds of m to hundreds of km, with corresponding escape velocities from about tens of cm s^{-1} to hundreds of m s^{-1}. The reason why $V_t(> v_e)$ derived from Eq.(49) is about one order of magnitude higher than that derived from Eq.(50) is unclear. This difference affects the total mass estimation of ejecta escaping from the target body. Therefore, we use Eq.(49) and Eq.(50) separately to obtain the upper and lower estimates of the total dust production rate from the surface of an icy particulate.

According to Schmidt & Holsapple (1982), the crater radius R in particulate targets is given by the following:

$$\Pi_r \Pi_2^{0.167} = 0.847 \quad , \tag{51}$$

$$\Pi_r = R\left(\frac{\rho}{m_i}\right)^{1/3} \quad , \quad \Pi_2 = \frac{3.22 g r}{v_i^2},$$

where r is a radius of projectile. By using Eq.(47), the surface gravity is expressed as

$$g = \sqrt{G\rho\frac{2\pi}{3}} v_{esc} = 3.74 \times 10^{-4} v_{esc} \tag{52}$$

where G is the gravitational constant. Substituting Eq.(52), $r = (3m_i/4\pi\delta)^{1/3}$, and an impactor density of $\delta = 2.5$ g cm^{-3} (Grün et al. 1985) into Eq.(51), the crater radius in the particulate target is:

$$R = 0.23 \times v_{esc}^{-0.167}. \tag{53}$$

We have assumed that the porosity of particulate was 0.5 (Yen & Chaki 1992) and the bulk density was 0.5 g cm^{-3}. Substituting Eq.(53) into Eqs.(49) and (50), the total volume of ejecta escaping from the target body is derived. The upper estimate is

$$V_t(> v_{esc}) = 1.3 \times 10^{-5} \times v_{esc}^{-1.21}, \tag{54}$$

whilst the lower estimate is

$$V_t(> v_{esc}) = 1.3 \times 10^{-6} \times v_{esc}^{-1.20}. \tag{55}$$

Substituting Eq.(47) into Eqs.(49) and (50), and using the value of f for the flux of interstellar dust grains used in Eq.(48), we are able to calculate the mass flux of escaping ejecta by the impact of an interstellar dust grain. The upper estimate is

$$F_t(> v_{esc}) = 3.2 \times 10^{-10} s^{-1.21} [\text{g s}^{-1}\text{cm}^{-2}] \tag{56}$$

whilst the lower estimate is

$$F_t(> v_{esc}) = 2.9 \times 10^{-11} s^{-1.20} [\text{g s}^{-1}\text{cm}^{-2}] \tag{57}$$

In both cases we quote the power index to 3 significant figures.

4.3 Dust production rate by interstellar dust impacts

4.3.1 From one EKO

For impacts by interstellar dust, the cross section of an EKO is assumed simply as πs^2. The hard surface model leads to the production rate of dust escaping from one target as

$$F_t(> v_{esc}) \times \pi s^2 = 3.2 \times 10^{-10} \pi v_{min}^2. \tag{58}$$

Thus the dust production rate from an object with a hard surface is independent of the target size s, if we assume that the minimum velocity of the ejecta is independent of the target size (see Fig. 13). We note, however, that for small objects (i.e. $v_{min} > v_{esc}$), v_{esc} in Eq.(46) is replaced by v_{min}. As a result, the production rate of dust escaping from a small object becomes

$$V_t(> v_{min}) \rho f \times \pi s^2 = 1.8 \times 10^{-16} \pi s^2. \tag{59}$$

In the gravity regime, the crater volume in particulate targets V_c is given by Schmidt & Holsapple (1982) as

$$\begin{aligned} \Pi_v \Pi_2^{0.506} &= 0.234, \\ \Pi_v &= \frac{V_c \rho}{m_i}, \end{aligned} \tag{60}$$

where Π_2 is defined in Eq.(51). From the definition of $V_t(> v_{min}) = V_c$ in Eq.(49), and from Eqs.(47), (14), (52) & (60), we obtained

$$\frac{v_{min}}{v_{esc}} \sim 0.52 s^{-0.58} \tag{61}$$

On the other hand, from Eqs.(50), (47), (14), (52) & (23),

$$\frac{v_{min}}{v_{esc}} \sim 0.07 s^{-0.58}. \tag{62}$$

If $s \geq 10^3$cm, $v_{min}/v_{esc} \ll 1$ in Eqs.(61) & (62). Therefore the escape velocity is always higher than v_{min}. This implies that the conditions which apply to Eq.(59) do not apply for a particulate surface.

Therefore, the production rate of dust escaping from one target body is derived from Eqs.(56) and (57) as

$$F_t(> v_{esc}) \times \pi s^2 = 3.2 \times 10^{-10} \pi s^{0.79}, \tag{63}$$

for the upper estimate, and

$$F_t(> v_{esc}) \times \pi s^2 = 2.9 \times 10^{-11} \pi s^{0.80}. \tag{64}$$

for the lower estimate.

These results demonstrate why the dust production rate in the case of icy particulate surfaces depends on the target radius s for all target bodies, in contrast with the two different s-dependence dust production rates derived for the hard surface case (see Fig. 13).

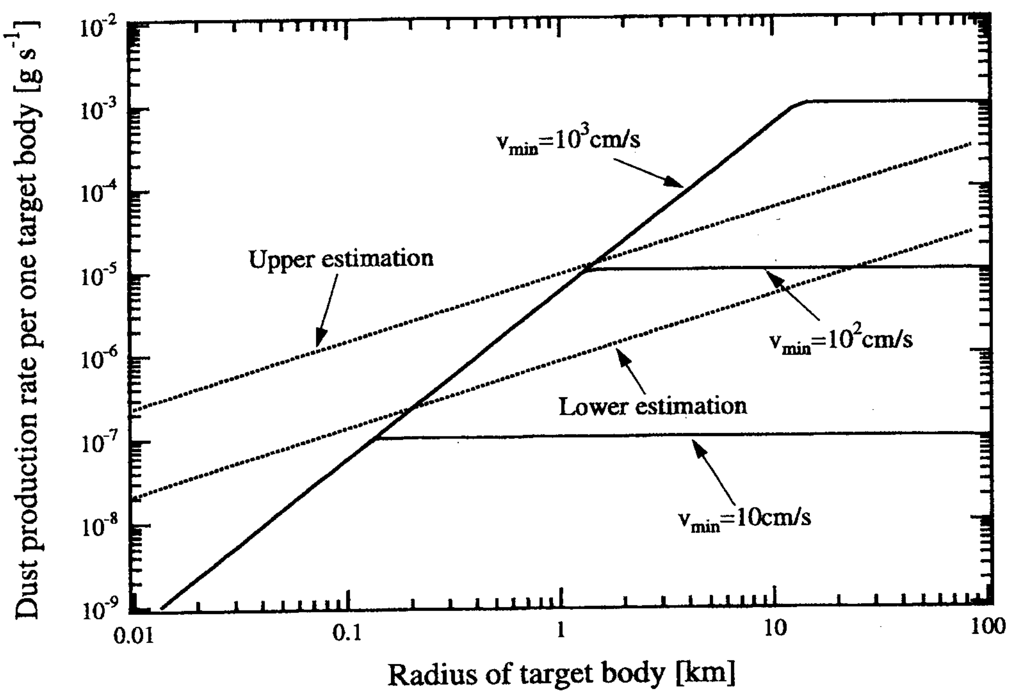

Figure 13: The production rate of dust escaping from a target body with radii ranging from 10 m to 100 km, and covered by a hard icy surface (solid line), or by ice particulate (dashed line).

4.3.2 From all EKOs

Next, we estimate the total dust production rate M_t by summing the ejecta mass from one target body, estimated in Sect. 4.3.1, over the entire Edgeworth-Kuiper Belt region. The size distribution of EKOs is a key factor. Stern (1995, 1996) investigated the rate of mutual collisions of EKOs with radii from 0.1 km to 162 km, and predicted a total production rate of collisional debris. Since it is worthwhile to compare the production rate by impacts of interstellar dust with that produced by mutual collisions of EKOs, we shall adopt the size distribution model of EKOs used by Stern (1995, 1996).

Stern's model assumes that EKOs obey a power law size distribution,

$$n(s)ds = N_0 s^{\beta} ds \tag{65}$$

where $n(s)ds$ is the number density of EKOs having radii between s and $s+ds$, and N_0 is a constant. Using the two models of EKO size distribution used in Stern (1995, 1996), we estimate the total dust production rate due to impacts by interstellar dust over all EKOs.

We note that the minimum size limit of EKOs is an important parameter in estimating the total dust production rates, both for dust production by EKOs mutual collisions and for that by impacts of interstellar dust on EKOs. Observations by the Hubble Space Telescope found 29 objects with radii ranging from 5 to 10 km in the Edgeworth-Kuiper Belt region (Cochran et al. 1995). Much smaller objects that are too faint to be detected, however, may exist in the Edgeworth-Kuiper Belt. Recent works on collisional evolution among EKOs assume the minimum radius of an EKO to be ~ 0.1 km (Stern 1995, 1996; Davis & Farinella 1997). In order to make a comparison with the dust production rate by mutual collisions of EKOs predicted by Stern (1996), we also assume that the minimum radius of the object is 0.1 km. In addition, we adopt a maximum radius of 162 km, which is also the same value used by Stern (1996).

Nominal model According to Jewitt & Luu (1995), there are about 3.5×10^4 QB_1 sized objects (≥ 50 km in radius) in the Edgeworth-Kuiper Belt region. As a simple power-law with $\beta = -4.21$, the first model connects this population with about 10^{10} comets which Stern (1995, 1996) defined as bodies with radii between 1 and 6 km.

Note that Stern (1995, 1996) uses a power law with $\beta = -11/3$, and he defines the 3.5×10^4 QB_1 sized objects as bodies with radii ≥ 100 km, whereas Jewitt & Luu's (1995) estimate applies for radii ≥ 50 km. In this work we define the QB_1 sized objects as bodies with radii ≥ 50 km.

The normalization constant N_0 is calculated from the statistics of the 3.5×10^4 QB_1 sized objects by

$$\int_{5\times10^6}^{\infty} N_0 s^{-4.21} ds = 35000. \tag{66}$$

From Eq.(66), we obtained $N_0 = 3.6 \times 10^{26}$.

For the hard surface model, Eqs.(58) and (59) lead to

$$\begin{aligned} M_t &= \int_{10^4}^{\frac{v_{min}}{7.48\times10^{-4}}} 1.8 \times 10^{-16} \pi s^2 N_0 s^{-4.21} ds \\ &+ \int_{\frac{v_{min}}{7.48\times10^{-4}}}^{1.62\times10^7} 3.2 \times 10^{-10} \pi v_{min}^2 N_0 s^{-4.21} ds. \end{aligned} \tag{67}$$

Substituting v_{min}= 10 and 10^3 cm s^{-1} into Eq.(30), we find that the total dust production rate M_t ranges from 1.4×10^6 g s^{-1} to 2.4×10^6 g s^{-1}.

On the other hand, from Eqs.(63) and (64), the total production rate of dust from a surface of icy particulate is

$$\begin{aligned} M_t &= \int_{10^4}^{1.62\times10^7} 3.2 \times 10^{-10} \pi s^{0.79} N_0 s^{-4.21} ds \\ &= 3.1 \times 10^7 \quad [\text{g s}^{-1}] \text{ for the upper estimate,} \end{aligned} \tag{68}$$

and

$$\begin{aligned} M_t &= \int_{10^4}^{1.62\times10^7} 2.9 \times 10^{-11} \pi s^{0.80} N_0 s^{-4.21} ds \\ &= 3.1 \times 10^6 \quad [\text{g s}^{-1}] \text{ for the lower estimate.} \end{aligned} \tag{69}$$

Constant mass model The second model assumes a constant EKO mass distribution in every logarithmic size bin, and gives $\beta = -4$ (Stern 1995, 1996). Again, the normalization constant N_0 is calculated from the statistics of the 3.5×10^4 QB_1 sized objects (Jewitt & Luu 1995),

$$\int_{5\times10^6}^{\infty} N_0 s^{-4} ds = 35000 \tag{70}$$

	Nominal model for the size distribution of EKOs	Constant mass model for the size distribution of EKOs
hard surface	$1.4 \times 10^6 \sim 2.4 \times 10^6$ [g s^{-1}] ($v_{min} = 10 \sim 10^3$ cm s^{-1})	$3.7 \times 10^5 \sim 7.3 \times 10^5$ [g s^{-1}] ($v_{min} = 10 \sim 10^3$ cm s^{-1})
particulate surface	$3.1 \times 10^6 \sim 3.1 \times 10^7$ [g s^{-1}] (depend on the velocity distribution of powdery ejecta)	$8.5 \times 10^5 \sim 8.5 \times 10^6$ [g s^{-1}] (depend on the velocity distribution of powdery ejecta)

Table 7: Total dust production rate M_t due to impacts by interstellar dust over the entire Edgeworth-Kuiper Belt.

giving $N_0 = 1.3 \times 10^{25}$. This model produces 4.3×10^9 comets with radii between 1 km and 6 km, and this result is consistent with the estimation by Duncan et al. (1995) that the total number of comets is roughly 5×10^9.

Following similar arguments as those for the nominal case described above, the total dust production rate for the hard surface model is,

$$\begin{aligned} M_t &= \int_{10^4}^{\frac{v_{min}}{7.48\times10^{-4}}} 1.8 \times 10^{-16} \pi s^2 N_0 s^{-4} ds \\ &+ \int_{\frac{v_{min}}{7.48\times10^{-4}}}^{1.62\times10^7} 3.2 \times 10^{-10} \pi v_{min}^2 N_0 s^{-4} ds. \end{aligned} \tag{71}$$

Substituting v_{min}= 10 and 10^3 cm s^{-1} into Eq.(34), we find that the total dust production rate is $M_t = 3.7 \times 10^5$ g s^{-1} and 7.3×10^5 g s^{-1} respectively.

For the case of icy particulate surface model, we derive

$$\begin{aligned} M_t &= \int_{10^4}^{1.62\times10^7} 3.2 \times 10^{-10} \pi s^{0.79} N_0 s^{-4} ds \\ &= 8.5 \times 10^6 \quad \text{[g s}^{-1}\text{] for the upper estimate,} \end{aligned} \tag{72}$$

and

$$\begin{aligned} M_t &= \int_{10^4}^{1.62\times10^7} 2.9 \times 10^{-11} \pi s^{0.80} N_0 s^{-4} ds \\ &= 8.5 \times 10^5 \quad \text{[g s}^{-1}\text{] for the lower estimate.} \end{aligned} \tag{73}$$

4.3.3 Discussion

The total dust production rate M_t due to impacts by interstellar dust over the entire Edgeworth-Kuiper Belt is summarized in Table 7 for the cases considered.

The production rate of dust escaping from a larger object ($\geq$ 100 km) is about four orders of magnitude higher than that from a smaller object ($\sim$ 0.1 km) (see Fig. 13). On the other hand, the smaller objects are at least 7 orders of magnitude more numerous than the larger target bodies from Eq.(65). Therefore, the major part of the dust produced in the Edgeworth-Kuiper Belt region originates from the smaller objects. In other words, the total dust production rate due to impacts by interstellar dust depends strongly on the number of small objects ($\leq$ 1km) in the Edgeworth-Kuiper Belt.

The minimum radius of an EKO was set at 0.1 km for comparison with the dust production rate by mutual collisions of EKOs (Stern 1996). However, much smaller objects that are too faint to be detected may exist in this region. Since most of the dust produced by impacts of interstellar dust comes from small objects, a reduction in the minimum radius of an EKO from 0.1 km to 10 or 1 m would lead to dust production rates higher than those estimated in this paper.

The sensitivity of our results to the value of α in Eq.(42) is tested. By using $\alpha = 3/7$, corresponding to the theoretical lower limit (Holsapple & Schmidt 1982), we re-derived the total dust production rate over all EKOs for the hard surface model. We find that the total dust production rates are 1.7×10^6g s^{-1} $\sim$ 2.4×10^6g s^{-1} for the nominal EKO's size distribution model, and 4.6×10^5g s^{-1} $\sim$ 7.3×10^5g s^{-1} for the constant mass model. These results are very similar to those derived for $\alpha = 3/4$. Therefore we conclude that the assumption of $\alpha = 3/4$ for the ice targets does not have a significant influence on the total dust production rate, as long as $3/7 \leq \alpha \leq 3/4$.

Next, we estimate the optical depth of a dust cloud consisting of grains with the properties estimated in Table 7. The optical depth τ is defined by

$$\tau = \frac{M_t T_l}{4\pi a^3 \rho/3} \frac{\sigma l}{V_{belt}} \tag{74}$$

where T_l is the lifetime of the grains, σ its cross section for extinction, l the width of the Edgeworth-Kuiper Belt, and V_{belt} the volume of the Edgeworth-Kuiper Belt region. For simplicity, we assume that all the grains have a radius $a = 10^{-4}$cm and hence $\sigma = \pi a^2 = 3.1 \times 10^{-8}$cm^2. Poynting-Robertson drag dominates the orbital evolution of grains with $a = 10^{-4}$cm in the Edgeworth-Kuiper Belt region (Liou et al. 1996) . Therefore, we take the timescale of the Poynting-Robertson drag T_{pr} as T_l, i.e.

$$T_{pr} = 7.0 \times 10^6 a \rho l_0^2 [\text{years}] \tag{75}$$

where a and ρ are in CGS-units and l_0 is in AU (Wyatt & Whipple 1950). We further assume that the dust grains are in circular orbits at $l_0 = 50$AU. Substituting $a = 10^{-4}$cm, $\rho = 1$g cm^{-3} and $l_0 = 50$AU into Eq. (75), we obtain $T_{pr} = 5.5 \times 10^{13}$s. Assuming the Edgeworth-Kuiper Belt region is a band with thickness of 16deg around the ecliptic, with a width $l = 20$AU (Jewitt & Luu 1995), we calculated $V_{belt} = 1.9 \times 10^{44}$cm^3. Substituting these values into Eq. (74), τ is calculated to be 2.4×10^{-7} for $M_t = 3.7 \times 10^5$ g s^{-1}, and 2.0×10^{-5} for $M_t = 3.1 \times 10^7$g s^{-1}. Stern (1996) predicted the optical depth of debris produced by mutual collisions to be between 3×10^{-7} and 5×10^{-6}. Although our estimates are slightly higher than those predicted by Stern (1996), more detailed analysis of the optical properties of thin dust clouds is required to predict their detectability from the Earth.

4.4 Comparison with the dust production rate by mutual collisions of EKOs

Stern (1996) predicted a time-averaged production rate of debris between 9.5×10^8 and 3.2×10^{11}g s^{-1} due to the mutual collisions of EKOs, depending on the parameters used in his collisional simulations. In this section, we shall estimate the production rate of dust grains due to mutual collisions of EKOs, based on the prediction by Stern (1996), in the equivalent mass range used in our estimation.

From laboratory measurements of impact ejection, Gault et al.(1963) showed that the mass of the largest fragment is about 10% of the total ejected mass M_{te} for M_{te} ranging from 10^{-2}g to 10^2g. We extrapolated this relation to the crater produced by the impact of an interstellar dust grain. Namely, the impact of an interstellar dust grain excavates a small amount of target material and produces only ejecta with small sizes. For hard icy surfaces, we obtained a crater mass $V_c\rho = 2.25 \times 10^{-8}$g from Eq.(3). Such a crater mass suggests that the mass of the largest fragment is about 2.25×10^{-9}g, corresponding to a spherical dust grain with radius $a_m = 8\mu m$. Therefore we assume that the maximum radius of dust grains produced by impacts of interstellar dust is $10\mu m$. As noted before, in the case of a particulate surface, the radius of the ejecta is smaller than that of the incident interstellar dust grains, i.e. $a_m \leq 1\mu m$.

On the other hand, the size of the collisional debris predicted by Stern (1996) ranges from multi-kilometer blocks to fine dust. In order to compare our results with his, it is necessary to estimate the fraction of dust grains with radii smaller than $10\mu m$ amongst the debris produced by mutual EKO collisions, as predicted by Stern (1996).

The size distribution of collisional debris was assumed by Stern (1996) to be $\sim a^{-3.5}$ in the range of radius a from 0.1 μm to 1 km. In this case, the total mass production rate of collisional debris is given by

$$\int_{10^{-5}}^{10^5} N_1 a^{-3.5} \frac{4\pi a^3 \rho}{3} da = M_{st}, \tag{76}$$

where M_{st} is $9.5 \times 10^8 \sim 3.2 \times 10^{11}$ g s^{-1} in Stern (1996). We found that the constant N_1 is $3.6 \times 10^5 \sim 1.2 \times 10^8$. Using this result, the production rate M_s of dust grains with radii between 0.1 μm and 10 μm can be given by

$$M_s = N_1 \times \int_{10^{-5}}^{10^{-3}} a^{-3.5} \frac{4\pi a^3 \rho}{3} da. \tag{77}$$

The value of M_s ranges from 8.6×10^4 g s^{-1} to 2.9×10^7 g s^{-1}, and is of about the same magnitude as that by impacts of interstellar dust given in Table 7.

We test the sensitivity of our result to the choice of a_m. Application of a_m=$1\mu m$ decreases the range of M_s in Eq.(77) to the range 2.1×10^4 g s^{-1} $\sim 6.9 \times 10^6$ g s^{-1}, about 24% that for a_m=$10\mu m$. These production rates are still of the same order of magnitude as those we derived earlier. Furthermore, we tested the sensitivity of the results to the minimum dust radius of $0.1\mu m$, and found that the minimum radius does not have a significant influence on the production rate M_s.

We note that the mutual collisions of debris made by the collisions between EKOs may play a significant role in the production of small dust grains. Since this scenario is rather complex and its examination is beyond the scope of this work, it will be studied at a later date.

4.5 Summary

We estimated the dust production rate by impacts of interstellar dust grains on EKOs. If EKOs have hard icy surfaces, and there are 10^{13} of these with radius $\geq$ 0.1km, we find that the total dust production rate over the entire Edgeworth-Kuiper Belt is between 3.7×10^5g s^{-1} and 2.4×10^6g s^{-1}, depending on the adopted minimum ejection velocity of 10 cm s^{-1} $\sim 10^3$ cm s^{-1}, and on the size distribution of the EKOs. On the other hand, if the surfaces of EKOs are covered by a layer of icy particulate, the total dust production rate is 8.5×10^5g s^{-1} $\sim 3.1 \times 10^7$g s^{-1}. These results suggest that, in addition to mutual collisions of EKOs, impacts by interstellar dust are a significant source of interplanetary dust grains with radii less than about 10 μm, and which exist at large distances from the sun.

After leaving the Edgeworth-Kuiper Belt, the orbits of the dust grains evolve under the complex influences of the gravitational forces of the Sun and the giant planets, as well as solar radiation pressure and Poynting-Robertson drag forces. The mutual collisions of debris particles and the collisions by interstellar dust grains may also play important roles in the evolution of dust grains. Liou et al. (1996) showed that a grain with diameter larger than about $9\mu m$ is destroyed by the mutual collisions of debris and by the impact of interstellar dust before reaching the inner Solar System, whereas smaller grains can evolve towards the inner Solar System under Poynting-Robertson drag forces. The results of Liou et al. (1996) show that about 80% of the smaller grains produced in the Edgeworth-Kuiper Belt are ejected from the Solar System by the giant planets, while 20% of the grains enter the inner Solar System under the Poynting-Robertson drag forces. The maximum radius of the grains produced by the impact of interstellar dust is about $10\mu m$ as mentioned above. Thus, a fraction of the dust grains produced by the impact of interstellar dust on EKOs may contribute to the population of the interplanetary dust inside the orbit of Jupiter. However, the sublimation of icy particles should be taken into account when estimating the lifetime of the grains at such distances (Mukai 1986). Further investigations are required to understand the contribution of these grains to the interplanetary dust in the inner Solar System.

acknowledgments We are grateful to Eberhard Grün for giving valuable comments and suggestions.

References

Backman, D.E., Dasgupta, A., Stencel, R.E., 1995, ApJ, 450, L35.

Cochran, A.L., Levison, H.F., Stern, S.A., Duncan, M.J., 1995, ApJ, 455, 342.

Davis, D.R., Farinella, P., 1997, Icarus, 125, 50.

Duncan, M.J., Levison, H.F., Budd, S.M., 1995, AJ, 110, 3073.

Eichhorn, K., Grün, E., 1993, Planet. Space. Sci., 41, 429.

Frisch, W., 1992, Hypervelocity Impacts in Space (edited by McDonnell J.A.M.), pp. 7, Unit for Space Sciences, University of Kent (Canterbury).

Gault, D.E., Shoemaker, E.M., Moore, H.J., 1963, NASA Tech. Note D-1767.

Grün, E., Zook, H.A., Fechtig, H., Giese, R.H., 1985, Icarus, 62, 244.

Grün, E., Zook, H.A., Baguhl, M., et al., 1993, Nat., 362, 428.

Grün, E., Baguhl, M., Divine, N., et al., 1995a, Planet. Space Sci., 43, 953.

Grün, E., Baguhl, M., Divine, N., et al., 1995b, Planet. Space Sci., 43, 971.

Holsapple, K.A., Schmidt, R.M., 1982, J. Geophys. Res., 87, 1849.

Housen, K.R., Schmidt, R.M., Holsapple, K.A., 1983, J. Geophys. Res., 88, 2485.

Humes, D.H., 1980, J. Geophys. Res., 85, 5841.

Jewitt, D.C., Luu, J.X., 1995, AJ., 109, 1867.

Lange, M.A., Ahrens, T.J., 1987, Icarus, 69, 506.

Liou, J.-C., Zook, H.A., Dermott, S.F., 1996, Icarus, 124, 429.

Luu, J.X., Jewitt, D.C., 1996, AJ, 112, 2310.

Melosh, H.J., 1989, Impact cratering, Oxford Univ. Press, New York.

Mukai, T., 1985, A&A 153, 213.

Mukai, T., 1986, A&A 164, 397.

Onose, M., 1996, Master thesis, Hokkaido Univ., [in Japanese].

Schmidt, R.M., Holsapple, K.A., 1982, Geol. Soc. Amer. Spec. Pap., 190, 93.

Stern, S.A., 1995, AJ, 110, 856.

Stern, S.A., 1996, A&A, 310, 999.

Wyatt, S.P., Whipple F.L., 1950, ApJ, 111, 134.

Yamamoto, S., Nakamura A.M., 1997, Icarus, in press.

Yen, K.Z.Y., Chaki, T.K., 1992, J. Appl. Phys., 71, 3164.

5 Sources of Interplanetary Dust beyond Neptune

S.Yamamoto & T.Mukai

Proc. of the 30th ISAS Lunar & Planetary Symposium., 134-137 (1997)

Abstract

Taking into account the gravitational force of the Sun, the solar radiation pressure, the Poynting-Robertson effect, as well as the ejection velocity of dust grain, we investigate the orbital evolution of dust grains, consisting of water-ice, released from the Edgeworth-Kuiper Belt objects (EKOs). All dust grains with radii greater than 1μm ejected from EKOs can stay in the Solar System against the solar radiation pressure, when the parent EKOs have eccentricities less than 0.3. On the other hand, a part of submicron-sized dust grains ejected from EKOs escape from the Solar System due to the solar radiation pressure. At the Jupiter crossing orbit, the major part of survival EKO dust grains have already circular orbits because of the Poynting-Robertson effect. Consequently, we can predict that when the grains, larger than 1μm, on the nearly circular orbits would be detected beyond Jupiter, their origin is the EKOs.

5.1 Introduction

The *in situ* measurements of dust grains beyond the Jupiter orbit suggest the existence of dust sources in the outer Solar System (Humes 1980; Grün et al. 1995a, b). Recently, it has been proposed that the dust particles produced in the Edgeworth-Kuiper Belt objects (EKOs) may contribute significantly to the interplanetary dust population (e.g. Liou et al. 1996; Stern 1996; Yamamoto & Mukai 1997). Stern (1996) estimated the collisional probability between EKOs, and predicted the mass production rate of debris due to mutual collisions between EKOs. Yamamoto & Mukai (1997) suggested that, in addition to mutual collisions of EKOs, impacts of interstellar dust on EKOs are a significant mechanism to produce the interplanetary dust grains with radii less than about 10 μm, and which exist at large distance from the Sun.

However, the existence of these dust grains coming from EKOs has not been directly confirmed by observations of zodiacal light/emission and *in situ* measurements. In order to predict the detectability of such dust grains by the observation and/or *in situ* measurements, it needs detailed analysis of spatial distribution of the dust grains released from EKOs. After leaving EKOs, the orbital elements of dust grains are immediately changed due to their ejection velocity and solar radiation pressure on them. Furthermore, the dust grains reduce gradually their perihelion distances and eccentricities under the Poynting-Robertson effect. To investigate the orbital evolution of the dust grains released from EKOs, therefore, we have to take into account the solar radiation pressure, the Poynting-Robertson effects, and the effect of ejection velocity as well as the gravitational force of the Sun. As a result of orbital evolution, we estimate the orbital properties of these dust grains at the Jupiter crossing orbit.

5.2 Orbital elements of ejected dust grains from EKOs

5.2.1 Radiation pressure

For the dust grain leaving from EKO, the solar radiation pressure immediately changes the orbital elements of dust grain (Burns et al. 1979). According to Mukai (1985), new orbital elements of the dust grain released from parent body with an eccentricity e_p and a perihelion distance q_p are given by:

$$e^2 = (1-\beta)^{-2}(e_p^2 - 2\beta + \beta^2 + 2\beta q_p(1+e_p)/r_p), \tag{78}$$
$$q = q_p(1+e_p)(1+e)^{-1}(1-\beta)^{-1}, \tag{79}$$

where the ejection velocity of the grain is assumed to be negligibly small. The e and q are, respectively, an eccentricity and a perihelion distance attained by the released dust grain. The r_p is a distance between the Sun and the parent EKO, where the grain left from the parent. The β denotes a ratio of solar radiation pressure to solar gravity on the grain. We assume for EKOs, $0 \leq e_p \leq 0.3$ and, 20 AU $\leq q_p \leq$ 50 AU

(Jewitt et al. 1996). From Eq.(78) and Eq.(79), new orbital elements of dust grains released from EKOs are estimated (Fig. 14). The orbital elements of dust grains with small value of β (~ 0.01) are similar to those

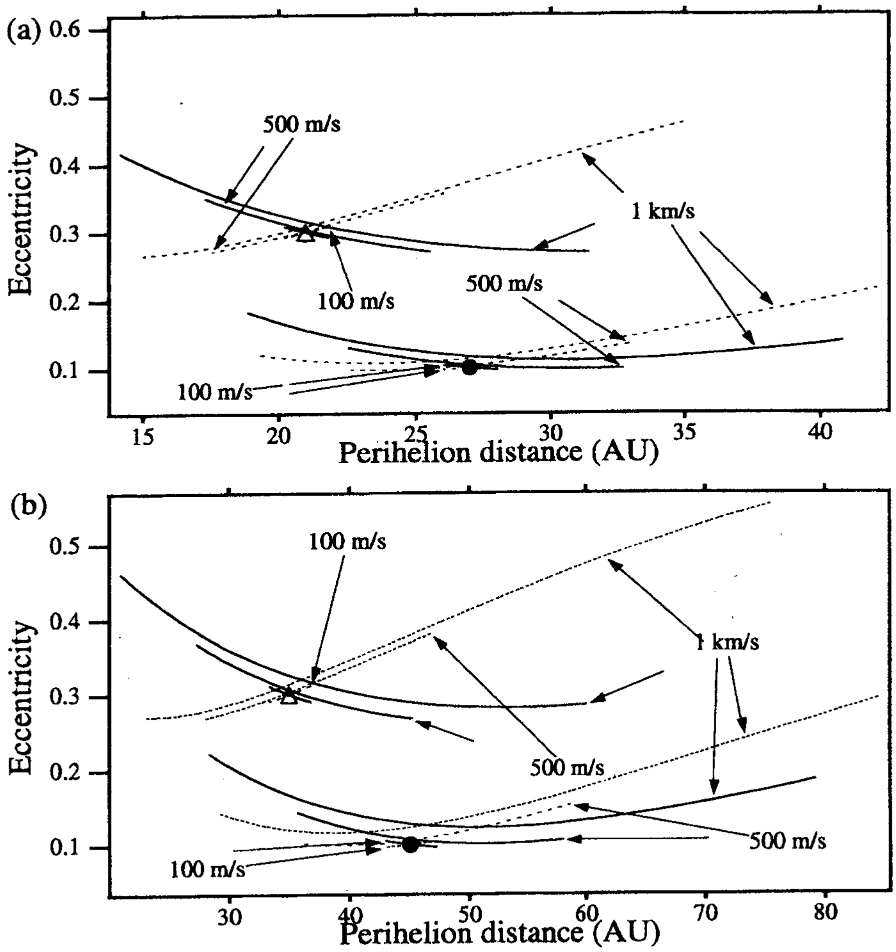

Figure 14: The distribution of the resulting eccentricity e and perihelion distance q of the dust grains affected by solar radiation force after ejection from EKOs with (a) $e_p = 0.1$ and (b) $e_p = 0.3$. The filled circle and open triangle indicate the initial positions of parent EKOs with semimajor axes of 30 AU and 50 AU, respectively. The number in each curve indicates the value of β, a ratio of radiation pressure to gravity on the grain.

of parent EKOs. The mean eccentricity of dust grain increases with increasing the value of β. When the β becomes larger than about 0.4, some dust grains attain hyperbolic orbits, *i.e.* $e > 1$ (Fig. 14), depending on the solar distance r_p of the ejection point in Eq.(78). These dust grains cannot stay in the Solar System. On the other hand, all dust grains with $\beta \leq 0.3$ can stay in the Solar System, as long as parent EKOs having $e_p \leq 0.3$.

The value of β depends on the grain radius and on the optical constants of grain material. We assume for simplicity that the EKO dust grain is a spherical water ice. The conversion from a certain value of β to a real radius of the grain is based on the Mie calculations for the optical constants of water ice (Mukai 1990) (see Fig. 15). From Fig. 15, we estimate that the β values of 0.3, 0.4 and 0.5 correspond to about 1.0, 0.7, and 0.5 μm, respectively, when the grain radius $> 0.1\mu$m. Consequently, we conclude that all dust grains with radii greater than 1μm can stay in the Solar System, while the submicron-sized dust grains partially escape from the Solar System due to the solar radiation pressure.

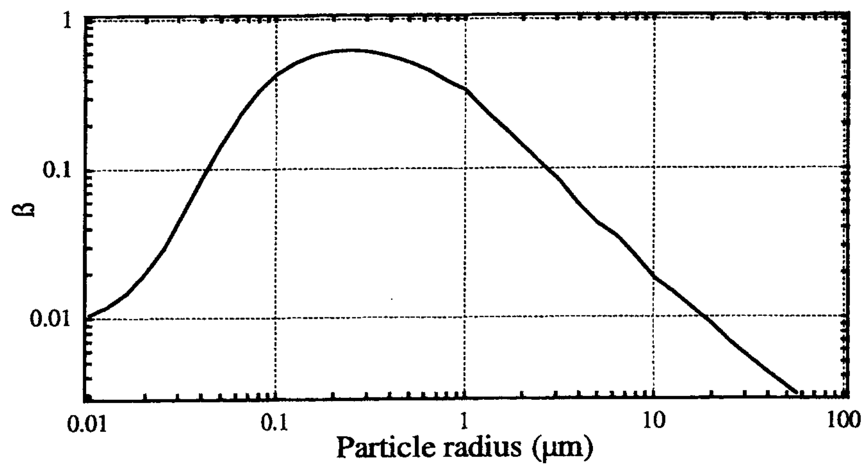

Figure 15: The value of β as a function of particle radius for a spherical water ice grain.

5.2.2 Effect of ejection velocity of dust grain

The dust grain with low ejection velocity has the orbital elements similar to that of the parent EKO. On the other hand, when the ejection velocity is sufficient large, the grain attains new orbital elements, which are different from those of parent EKO. In this case, new orbital elements of dust grain with ejection velocity $\vec{v_e}$ from the parent EKO with velocity $\vec{v_p}$ at a solar distance r_p are as follows:

$$e^2 = 1 - \left(\frac{H + \vec{r_p} \times \vec{v_e}}{GM_\odot}\right)^2 \left\{1/a_p - (v_e^2 + 2\vec{v_p} \cdot \vec{v_e})/GM_\odot\right\}, \quad (80)$$

$$q = \frac{1-e}{1/a_p - (v_e^2 + 2\vec{v_p} \cdot \vec{v_e})/GM_\odot}, \quad (81)$$

where the radiation pressure on the released grain is assumed to be negligibly small. $H = [a_p GM_\odot(1-e_p^2)]^{1/2}$ is the angular momentum per unit mass, and G and $M_\odot$ are, respectively, the gravitational constant and the solar mass. The highest velocity of ejected grain from an icy target measured in the laboratory impact experiments is less than about 1 km s^{-1} (e.g. Frisch 1992; Arakawa & Higa 1996). The dust grain with velocity lower than the escape velocity of parent body would fall back on the surface. A large fraction of EKOs have escape velocities less than about 100 m s^{-1}. Thus, we investigate dust grains with v_e=100, 500, and 1000 m s^{-1}. For simplicity, we investigate only the case of dust grain ejected at a perihelion and an aphelion of orbit of parent EKO. From Eq.(80) and Eq.(81), new orbital elements of dust grains ejected from EKOs were estimated (Fig. 16).

All ejected dust grains have $e \leq 0.6$ in Fig. 16. The resulting eccentricity e of grain orbit caused by the ejection velocity is $e < 1$. In summary, the ejection velocity has no significant influence on the survival probability of dust grains ejected from EKOs, at least, in the range of ejection velocity of interest.

5.3 Orbital distribution of dust grains at the Jupiter crossing orbit

Roughly speaking, the perihelion distance q of dust grain after leaving from EKOs ranges from 15 AU to 80 AU (see Figs. 14 and 16). These dust grains move towards to the Sun under the Poynting-Robertson effect with decreasing the eccentricity and perihelion distance, simultaneously. The grain with an initial position of e_0 and q_0 moves, under the Poynting-Robertson effect, along the trajectory in the phase space

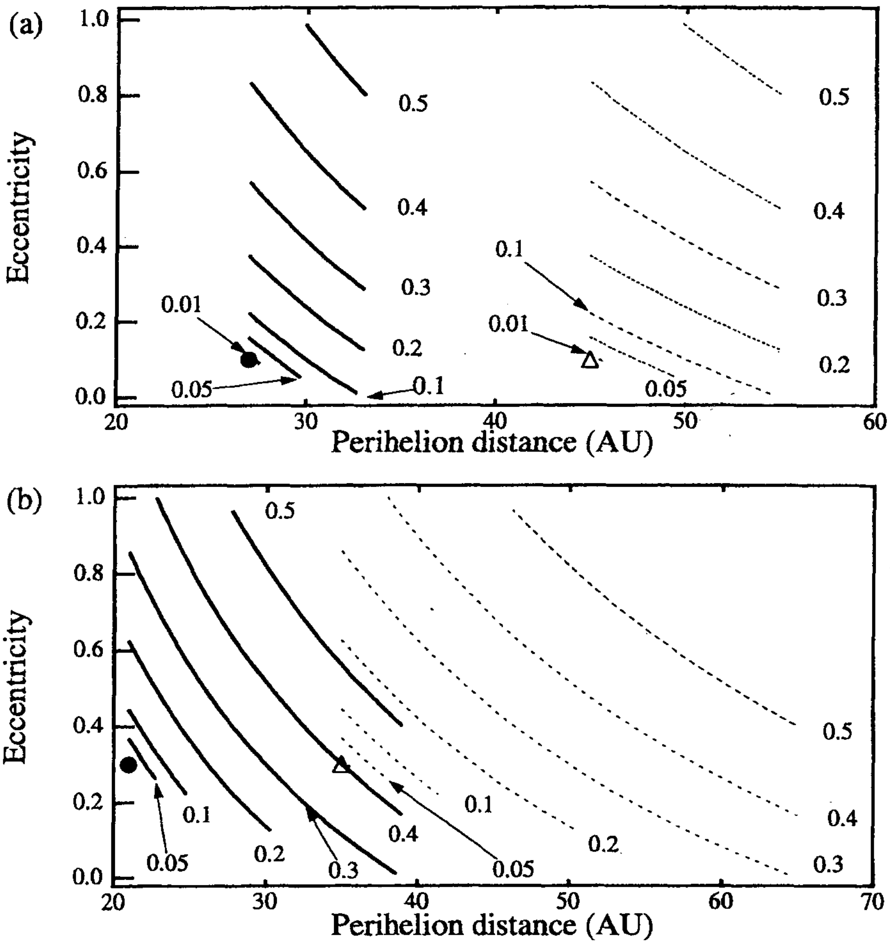

Figure 16: (a) The orbital element distribution of dust grains ejected from EKOs with semimajor axis a_p= 30 AU, taking into account the effect of ejection velocities of 100, 500, and 1000 m s^{-1}. The solid curve indicates the grain ejected at the perihelion of parent EKO orbit, and the dotted curve indicates that at the aphelion. The filled circle and open triangle correspond to the initial position in the phase space of parent EKOs with $e_p = 0.1$ and 0.3, respectively. (b) The same as (a), but a_p= 50 AU.

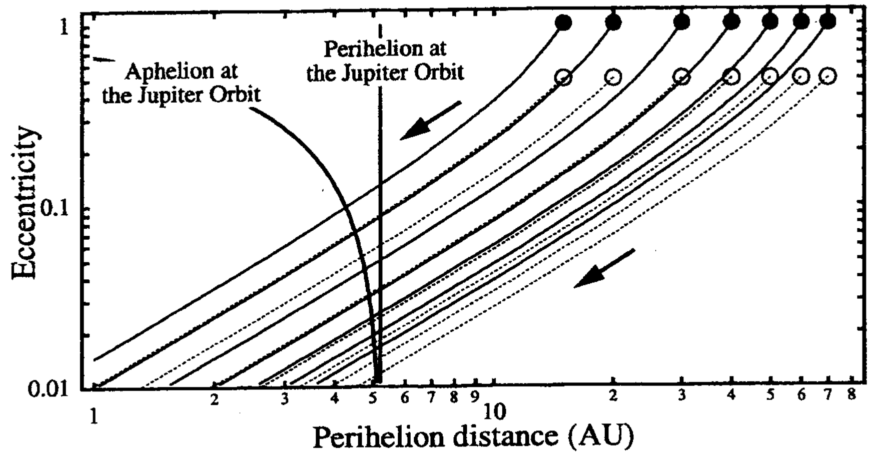

Figure 17: Trajectory of grains in the phase space due to the Poynting-Robertson drag forces (solid and dotted curves). The filled circles correspond to the initial position of dust grains with eccentricity $e_0 = 1$ and 15AU$\leq$ perihelion distance $q_0 \leq$ 70AU, and the open circles for those with $e_0 = 0.5$ and 15AU$\leq q_0 \leq$ 70AU.

(e, q) defined by,

$$\frac{q(1+e)}{e^{4/5}} = \frac{q_0(1+e_0)}{e_0^{4/5}} = \text{constant}, \tag{82}$$

(e.g., Wyatt & Whipple 1950). Using Eq.(82), we can predict the orbital elements of dust grains released from EKOs at the Jupiter crossing orbit (see Fig. 17). We have found that the resulting eccentricities of dust grains become sufficiently small at the Jupiter crossing orbit. Even for the dust grain with $e_0 \sim 1$ at $q_p = 15$ AU, its eccentricity at the Jupiter orbit becomes $e < 0.1$. This means that most of the dust grains ejected from EKOs have already attained the nearly circular orbit at the Jupiter crossing orbit.

5.4 Summary and discussion

If most of EKOs have eccentricities ≤ 0.3 (Jewitt et al. 1996), almost all dust grains with radii greater than 1μm, produced from EKOs, can stay after leaving the parent body in the Solar System against the solar radiation forces on them and the relative ejection velocity to parent EKOs. On the other hand, a part of submicron-sized dust grains escape from the Solar System due to mainly the solar radiation pressure. We have found that the effect of ejection velocity on the survival probability of dust grains ejected from EKOs is negligible.

While the mutual collisions between EKOs produce collisional debris ranging from multi-kilometer blocks to fine dust (Stern 1996), the interstellar dust impacts on EKOs provide only smaller grains ($\leq 10\mu$m) (Yamamoto & Mukai 1997). The ice grains with radii smaller than 10 μm have large values of β as shown in Fig. 15. Thus, a large fraction of dust grains produced by the interstellar dust impacts have large eccentricity after ejection due to the solar radiation pressure. On the other hand, the mutual collisions between EKOs provide both the smaller dust grains with large eccentricity and larger dust grains with eccentricities similar to those of parent EKOs.

However, since the Poynting-Robertson effect decreases the eccentricities of the grain orbits, the most of dust grains produced in the Edgeworth-Kuiper Belt region become $e < 0.1$ at the Jupiter crossing orbit. Consequently, it is difficult to distinguish between the dust grains due to mutual collisions of EKOs and dust grains due to interstellar dust impacts on EKOs from the analysis of orbital elements of dust measured by such as Ulysses and Galileo at the Jupiter crossing orbit alone.

It should be noted that the gravitational forces of outer giant planets beyond the Jupiter could increase the eccentricity of dust grain passing through near the planet, as noted by Liou et al.(1996). Since this mechanism is rather complex, it will be examined in our future studies.

References

Arakawa, M., Higa, M., 1996, Planet. Space Sci., 44, 901.

Burns, J,A., Lamy, P.L., Soter, S., 1979, Icarus, 40, 1.

Frish.,W., 1992, Hypervelocity Impacts in Space (edited by McDonnell J.A.M.), pp. 7, Unit for Space Sciences, University of Kent (Canterbury).

Grün, E., Baguhl, M., Divine, N., et al., 1995a, Planet. Space Sci., 43, 953.

Grün, E., Baguhl, M., Divine, N., et al., 1995b, Planet. Space Sci., 43, 971.

Humes, D.H., 1980, J. Geophys. Res., 85, 5841.

Jewitt, D., Luu, J., Chen, J., 1996, AJ, 112, 1225.

Liou, J.-C., Zook, H.A., Dermott, S.F., 1996, Icarus, 124, 429.

Mukai, T., 1985, A&A, 153, 213.

Mukai, T., 1990, Evolution of Interstellar dust and related topics (edited by Bonetti, A., Greenberg, J.M., Aiello, S), pp. 397, Elsevier Science.

Stern, S.A., 1996, A&A, 310, 999.

Wyatt, S.P., Whipple, F.L., 1950, ApJ, 111, 134.

Yamamoto, S., Mukai, T., 1998, A&A, 329, 785.

6 Thermal Radiation from Dust Grains in Edgeworth-Kuiper Belt

S.Yamamoto & T.Mukai

Earth, Planets, Space, **50**, 531-537 (1998)

Abstract

We calculate the temperature of dust grains produced in Edgeworth-Kuiper Belt (EKB) based on the grain model for water-ice and silicate mixtures. The dust grains with radii ranging from 0.1 μm to 1 mm have low temperatures of about 20K to 50K in EKB, depending on their size, solar distance, and a volume mixing ratio of silicate to water-ice. We also estimate the thermal radiation from dust cloud in EKB. The result of thermal emission shows the spectral feature of water-ice at the wavelength of about 60μm. Although it is difficult to estimate the possibility to detect the thermal emission spectrum of EKB dust cloud, due to large uncertainties in its spatial density, we found that the thermal emission of dust cloud in EKB lies below the IRAS data of foreground zodiacal emission. The maximum value of the thermal emission derived from the acceptable dust cloud model in EKB, however, becomes to be comparable to that of foreground zodiacal emission in far-infrared and submillimeter wavelength domains. Since the EKB dust cloud seems to concentrate near the ecliptic plane, a scanning of infrared observation along a line perpendicular to the ecliptic plane may reveal the presence of such dust cloud in the future.

6.1 Introduction

Recently, it has been suggested that significant dust production occurs in Edgeworth-Kuiper Belt (EKB) (e.g., Backman et al., 1995; Liou et al., 1996; Stern, 1996; Yamamoto & Mukai, 1998). One mechanism to produce dust is the mutual collisions of Edgeworth-Kuiper Belt objects (EKOs) (Backman et al., 1995; Stern, 1995,1996), and another is the interstellar dust impacts on EKOs (Yamamoto & Mukai, 1998). However, the existence of these dust grains produced in EKB region has not been directly confirmed by observations of zodiacal light/emission and *in situ* measurements.

Backman et al. (1995) and Stern (1996) calculated the thermal emission brightness from debris created by the mutual collisions of EKOs. Backman et al. (1995) investigated the detectability of the emission by COBE. Stern (1996) reported that the thermal emission brightness exceeds the detection limits of ISO and SITRF, while that is most likely below IRAS detection limits.

The thermal emission brightness depends strongly on the temperature and the emission/absorption efficiency of dust grains. In order to estimate these grain's nature, an optical property of grain becomes important. In the previous works, the simple models of an optical property of grain were used due to the lack of specific knowledge about grain properties. Backman et al. (1995) used a simple model for grain emissivities and albedo. Stern (1996) used the representative temperature of 40K to 60K for EKB dust cloud.

It has been considered that EKB region is a comet reservoir extending outside the orbit of Neptune. Cochran et al. (1995) detected comet-sized objects in EKB using Hubble Space Telescope. Thus, the dust grain from EKO has icy material including small refractory particles such as cometary dust. In order to estimate the thermal radiation from EKB dust cloud, it is important to take into account the optical properties of such a grain.

In this study, we will estimate the temperature of EKB dust grains based on the grain model for water-ice and silicate mixtures such as cometary dust, using the optical constants deduced from the Maxwell-Garnett mixing rule (e.g., Mukai, 1986). From the results, we reexamine the thermal emission from EKB dust cloud, and investigate the detectability of thermal radiation from EKB dust cloud produced by the mutual collisions of EKOs and by the interstellar dust impacts on EKOs, taking into account the contribution of foreground thermal emission.

6.2 Temperature of EKB dust grain

In this section, we examine the temperature of dust grains produced in EKB, based on the model of heterogeneous icy material including small refractory particles (Mukai, 1986).

A grain absorbs the solar energy of E_a and simultaneously emits the energy of E_r. These energy sources are defined by

$$E_a = \pi(R_\odot/r)^2 \int_0^\infty \pi a^2 B_\odot(\lambda) Q_{abs}(a,\lambda,m^*) d\lambda, \tag{83}$$

$$E_r = 4\pi \int_0^\infty \pi a^2 B(\lambda, T_g) Q_{abs}(a,\lambda,m^*) d\lambda, \tag{84}$$

where λ is a wavelength, $R_\odot$ and $B_\odot(\lambda)$ are the radius and solar surface brightness, respectively, and r is the solar distance of dust grain with a radius of a. The Planck function $B(\lambda, T_g)$ at the temperature T_g of the dust grain is defined by $B(\lambda, T_g) = 2hc^2\lambda^{-5}[\exp(hc/\lambda k_b T_g) - 1]^{-1}$, where h, k_b, and c are the Planck constant, the Boltzmann constant, and the speed of light, respectively. For simplicity we assume that the dust grain from EKO has a spherical shape. In this case, the efficiency factor for absorption/emission Q_{abs} is deduced by Mie Theory as functions of a, λ and m^*, where m^* is the complex refractive index of grain material. For the case of heterogeneous icy material consisting of icy matrix embedded with small refractory inclusions, the Maxwell-Garnett mixing rule to calculate m^* is applicable (Mukai, 1986).

We used the dielectric function of olivine for inclusions and water-ice for the matrix. For the optical constants of water-ice, we employ the data of Warren (1984) in a domain of wavelength $\lambda = 0.14 - 1000\mu m$. For olivine, we used the data given by Huffman & Stapp (1973) and Huffman (1976) in $\lambda = 0.14 - 7\mu m$, and those by Mukai & Koike (1990) in $\lambda = 7 - 200\mu m$. Since no data of the optical constant for olivine beyond $\lambda = 200\mu$m are available, the constant value of m^* of Mukai & Koike (1990) at $\lambda = 200\mu$m is used in $\lambda =$ 200-1000μm for olivine. This assumption does not have a significant influence on the result. The solar spectrum of $B_\odot$ is complied in Mukai (1990) in $\lambda = 0.14 - 300\mu$m wavelength domain. For the $B_\odot$ beyond $\lambda = 300\mu$m to 1000μm, we adopted the brightness temperature of 5780 K.

The integration of Eqs.(83) and (84) is carried out in the wavelength domain of 0.14μm to 1000 μm. Under a local thermal equilibrium of the grain, the input energy on the grain is balanced with the output energy, *i.e.*, $E_a = E_r$. The energy loss by sublimation of water-ice is negligibly small in the region of interest. Consequently, we obtained the equilibrium temperature of EKB dust grain as functions of a and r.

The resulting temperatures for the volume fraction of olivine of 0%, 1%, and 10% are plotted in Fig. 18. As increasing the volume fraction of olivine, the temperature of grain increases compared with that of pure water-ice. According to Greenberg (1982), the expected volume faction of refractory materials in cometary dust is less than 10%. In this case, the temperature of dust grain in EKB seems to be lower than that of blackbody (Fig. 18). Furthermore, we calculated the temperature for the case of higher refractory material (100%), that is a pure olivine grain. While the temperature of grains with radii less than a few μm becomes to be higher than the blackbody temperature, the grains with radii larger than a few μm still have lower temperature compared to the blackbody temperature (Fig. 18).

Backman et al. (1995) calculated that the small grain with radius of 1μm would have a temperature of 100K and the larger grain would have a temperature of about 40K at 30AU, based on a simple model for grain emissivities and albedo. Stern (1996) used the isothermal model of temperature at 40K to 60K, which values were estimated from those of the blackbody in EKB region. On the contrary, we found that the dust grain in EKB has temperature ranging from 20K to 50K, when EKB dust grain is heterogeneous icy material consisting of refractory inclusions embedded in the icy matrix, such as cometary dust.

6.3 Thermal emission from EKB dust cloud

Based on the results of EKB dust temperature $T_g(a,r)$ obtained above, we will estimate the thermal emission from EKB dust cloud. The thermal emission of EKB dust cloud B_{EKO} within the range of wavelength λ to $\lambda + d\lambda$ is calculated as

$$B_{EKO} = \int_{\theta(r=30AU)}^{\theta(r=50AU)} \frac{\sin e}{\sin^2\theta} d\theta \int_{a_1}^{a_2} n(a,r)\pi a^2 Q_{abs}(a,\lambda,m^*) B(\lambda, T_g(a,r)) da, \tag{85}$$

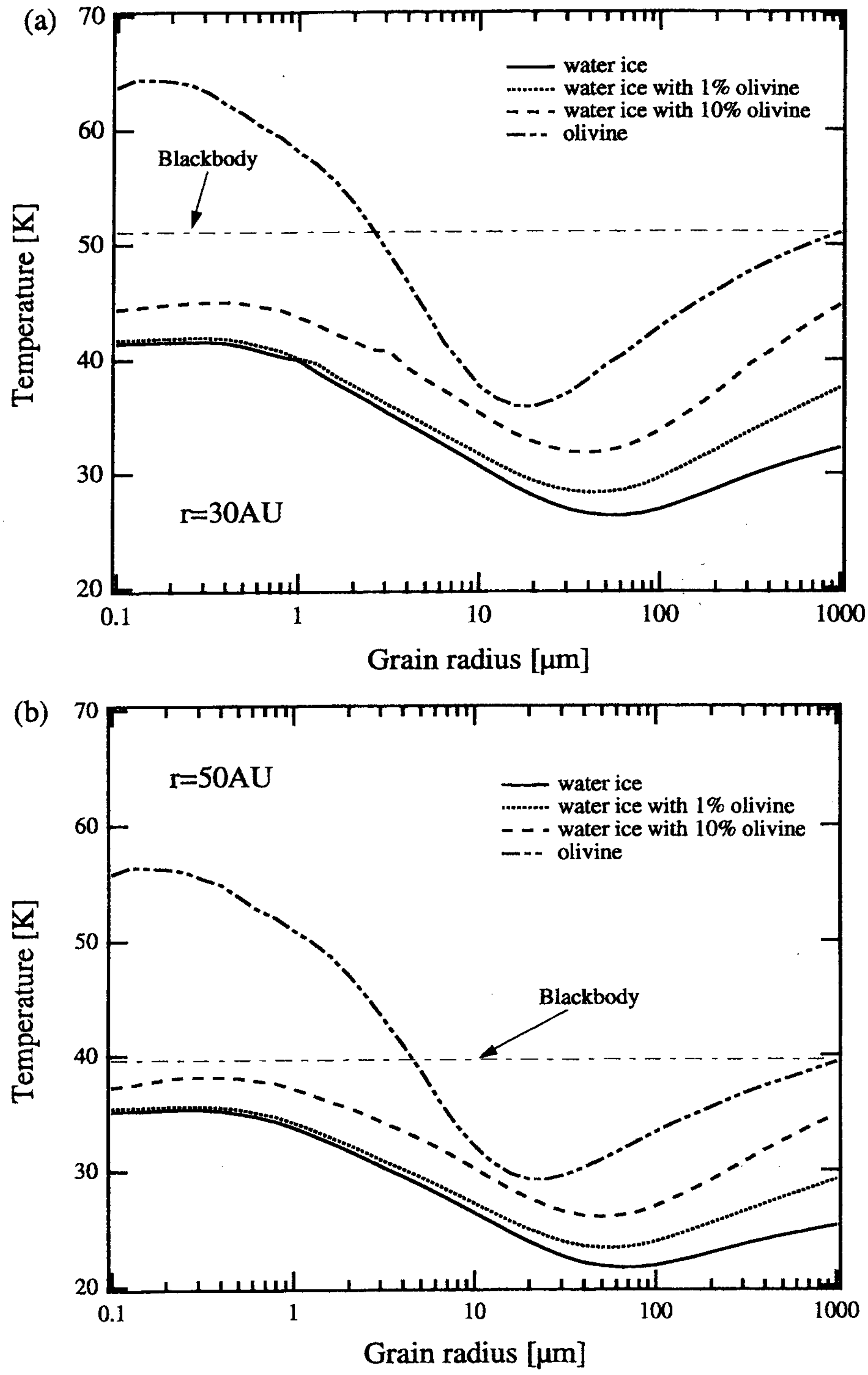

Figure 18: Temperature of the grain, consisting of icy matrix with olivine inclusions, at a solar distance of (a) $r = 30$ AU and (b) $r = 50$ AU. A volume fraction of olivine is 0%, 1%, and 10%. Dash-dotted line indicates the blackbody temperature.

where a_1 and a_2 are, respectively, the minimum radius and the maximum radius of EKB dust grain, r is a solar distance, e is an elongation angle (angle between the radial direction from the Earth to the Sun and the line of sight), and θ is an angle between the line of sight and the radial direction from the Sun to the EKB dust (see, Peterson, 1963). The width of EKB region is assumed to be from $r = 30$ AU to $r = 50$ AU (Jewitt & Luu, 1995).

For simplicity, the number density $n(a,r)da$ of EKB dust with radii between a and $a + da$ at the solar distance r is assumed as,

$$n(a,r)da = C_0 a^{\beta}(D/r)^q da, \tag{86}$$

where C_0 is a constant, a power-law exponent β is -3.5 (Backman et al., 1995; Stern, 1996), D = 30AU, and q is a power-law exponent. The value of q depends on the spatial distribution of dust grain in EKB. The dust grain in EKB evolves its orbit under the complex influences of gravitational forces of the Sun and the giant planets, mutual collisions of grains, as well as solar radiation pressure and Poynting-Robertson effects (Liou et al., 1996). For simplicity, we assume a constant radial distribution of EKB dust, that is $q = 0$. In order to calculate B_{EKO} in Eq.(85), it is necessary to determine the value of C_0 in Eq.(86). According to Grün et al. (1985), the total cross-sectional area for the interplanetary meteoroids is estimated to be 4.6×10^{-21} cm^2/cm^3 at 1AU. If the total cross-sectional area of EKB dust cloud is f times as large as that of interplanetary flux model at 1AU, the value of C_0 is derived from Eq.(86),

$$C_0 \int_{r=30AU}^{r=50AU} (D/r)^q dr \int_{a_1}^{a_2} a^{-3.5}\pi a^2 da = f \times 4.6 \times 10^{-21} \times (50\ [\text{AU}]\ \text{-}\ 30\ [\text{AU}]). \tag{87}$$

Stern (1996) predicted that the optical depth of debris produced by mutual collisions of EKOs is between 3×10^{-7} to 5×10^{-6} for infrared wavelength domain. On the other hand, from IRAS observations, the optical depth of zodiacal emission at a wavelength of 12μm in the ecliptic plane at elongation 91.1° was estimated to be 3×10^{-7} to 2.8×10^{-6} (Hauser et al., 1984). Consequently, the ratio of optical depth of EKB dust cloud to that of interplanetary flux model is ranging from about 0.1 to 20. If we assume that the total cross-sectional area is proportional to the optical depth, the value of f is estimated to be about 0.1 to 20. Consequently, assuming $a_1 = 10^{-5}$ cm and $a_2 = 10^{-1}$ cm, the value of C_0 becomes 2×10^{-25} to 4×10^{-23} from Eq.(87).

On the other hand, Yamamoto & Mukai (1998) estimated that the optical depth of grains produced by interstellar dust impacts on EKOs is ranging from 2.4×10^{-7} to 2.0×10^{-5}. Again, we assume that the total cross-sectional area is proportional to the optical depth, and then the value of f is estimated to be from 0.1 to about 70. Since the interstellar dust impacts on EKOs provide only small dust grain with radii less than about 10μm (Yamamoto & Mukai, 1998), we set $a_1 = 10^{-5}$ cm and $a_2 = 10^{-3}$ cm. Consequently, the value of C_0 is calculated to be 3×10^{-25} to 2×10^{-22} from Eq.(87).

From $n(a,r)$ and C_0 estimated above, we estimate the total mass of dust in EKB. We assume that the EKB is a band with thickness of 16deg around ecliptic, with solar distance between 30 AU and 50 AU (Jewitt & Luu, 1995), and the density of grain material is 1 g cm^{-3}. In this case, the total mass of dust existing in EKB produced by mutual collisions of EKOs is 2×10^{-8} $M_{\oplus} \sim 3 \times 10^{-6}$ $M_{\oplus}$, and those produced by the interstellar dust impacts is 2×10^{-9} $M_{\oplus} \sim 2 \times 10^{-6}$ $M_{\oplus}$ where $M_{\oplus}$ is the Earth mass. On the other hand, the total mass of EKOs with diameters larger than 6 km inside 50 AU is estimated to be from 0.1 $M_{\oplus}$ to 0.4 $M_{\oplus}$ (Stern, 1998).

Applying these values into Eq.(85), we calculated the thermal emission from EKB dust cloud at $e = 90°$ as a function of wavelength for the case of mutual collisions of EKOs (Fig. 19) and for the case of interstellar dust impacts (Fig. 20). There is a spectral feature of water-ice at around 60μm in Figs. 19 and 20. For comparison, the result for higher refractory material, that is the pure olivine, is also shown.

After leaving EKB, some EKB dust grains suffer from the mutual collisions of grains and interstellar dust impacts (Liou et al., 1996). A disruption of grain provides an increase of total cross-sectional area with decreasing a solar distance of EKB dust grain under the Poynting-Robertson effect. In this scenario, the EKB dust cloud has total cross-sectional area smaller than that observed at 1 AU. This is the case of $f < 1$

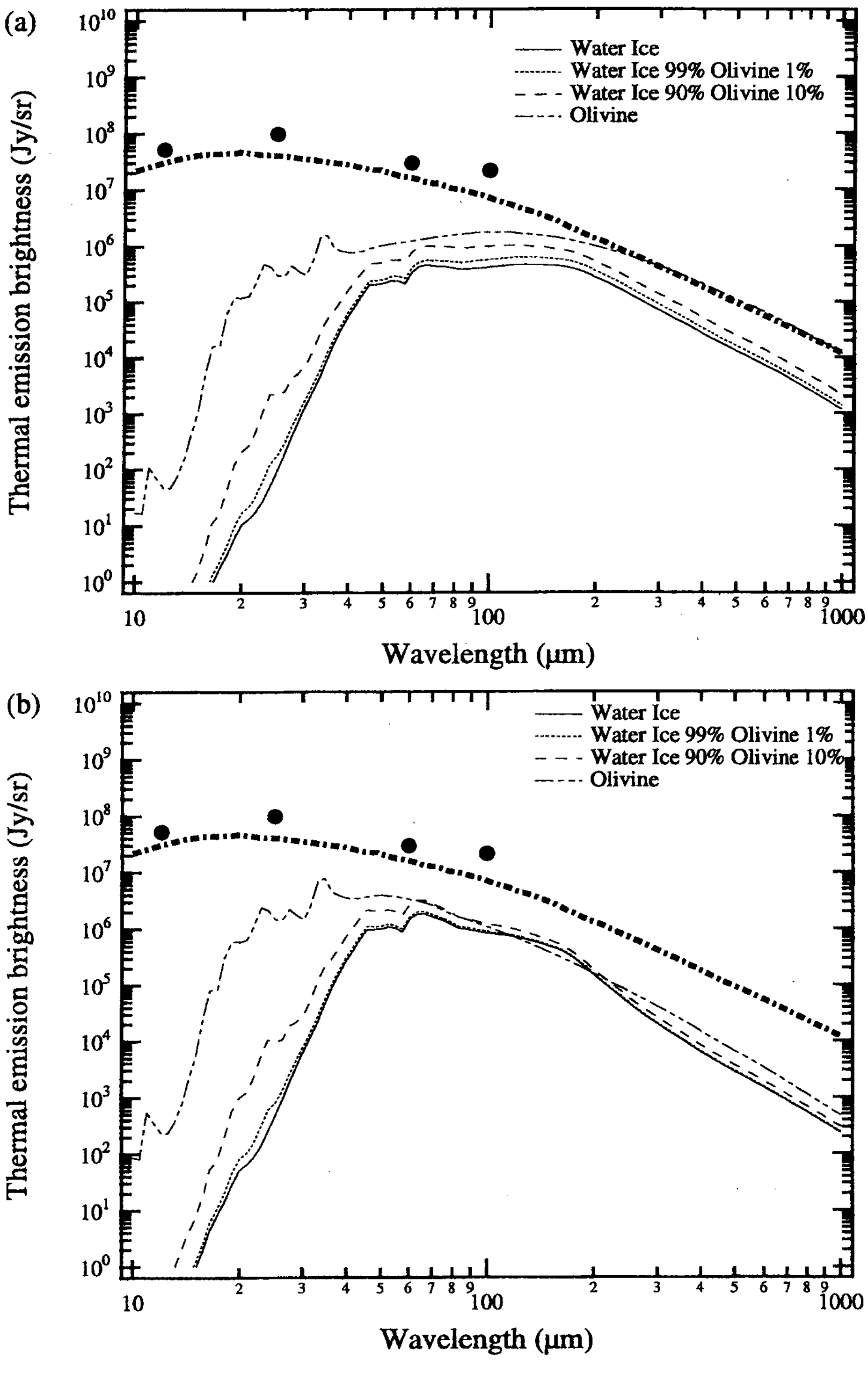

Figure 19: Thermal emission from EKB dust cloud produced by mutual collisions of EKOs as a function of wavelength for (a) the maximum case of expected brightness and (b) the minimum case, where the both cases are detailed in the text. A volume fraction of olivine is 0%, 1%, and 10%. For comparison, IRAS data (Hauser et al., 1984) (filled circles) and the model of zodiacal dust emission (Temi et al., 1988) (dash-dotted line) are also plotted for the foreground zodiacal emission (see text).

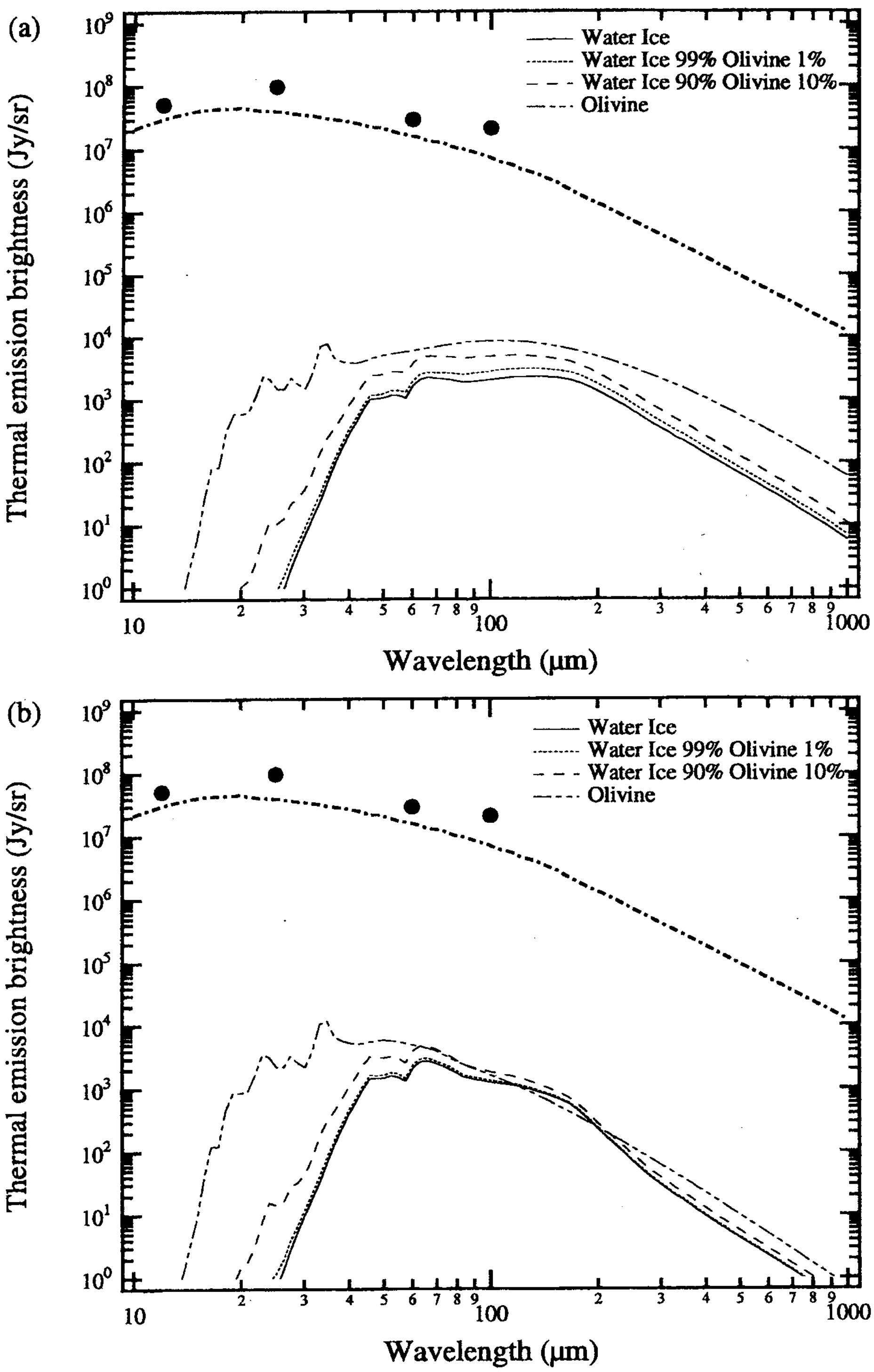

Figure 20: The same as Fig. 19, but for the EKB dust cloud produced by interstellar dust impacts on EKOs.

(Fig. 19(b) and Fig. 20(b)). On the other hand, the loss of grains due to dynamical processes such as gravitational scattering, the solar radiation pressure, and due to sublimation could remove the dust grains from the Solar System, before the grains reach inner Solar System (Liou et al., 1996). This is the case of $f > 1$ (Fig. 19(a) and Fig. 20(a)).

For comparison, IRAS data in ecliptic plane (Hauser et al., 1984) for foreground zodiacal emission at $e = 91.1°$ are plotted in Figs. 19 and 20 as filled circles. In addition, the model of zodiacal dust emission at $e = 90°$ (Temi et al., 1988) in $\lambda = 10 - 200\mu$m is plotted (dash-dotted line). For the model of zodiacal dust emission beyond $\lambda = 200\mu$m, we extrapolated the results of Temi et al. (1988), assuming the representative zodiacal emission temperature of 244 K (Hauser et al., 1984) and blackbody of the grains. The thermal emission of EKOs is fainter than that of IRAS in all cases considered here. This means that it is difficult to find the thermal emission spectrum of EKB dust cloud in the previous infrared observations from the Earth. On the other hand, for the maximum case shown in Figs. 19(a) and 20(a), the thermal emission from EKB dust cloud should be comparable than the foreground zodiacal emission in far-infrared and submillimeter regions. In this case, a spatial variation of the color between mid-infrared and submillimeter regions might be observed.

It is likely that the EKB dust cloud has a band structure with a thickness of about 10 to 20 degrees around the ecliptic as that of parent EKOs (Jewitt & Luu, 1995). The maximum values of the thermal emission from EKB dust cloud attains about tens of percentages of that of foreground zodiacal emission. In this case, the detail scanning of thermal radiation along a line perpendicular to the ecliptic plane may reveal the contribution of EKB dust cloud to the foreground zodiacal dust cloud. Since the gradient of brightness depends on the latitudinal distribution of EKB dust cloud, it is important to know the spatial distribution of parent EKOs. Up to now, no available data for the spatial distribution of whole EKOs exist. Thus, more detailed analysis of dynamical properties of EKB dust grain is required to construct a reliable cloud model, and predict the detectability of EKB dust cloud from the Earth.

It is worthwhile to investigate various scenarios for heliocentric distribution of EKB dust cloud. We calculated the thermal emission from EKB dust cloud when $n(a,r) \propto r^{-1}$ and $n(a,r) \propto r^{-2}$, and found that there are no significant deference between these results and the results for the case of constant distribution of EKB dust model. Thus, we conclude that the heliocentric distribution of EKB dust cloud does not have a significant influence on the total thermal emission.

While the interstellar dust impacts on EKOs provide only small dust grains with radii less than 10μm, the mutual collisions of EKOs provide both small and large dust grains. However, there are no significant difference of the thermal emission spectrum between the former and the latter in the wavelength shorter than about 60μm. Since we used the model of number density of $n(a) \propto a^{-3.5}$, the small grains of EKB dust cloud have the large total cross-sectional area compared to large dust grains. Namely, the thermal emission mainly comes from the small dust grains, except for longer wavelength domain.

Furthermore, we investigated the sensitivity of our results to the value of the minimum radius of EKB dust grain a_1 in Eq.(85). By using $a_1 = 0.01\mu$m, corresponding to the radius of small refractory particle found in cometary grain (e.g., McDonnell et al., 1986), we reexamined the thermal radiation from EKB dust cloud. We found that the change of a_1 from 0.1μm to 0.01μm leads to a decrease of the total thermal radiation one third of that for $a_1 = 0.1\mu$m.

6.4 Summary

We estimated the temperatures of EKB dust grains, based on the model of heterogeneous icy material consisting of small refractory inclusions embedded in icy matrix such as cometary dust. It is found that the dust grain in EKB has temperature, which depends on its radius, ranging from 20K to 50K. Applying the results of temperature for EKB dust grains, we examine the thermal emission from EKB dust cloud produced by the mutual collisions of EKOs and by the interstellar dust impacts on EKOs. The thermal emission of icy grain with small refractory inclusions shows the spectral feature of water-ice at the wavelength of about 60μm. Since the predicted thermal emission from EKB dust cloud is fainter than that of IRAS data, however, it seems to be difficult to find a sign of thermal emission from EKB dust cloud in the past observations from the Earth.

The maximum case of thermal emission from EKB dust cloud presented here becomes to be comparable to that of foreground zodiacal emission at the wavelength of about tens of μm to hundreds of μm. When the EKB dust cloud has a narrow spatial band structure with a thickness of about 10 to 20 degree around the ecliptic as predicted for EKOs (Jewitt & Luu, 1995), the scanning of thermal radiation along a line perpendicular to the ecliptic plane may give a hint of the presence of EKB dust cloud in the future observations.

Acknowledgement We are grateful to S.A.Stern and T.Matsumoto for giving valuable comments and suggestions as reviewers.

References

Backman, D.E., Dasgupta, A., Stencel, R.E, 1995, ApJ, 450, L35.

Cochran, A.L., Levison, H.F., Stern, S.A., Duncan, M.J., 1995, ApJ, 455, 342.

Greenberg, J.M., 1982, Comets (edited by Wilkening, L.L.), pp. 131.

Grün, E., Zook, H.A., Fechtig, H., Giese, R.H., 1985, Icarus, 62, 244.

Hauser, M.G., Gillett, F.C., Low, F.J., et al., 1984, ApJ, 278, L15.

Huffman, D.R. Stapp, J.L., 1973, Interstellar dust and related topics (edited by Greenberg, J.M.,van de Hulst, H.C.), pp. 297, IAU Symp. 52.

Huffman, D.R., 1976, Solid State Astrophysics (edited by Wickramasighe, N.C., Morgan, D.J.), pp. 191.

Jewitt, D.C., Luu, J.X., 1995, AJ, 109, 1867.

Liou, J.-C., Zook, H.A., Dermott, S.F., 1996, Icarus, 124, 429.

McDonnell, J.A.M., Alexander, W.M., Burton, W.M., et al., 1986, Nature, 321, 338.

Mukai, T., 1986, A&A, 164, 397.

Mukai, T., 1990, Evolution of Interstellar dust and related topics (edited by Bonetti, A., Greenberg, J.M., Aiello, S.), pp. 397, Elsevier Science.

Mukai, T., Koike, C., 1990, Icarus, 87, 180.

Peterson, A.W., 1963, ApJ, 138, 1218.

Stern, S.A., 1995, AJ, 110, 856.

Stern, S.A., 1996, A&A, 310, 999.

Stern, S.A., 1998, Cosmic Origins: Galaxies, Stars, Planets, and Life (edited by Shull, J.M., Woodward, C.A., Thronson, H.A.), Astron. Soc. of Pacific publishers, in press.

Temi, P., de Bernardis, P., Masi, S., et al., 1988, Experiments on cosmic dust analogue (edited by E.Bussoletti, Fusco, C., et al.), pp. 337.

Warren, S.G., 1984, Appl. Opt., 23, 8, 1206.

Yamamoto, S., Mukai, T., 1998, A&A, 329, 785.

7 Dust Disk in Outer Solar System

S.Yamamoto, H.Ishimoto, & T.Mukai
Proc. of the 31th ISAS Lunar & Planetary Symposium., 156-169 (1998)

Abstract

We investigate the mass distribution of EKB dust disk beyond 50 AU using numerical model which takes into account grain-grain collisions and the Poynting-Robertson effect. As decreasing the solar distance, the total cross-sectional area of dust grains increases. Based on the resulting mass distribution of dust disk, its brightness of thermal emission is calculated. Since the predicted thermal emission from EKB dust disk is fainter than the IRAS data of foreground zodiacal emission, it seems to be difficult to find out a sign of thermal emission from such EKB dust disk, if it would exist, in available observation in infrared wavelength domain. The thermal emission from EKB dust disk, however, may be comparable to that of foreground zodiacal emission in far-infrared and submillimeter wavelength domains. Since the EKB dust disk seems to concentrate near the ecliptic plane, a scanning of infrared observation along a line perpendicular to the ecliptic plane may reveal the presence of EKB dust disk.

7.1 Introduction

Recently, it has been proposed that the significant dust production occurs in the Edgeworth-Kuiper Belt (EKB) (Backman et al.1995; Stern 1996; Yamamoto & Mukai 1998a). The dust production rates from EKB between the solar distances of 30 AU and 50 AU have been investigated for the cases of mutual collisions of Edgeworth-Kuiper Belt objects (EKO)(Backman et al. 1995; Stern 1996) and interstellar dust impacts (Yamamoto & Mukai 1998a). Based on these dust production rates, the thermal emission brightnesses from EKB dust disk between the solar distances of 30 AU and 50 AU have been calculated (Backman et al. 1995; Stern 1996; Yamamoto & Mukai 1998b). In addition to EKOs between the solar distances of 30 AU and 50 AU, it is suggested that the aggregates of planetesimals, which are too faint to detect from the Earth, must exist beyond 50 AU (Yamamoto & Kozasa 1988). Thus, the contribution of thermal emission from the objects in EKB beyond 50 AU should be considered.

For the estimation of thermal emission brightness, the knowledge of size distribution of grains in EKB dust disk becomes important. In the previous works (Backman et al. 1995; Stern 1996; Yamamoto & Mukai 1998b), the simple models of power-law size distribution of dust grains in EKB were used. Since the Poynting-Robertson decay time of dust grains beyond 50 AU is too long, however, the mutual collisions of debris particles and the collisions by interstellar dust grains become important in the determination of size distribution. In order to estimate the equilibrium size distribution of dust grains in EKB regions, we will take into account the collisional evolution of dust grains in EKB region in this paper.

Furthermore, we shall investigate the dust production rate from EKO existing beyond 50 AU (Sect. 7.2). In Sect. 7.3, the mass distributions of EKB dust disk beyond 50 AU will be investigated based on numerical model which takes into account grain-grain collisions and the Poynting-Robertson effect (Ishimoto & Mann 1998; Ishimoto 1998). From these results, we will examine the thermal emission from EKB dust disk beyond 50 AU in Sect. 7.4.

7.2 Dust production rate from EKOs

According to planetesimal model, the mass m of the aggregate of planetesimals (that is EKO) with density of $\rho = 1$ g cm^{-3} at a solar distance r is estimated (Yamamoto & Kozasa 1988) by

$$m = \gamma \sigma_{d1}^3 (r_0)^6 (r/r_0)^{6-3n} \left(\frac{2\pi^2}{f_p M_\odot}\right)^2 \left(1 + \frac{4.4 \times 10^5}{\gamma^{1/3}(r/r_0)^{3.5}}\right)^3, \tag{88}$$

where $r_0 = 1$ AU, σ_{d1} denotes the surface density of dust in the solar nebula, $M_\odot$ means a solar mass, a constant $f_p \sim 1.057$ (Nakano 1987), and a parameter γ is related to the total number of planetesimals in

EKB. The minimum-mass model of the solar nebula by Hayashi (1981) gives $\sigma_{d1} = 30$ g cm^{-2} and $n = 1.5$. The value of γ is estimated to be from 10^{-3} to 10^{-7} (Yamamoto & Kozasa 1988). For simplicity, we use $\gamma = 10^{-3}$. By using Eq.(88), the spatial distribution of the aggregates $n_p(r)dr$ between solar distance r and $r + dr$ is expressed by

$$n_p(r)dr = 2\pi r \frac{\sigma_{d1}(r/r_0)^{-n}}{m} dr. \tag{89}$$

When $\gamma = 10^{-3}$, the total number of EKOs existing between $r = 50$ AU and 200 AU is about 6×10^9. By using Eq.(89), the mass flux $M(r)dr$ of collisional fragments produced between r and $r + dr$ is calculated as,

$$M(r)dr = F_t(m,r)n_p(r)dr, \tag{90}$$

where $F_t(m,r)$ is a production rate of impact ejecta from target body with mass of m at the solar distance r.

For the case of mutual EKO collisions, $F_t(m,r)$ is derived by

$$F_t(m,r) = M(> v_{esc}) \frac{n_p(r)dr}{2\pi r dr \times 2ri} Av, \tag{91}$$

where $M(> v_{esc})$ is the total mass of collisional fragments having the velocities beyond the escape velocity from colliding pair, i is a mean inclination of the planetesimal orbits from the central plane, A is a collision cross section, and v is the relative collisional velocity at r. In this study, the value of v is set to be the random velocity of the aggregates (Nakano 1987), i.e.

$$v = \left(\frac{G}{\theta}\right)^{0.5} \left(\frac{4\pi\rho}{3}\right)^{1/6} m^{1/3} \tag{92}$$

where θ is the Safronov parameter and G is the gravitational constant. According to Nakano (1987), we set $i = v/v_k$ where v_k is the circular Keplerian velocity at r.

The specific impact energy Q is calculated according to the standard definition, $Q = 0.5v^2$ (Housen & Holsapple 1990). We use a strain-rate scaling model for threshold value of catastrophic fragmentation, Q^* (Housen & Holsapple 1990). If $Q > Q^*$, the colliding pair of EKOs are disrupted (catastrophic disruption). When $Q < Q^*$, the impact of projectile produces a crater on the target surface (cratering event). For the case of $\gamma = 10^{-3}$, $Q > Q^*$ occurs beyond $r = 50$ AU. Namely, the mutual EKO collision causes a catastrophic disruption. While the collisional fragments having enough ejection velocity escape from the colliding pair, the remnants are reaccumulated due to their own gravity. In order to estimate the value of $M(> v_{esc})$, we use the catastrophic disruption model by Colwell & Esposito (1993).

In the case of interstellar dust impacts, we use the model for a hard surface of EKO by Yamamoto & Mukai (1998a) to estimate $F_t(m,r)$ in Eq.(90).

Substituting Eqs. (88) and (89) into Eq.(90), the mass production rates as a function of r are calculated for the cases of the interstellar dust impacts and the mutual collisions of EKOs (Fig. 21), where the outer limit of EKB region is assumed to be 200 AU.

The size of collisional debris produced by the mutual collisions of EKOs ranges from multi-kilometer blocks to fine dust, while the interstellar dust impacts provide only dust with radii smaller than about 10 μm (Yamamoto & Mukai 1998a). In this study, the number density $n_0(m,r)$ of ejecta produced both by the mutual EKO collisions and by the interstellar dust impacts is assumed as,

$$n_0(m,r) \propto m^{-q}. \tag{93}$$

Kato et al.(1995) estimated that the value of q ranges from about 1.63 to 1.90, based on impact experiments onto icy targets. By using Eq.(93) for $q = 1.67$, we estimate the fraction of dust grains with radii smaller than 10μm in the debris produced by mutual EKO collisions (Fig. 21). It is found that beyond r =70 AU the dust production rate due to the interstellar dust impacts is greater than that due to mutual EKO collisions for the grains with radii $< 10\mu$m.

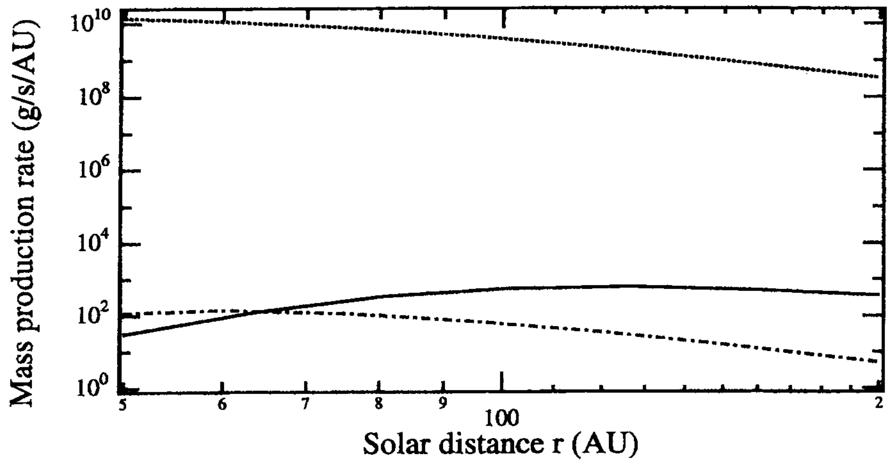

Figure 21: Mass production rates as a function of r for the cases of the interstellar dust impacts (solid curve) and the mutual collisions of EKOs (dotted curve). For comparison, the fraction of dust grains with radii smaller than 10μm in the debris produced by mutual EKO collisions is also shown (dash-dotted curve).

7.3 Mass distribution of EKB dust disk

We examine the equilibrium mass distribution of dust grains in EKB dust disk using numerical model which takes into account grain-grain collisions and the Poynting-Robertson effect (Ishimoto & Mann 1998; Ishimoto 1998). According to Ishimoto (1998), the radial and mass dependence of the number density distribution $n(m,r)$ for EKB dust grains is derived by

$$\frac{\partial n(m,r)}{\partial r} = -\frac{n(m,r)}{r} - \frac{rc}{2\beta G M_{\odot}} Y(m,r) \tag{94}$$

where $M_{\odot}$, G, and c are, respectively, the solar mass, the gravitational constant and the speed of light, and β is a ratio of solar radiation pressure to the solar gravity. The term $Y(m,r)$ includes collisional gain and loss due to mutual grain collisions and due to impacts between interstellar dust onto grains as well as direct dust supply from EKOs estimated in Fig. 21. Since the ejected grains with large β attain hyperbolic orbits due to the solar radiation pressure (Burns et al. 1979), we assume that the small grains with masses less than about 10^{-12}g escape from the Solar System.

By using Eq.(94), the mass distribution of grains in EKB dust disk for the steady state is calculated as a function of r and m (Fig. 22). The impacts of interstellar dust disrupt the grains with masses of about 10^{-9} to 10^{-5}g, and then smaller grains are produced. On the other hand, the large EKB grains are not disrupted by the interstellar dust impacts. As decreasing the solar distance under the Poynting-Robertson drag, the number density of small dust grains increases compared with that of larger dust grains due to these collisions. Therefore, the total cross-sectional area of dust grains increases with decreasing the solar distance.

7.4 Thermal emission brightness from EKB dust disk

From the mass distribution of grains in EKB dust disk obtained above, we examine the thermal emission from EKB dust disk beyond r =50 AU. Grains' temperatures are calculated using expressions in Yamamoto & Mukai (1998b) for the thermal equilibria. For optical constants of EKB dust grains, we use water-ice and astronomical silicate. By using the resulting temperature of EKB grains, we estimate the thermal emission from EKB dust disk along a line of sight from r = 50 to 200 AU (Fig. 23). For comparison, IRAS data in

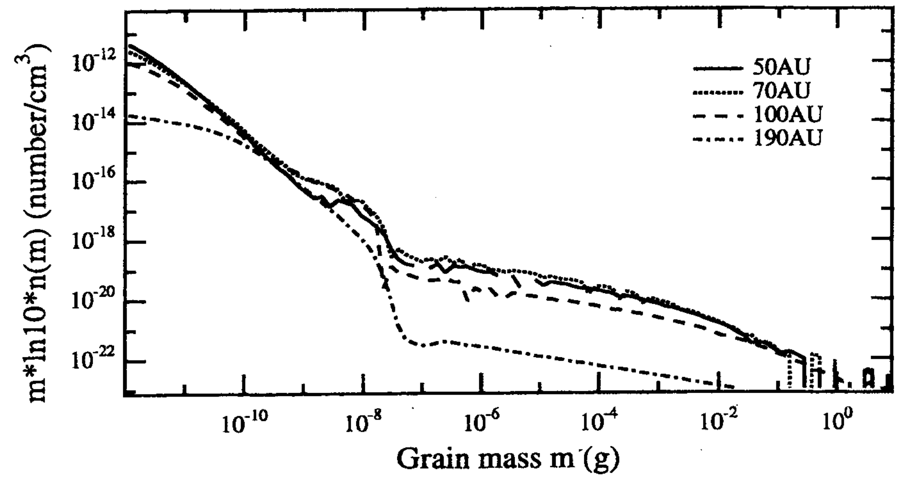

Figure 22: Mass distribution of dust grains in EKB dust disk at the solar distances of 50, 70, 100, and 190 AU.

ecliptic plane (Hauser et al., 1984) for foreground zodiacal emission at a solar elongation angle of 91.1° are plotted in Fig. 23 as filled circles. The expected thermal emission of EKOs is fainter than that of IRAS in all cases considered here. This means that it is difficult to find the thermal emission spectrum of EKB dust disk from the Earth directly in infrared wavelength domain. On the other hand, for the case of astronomical silicate, the thermal emission from EKB dust disk may be comparable than the foreground zodiacal emission in far-infrared and submillimeter regions.

7.5 Summary

We investigate the mass distribution of EKB dust disk beyond r =50 AU using numerical model which takes into account grain-grain collisions and the Poynting-Robertson effect. As decreasing the solar distance, the number density of small dust grains increases compared with that of larger dust grains. This indicates that the total cross-sectional area of dust grains increases with decreasing the solar distance.

The predicted thermal emission brightness from EKB dust disk beyond r = 50 AU is fainter than that of IRAS data in infrared wavelength domain. It has been reported that the thermal emission from inner EKB (30-50 AU) is also fainter than that of IRAS data in infrared wavelength domain (Yamamoto & Mukai 1998b). Therefore, it seems to be difficult to find a sign of thermal emission from EKB dust disk in the past observations from the Earth. However, in far-infrared and submillimeter wavelength domains, the thermal emission from EKB dust disk presented here may become comparable to that of foreground zodiacal emission. When the EKB dust disk has a narrow spatial band structure with a thickness of about 10 to 20 degree around the ecliptic as predicted for EKOs (Jewitt & Luu, 1995), the scanning of thermal radiation along a line perpendicular to the ecliptic plane may reveal a hint of the presence of EKB dust disk in the future observations.

References

Backman, D.E., Dasgupta, A., Stencel, R.E., 1995, ApJ, 450, L35.

Burns, J,A., Lamy, P.L., Soter, S., 1979, Icarus, 40, 1.

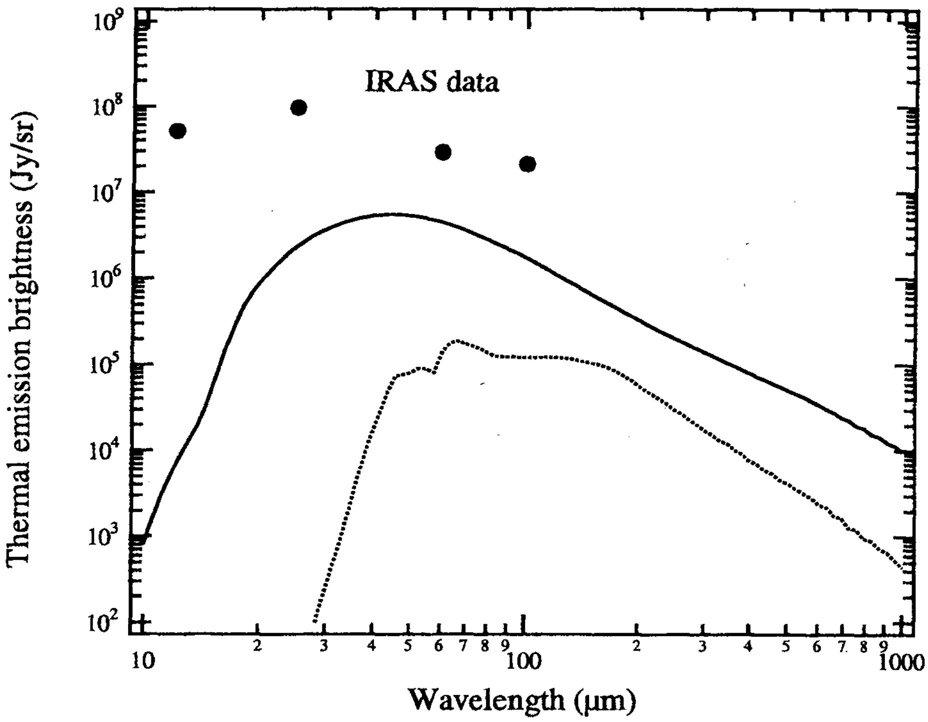

Figure 23: Thermal emission from EKB dust disk from $r = 50$ to 200 AU for the case of astronomical silicate (solid curve) and for the case of water-ice (dotted curve). For comparison, IRAS data (Hauser et al., 1984) (filled circles) are also plotted for the foreground zodiacal emission.

Colwell, J.E., Esposito, L.W., 1993, J. Geophys. Res., 98, 7387.

Hauser, M.G., Gillett, F.C., Low, F.J., et al., 1984, ApJ, 278, L15.

Housen, K.R., Holsapple, K.A., 1990, Icarus, 84, 226.

Hayashi, C., 1981, Suppl. Prog. Theor. Phys., 70, 35.

Ishimoto, H., Mann, I., 1998, Planet. Space Sci., in press.

Ishimoto, H., 1998, Adv.Space.Res., submitted.

Jewitt, D.C. Luu, J.X., 1995, AJ, 109, 1867.

Kato, M., Iijima, Y., Arakawa, M., et al., 1995, Icarus, 113, 423.

Nakano, T., 1987, Mon. Not. R. Astron. Soc., 224, 107.

Stern, S.A., 1996, A&A, 310, 999.

Yamamoto,T., Kozasa, T., 1988, Icarus, 75, 540.

Yamamoto,S., T.Mukai, 1998a, A&A, 329, 785.

Yamamoto,S., T.Mukai, 1998b, Earth Planets Space, 50, 531.